

PENNING TRAP MASS SPECTROMETRY Q -VALUE DETERMINATIONS FOR
HIGHLY FORBIDDEN AND ULTRA-LOW Q -VALUE β -DECAYS

By

Rachel Nicole Sandler

A DISSERTATION

Submitted to
Central Michigan University
in partial fulfillment of the requirements
for the degree of

Physics - Doctor of Philosophy

2019

Dedicated to coffee, the most benevolent of beans.

“How can you drink that? No milk? No sugar?”
“Exactly. It’s just you and the bean.”
-Chandana Sumithrarachchi and Ryan Ringle

ACKNOWLEDGMENTS

Graduate school has been the most intense chapter of my life thus far and I am so appreciative of everybody who helped me through it. First I'd like to thank my doctoral advisor, Matt Redshaw, and my advisor for my master's degree, Georg Bollen. Georg's enthusiasm and warm welcome convinced me to join the LEBIT group and gave me a place to call my own during the most stressful transition of my life up to that point. When I fell short of MSU's testing requirements, Matt came to my rescue, giving me a solution that allowed me to continue working towards my goals with the least possible amount of life upheaval. Thank you, Matt, for bending over backwards to accommodate my anxiety problems, and thank you both for the guidance—and funding!—you provided to help me become the best scientist I possibly could. Thank you also to the rest of my committee, Ryan Ringle, Alan Jackson, and Mihai Horoi for taking the time to read through this thesis and guide me through my PhD.

Ryan Ringle deserves a second thank you. As the person most optimized between knowledge and availability, I appreciate your patience as I came to you with all kinds of problems over the years, from codes which wouldn't run to buttons I couldn't reach in the lab.

There were numerous collaborators who helped with the creation of this thesis and the work within. At the NSCL, the post-docs for my first several years, Martin Eibach and Kerim Gulyuz, as well as the other graduate students over the years, Adrian Valverde, Chris Izzo, Alec Hamaker, Isaac Yandow, Danny Puentes, and Jason Surbrook (kinda) were always there to help analyze data, hold things in place, or just vent about ugly, dirty beam. You all taught me a million things and made this work possible. At ANL, the scientists and graduate students there, Guy Savard, Jason Clark, Rodney Orford, and Dwaipayan Ray

were welcoming and instructive, teaching me how to use the equipment, taking shifts, and helping to analyze the data.

Thank you to my family for being there when I needed you and helping to support me this far. To my nephews, Noah, Max, and Oliver, I can't wait to see where you go in life. You're all going to do such amazing things and I'm so excited for you.

Graduate school also wouldn't have been possible without my friends, who kept me sane over the years and prevented me from becoming a hermit. Whether writing together, playing board games, playing video games, making cocktails, renting AirBnBs for New Year's, or any of the other incredible things we did, I'll miss you all. I hope we all keep in touch as we finish school and branch out into the real world.

Finally, but most importantly, thank you to Justin. You have been everything to me over the past five years. You've been the most welcoming and accepting friend I've ever had. You've been the light in my life, helping me to see the positive, even when all I could see on my own was the negative. You've helped me to become a better person. You've pushed me to try new and exciting things I never would have been brave enough to try on my own, from cosplaying at Youmacon to cooking our own Crunchwraps. You've shared your passions with me and delighted in my own passions. You've given the greatest hugs known to mankind. I love and respect you more than I can say in words and I can't wait to discover our next adventure together in Tennessee.

ABSTRACT

PENNING TRAP MASS SPECTROMETRY Q -VALUE DETERMINATIONS FOR HIGHLY FORBIDDEN AND ULTRA-LOW Q -VALUE β -DECAYS

By

Rachel Nicole Sandler

Nuclear mass measurements are important in a wide variety of scientific fields, from low-precision requirements of molecular identification in analytical chemistry to high-precision tests of fundamental symmetries. Penning trap mass spectrometry (PTMS) is currently the most precise and accurate atomic mass measurement technique. This thesis work used two PTMS techniques to measure the Q -values of two rare decay processes: highly-forbidden β -decays and ultra-low Q -value β -decays. The Q -value is the energy released during a decay and, in the case of β^- -decay and electron capture- (ϵ -) decay, is equal to the mass-energy difference between a parent atom and its daughter atom.

Forbidden decays occur when the initial state in the parent and final state in the daughter nuclei have different total angular momenta and/or parities, leading to the final state leptons being emitted with orbital angular momentum $L \neq 0$. These decays have extremely long half-lives, ranging from $\sim 1 \times 10^9$ to $\sim 1 \times 10^{17}$ years and beyond. This makes them very difficult to detect, as the signal is easily overwhelmed by background. Improvements in low-background techniques and technology has led to an increase in β -decay spectra measurements of these highly-forbidden decays. However, the end-point energies determined from these spectra, which correspond to the Q -values of the decays, often have large uncertainties. The Q -value enters into the phase space factor for the decay, which is used to compute, for example, the shape factor of the β -decay spectrum and the half-life. Therefore, it needs to be as precise as possible to have a meaningful comparison with the experimental data.

Independent, precise Q -value measurements performed with a Penning trap can improve the theoretical spectrum shape calculations and systematically test the new experimental spectra measurements. Q -value measurements for the decay of $^{138}\text{La}\rightarrow^{138}\text{Ba}$ (ϵ -decay) and $^{138}\text{La}\rightarrow^{138}\text{Ce}$ (β -decay) were performed at the Low Energy Beam Ion Trap (LEBIT) facility at the National Superconducting Cyclotron Laboratory (NSCL), using a method known as Time of Flight-Ion Cyclotron Resonance (TOF-ICR). The motivation, procedure, and results of this experiment are presented in the first half of this thesis.

Ultra-low Q -value decays are defined as those for which the decay energy is less than ~ 1 keV. Such a decay can occur between the ground state of the parent and an excited nuclear state in the daughter. These low Q -value decays could allow for very sensitive probing of the absolute neutrino mass, and provide a testing ground for nuclear theory at these energy extremes. Q -values for the potential ultra-low Q -value decay candidates $^{115}\text{Cd}\rightarrow^{115}\text{In}$, $^{113}\text{Ag}\rightarrow^{113}\text{Cd}$, and $^{112}\text{Ag}\rightarrow^{112}\text{Cd}$ were measured at the Canadian Penning Trap (CPT) facility at Argonne National Laboratory (ANL), using a method known as Phase Imaging-Ion Cyclotron Resonance (PI-ICR). The motivation, procedure, and results of this experiment are presented in the second half of this thesis. Additionally, Q -values for the ultra-low Q -value decay candidates $^{89}\text{Sr}\rightarrow^{89}\text{Y}$ and $^{139}\text{Ba}\rightarrow^{139}\text{La}$ were measured at the LEBIT facility.

TABLE OF CONTENTS

LIST OF TABLES	ix
LIST OF FIGURES	xii
KEY TO ABBREVIATIONS	xix
Chapter 1 Introduction	1
1.1 Motivation for Mass Measurements	1
1.2 Penning Trap Mass Spectrometry	5
1.3 β -Decay Q -value Measurements	7
I Highly-Forbidden Decays	10
Chapter 2 Introduction to Highly-Forbidden Decays	11
2.1 Studying Highly-Forbidden Decays	12
2.2 Spectrum Measurement of ^{138}La	18
Chapter 3 The LEBIT Facility	24
3.1 Offline Sources at LEBIT	24
3.1.1 The Laser Ablation Source	25
3.1.2 The Plasma Ion Source	26
3.2 The Beam Cooler-Buncher	28
3.3 The Penning Trap and Magnet	31
3.4 Time of Flight-Ion Cyclotron Resonance	33
3.4.1 Mechanism	33
3.4.1.1 Cleaning of Contaminant Ions	36
3.4.2 Magnetic Field Calibration	37
3.4.3 Data Analysis	40
3.4.3.1 Direct Measurements	41
3.4.3.2 Indirect Measurements	42
3.4.3.3 The Birge Ratio	43
Chapter 4 Measurement of ^{138}La β- and ϵ-Decay Q-values	44
4.1 Direct Measurement of the ^{138}La β -Decay Q -value	45
4.2 Indirect Measurement of the ^{138}La β -Decay Q -value	49
4.3 Checking Systematics	54
4.4 Theoretical Calculations	56
4.4.1 Calculating the β -decay Spectrum Shape	56
4.4.2 Calculating the Electron capture Probability Ratios	57

II	Ultra-Low Q-Value Decays	59
Chapter 5	Introduction to Ultra-Low Q-Value Decays	60
5.1	Studying Ultra-Low Q -value Decays	60
5.2	Theoretical Calculations of Ultra-low Q -value Decays	63
Chapter 6	The CPT Facility	70
6.1	CARIBU	70
6.1.1	The Gas Catcher	72
6.1.2	The Isobar Separator	73
6.2	The Multi Reflection Time of Flight Mass Separator	75
6.3	The Stable Ion Source	76
6.4	The Penning Trap and Magnet	76
6.5	Phase Imaging Ion Cyclotron Resonance	78
6.5.1	Mechanism	78
6.5.2	Magnetic Field Calibration	81
6.5.3	Contamination Separation	82
Chapter 7	Measurement of $^{112,113}\text{Ag}$ and ^{115}Cd β-Decay Q-values	84
7.1	First Experiment—October 2016	85
7.1.1	Data Collection	85
7.1.2	Data Analysis	86
7.2	Testing Systematics—January 2017	89
7.2.1	Data Collection	89
7.2.2	Data Analysis	90
7.2.3	Correcting the Data from the First Experiment	95
7.3	Second Experiment—November 2018	97
7.3.1	Data Collection	97
7.3.2	Data Analysis	98
7.4	Combining the Data and Concluding	98
Chapter 8	Measurement of ^{89}Y and ^{139}La Atomic Masses	102
8.1	Measurements of ^{89}Y and ^{139}La Atomic Masses	104
8.2	Analysis of ^{89}Sr and ^{139}Ba Decay	108
III	Conclusion	110
Chapter 9	Summary and Outlook	111

LIST OF TABLES

Table 1.1:	The typical mass precisions required for a variety of different subfield applications.	2
Table 2.1:	The orbital and total angular momentum values and parity changes of various classes of β -decay.	13
Table 4.1:	The natural abundances of the isotopes used in this experiment. . .	45
Table 4.2:	Measured frequency ratios, $f_c(\text{parent})/f_c(\text{daughter})$, of $^{138}\text{La}^+$, $^{138}\text{Ba}^+$, and $^{138}\text{Ce}^+$ against each other for direct Q -value measurements. The uncertainties provided for \bar{R} include inflation by the Birge Ratio where necessary (see Sec. 3.4.3.3).	47
Table 4.3:	Absolute mass measurements of ^{138}La and ^{138}Ce , given as the mass excess, calculated using ^{138}Ba as a reference ion. The column DM is the amount the measured mass excess deviates from the AME 2016.	48
Table 4.4:	Q -values based on the direct measurement of f_{cd}/f_{cp} and absolute mass measurements, along with the 2016 AME value.	49
Table 4.5:	Absolute mass measurements of ^{138}Ba and ^{138}Ce , given as the mass excess, calculated using ^{136}Xe as a reference ion. The column DM is the amount this measured mass excess deviates from the AME 2016.	53
Table 4.6:	Mass excesses, ME, for ^{138}Ba , ^{138}La , and ^{138}Ce . The results are compared to those listed in the AME 2016 [1]. The column ΔM is calculated as $\text{ME}_{\text{LEBIT}} - \text{ME}_{\text{AME2016}}$	54
Table 4.7:	Absolute mass measurements of ^{136}Ba and ^{134}Xe , given as the mass excess, calculated using ^{136}Xe as a reference ion. The column DM is the amount the measured mass excess deviates from the AME 2016.	55
Table 4.8:	Adjusted parameters of the experimental shape factor $C_{\text{exp}}(W) = 1 + aW + bW^2$, to be applied on the theoretical shape factor to get the measured spectrum from [22]. Fitting procedure has been applied using the AME 2016 Q -value and the LEBIT Q -value.	56
Table 4.9:	Theoretical predictions of the capture probability ratios for ^{138}La , using the AME 2016 Q -value and the LEBIT Q -value, compared with experimental results made by Quarati, <i>et al.</i>	58

Table 5.1:	A list of possible ultra-low Q -value decay candidates, from [50, 55, 56]. The column E^* gives the excitation energy of the daughter nucleus. The column Q_{UL} is calculated as $Q_{GS} - E^*$	66
Table 7.1:	The list of potential ultra-low Q -value decay candidates studied using the Canadian Penning Trap at Argonne National Laboratory. Q_{gs} values were obtained using mass data from the AME 2016 [1]. The column E^* gives the excitation energy of the daughter nucleus from the NNDC [43]. The column Q_{UL} is calculated as $Q_{GS} - E^*$	85
Table 7.2:	The parent-daughter ion pairs measured in October of 2016, along with the accumulation times for each and the number of measurements taken for each accumulation time.	86
Table 7.3:	The average Q -values measured by CPT in October of 2016, along with the ranges measured and values from the AME 2016 [1].	87
Table 7.4:	The baseline and frequencies of the sine waves fit to the data seen in Figs. 7.3 and 7.4. The baseline is expected to be the actual cyclotron frequency of the ions measured, while the frequency is the magnetron frequency of the system.	94
Table 7.5:	The Q -values measured for the decay $^{115}\text{In} \rightarrow ^{115}\text{Sn}$, using the corrected data from Table 7.4 compared to the AME2016 [1]. The column ΔQ is calculated as CPT-AME.	94
Table 7.6:	The Q -values measured at the CPT facility in October of 2016, shown in Fig. 7.8, with the AME 2016 values for comparison.	96
Table 7.7:	The Q -values measured at the CPT facility in November of 2018, shown in Fig. 7.10, with the AME 2016 values for comparison. The bolded values are weighted averages.	100
Table 7.8:	The Q -values measured at the CPT facility using combined data from the October 2016 experiment and the November 2018 experiment, shown in Fig. 7.11, with the AME 2016 values for comparison.	101
Table 8.1:	The list of potential ultra-low Q -value β -decay candidates studied using the LEBIT facility at the National Superconducting Cyclotron Laboratory, using information from the AME 2016 [1] and the NNDC [43]. The column E^* gives the excitation energy of the daughter nucleus. The column Q_{UL} is calculated as $Q_{GS} - E^*$	102

Table 8.2:	Absolute mass measurements of ^{89}Y and ^{139}La , given as the mass excess. The column ΔME is the amount this measured mass excess deviates from the AME 2016.	106
Table 8.3:	Mass excesses for ^{89}Sr and ^{139}Ba , from the AME 2016.	109
Table 8.4:	Q -values based on the absolute mass measurements in Table 4.3 and Eqn. 1.5. The column E^* gives the excitation energy of the daughter nucleus. The result for the ultra-low Q -value decay branch is calculated as $Q_{UL} = Q_{GS} - E^*$	109

LIST OF FIGURES

Figure 1.1:	The chart of the nuclides, with each nuclide colored according to its known mass precision, using data from the most recent Atomic Mass Evaluation, AME 2016.	4
Figure 1.2:	A diagram of a high-precision Penning trap used for measurements of radioactive isotopes, taken from [6]. This diagram shows the compensation electrodes, introduced in order to counteract the distortion effects the endcap holes have on the electric field within the trap.	6
Figure 1.3:	Feynman diagrams of the mechanisms of β^- decay (on the left) and β^+ decay (on the right).	8
Figure 1.4:	A Feynman diagram of the mechanism of electron capture (ϵ)-decay.	9
Figure 2.1:	The mechanism of β -decay. J is total angular momentum and π is parity, while i denotes the initial parent state and f denotes the final daughter state.	12
Figure 2.2:	The effect found by Haaranen <i>et al.</i> of how altering the value of the axial-vector component of the weak coupling constant, g_A , can change the shape of the theoretical spectra [20].	15
Figure 2.3:	An example of the spectral-shape method (SSM) of altering the values of the weak coupling constants, g_V and g_A , to fit a theoretical model to existing experimental data, thus extracting information about the true values of the constants [20].	16
Figure 2.4:	Examples of the effects of changing the value of g_A on the theoretical β -decay spectra of second-forbidden decays. Shown here are ^{129}I (unique) and ^{93}Zr , ^{99}Tc , ^{125}Cs , and ^{137}Cs (all non-unique) [19]. It can be seen that, other than ^{99}Tc , which changed shape when $g_A \approx g_V$, changing the value of g_A for these decays has much less of an effect than on the fourth-forbidden decays examined in [20].	17
Figure 2.5:	The decay scheme of ^{138}La , which can decay via β -decay to ^{138}Ce or via ϵ -decay to ^{138}Ba . Both of these decays are second-forbidden, unique decays and have half-lives on the order of 10^{11} years.	19

Figure 2.6:	Comparison of β -decay continuum spectra of ^{138}La experiment and theory from [21]. Line 1 is the classically calculated theoretical curve while lines 2 and 3 are experimental spectra measured using the coincidence method and the convolution method, respectively.	20
Figure 2.7:	Comparison of β -decay continuum spectra of ^{138}La experiment and theory from [22]. The blue dotted line is the classical theoretical calculation and the black solid line is the experimental spectrum, found using the coincidence method. The gray band is the new theoretical calculation. The thickness of the gray band shows the uncertainty in the theory caused by the uncertainty in the endpoint energy (Q -value).	21
Figure 2.8:	Fitting a theoretical spectrum to the experimental data of ^{241}Pu β -decay, from [24]. The green curve is the classical calculation, the red curve includes the screening correction, and the blue curve includes both the screening correction and the exchange correction.	22
Figure 3.1:	A schematic of the relevant section of the LEBIT (Low Energy Beam Ion Trap) facility at the NSCL.	25
Figure 3.2:	A schematic of the Laser Ablation Source.	26
Figure 3.3:	The targets used with the LAS, taken from [29]. Picture (a) shows a variety of targets. Clockwise from the top left is a single carbon target, a dual carbon-zirconium target, a dual molybdenum-zirconium target, and a single titanium target. Picture (b) shows the single carbon target mounted on the target holder, which is controlled by a stepper-motor. Also visible is the path the laser takes along the target, seen here as a circular groove.	27
Figure 3.4:	A picture of the Thermal Ion Source chamber, with a USD 25 cent piece for scale. Shown here is an older chamber, composed of boron nitride, while the newer chamber is made of alumina. At the end of the chamber, the anode plate is visible through the endcap.	28
Figure 3.5:	Photos of the LEBIT beam cooler-buncher, used to prepare beam for delivery to the Penning trap, shown here in two parts. On the left are the pre-cooler and the micro-RFQ, shown with an NSCL coffee mug for scale. On the right is the buncher.	29
Figure 3.6:	The LEBIT Penning trap, shown here with one endcap removed and a bottle cap for scale.	31

Figure 3.7:	The superposition of an ion’s three normal modes of motion within the Penning trap. The frequencies of the reduced cyclotron motion and the magnetron motion add to the true cyclotron frequency of the trapped ions.	33
Figure 3.8:	A diagram showing the conversion between magnetron and cyclotron motion in a Penning trap. The ion initially begins with pure magnetron motion, shown in red. The quadrupolar RF pulse drives the reduced cyclotron motion and increases its radius while decreasing the magnetron radius, as seen with the growing black circles in part (a). When the applied RF pulse matches the cyclotron frequency of the trapped ion, the magnetron motion is fully converted and the radius of the reduced cyclotron motion matches that of the initial magnetron motion, as seen with the growing black circles in part (b).	35
Figure 3.9:	An example of a time of flight-ion cyclotron resonance curve, shown here with ^{138}La . The applied RF quadrupole excitation pulse is scanned over a range of frequencies, which includes the true cyclotron frequency of the trapped ions. The data are then fit with a theoretical curve, shown here as a red line, the minimum of which is the cyclotron frequency.	36
Figure 3.10:	The LEBIT magnet, a 9.4 Tesla superconducting solenoid.	38
Figure 3.11:	An illustration explaining how reference measurements are used to calibrate LEBIT’s magnetic field. An ion of well-known mass is measured before and after each measurement of the ion of interest. The two points of the reference ion measurements are then linearly interpolated to find the cyclotron frequency of the reference at the time the measurement of the ion of interest is taken.	39
Figure 4.1:	Cyclotron frequency ratio measurements for $^{138}\text{La}^+ / ^{138}\text{Ce}^+$, with the 1σ uncertainty in \bar{R} shown by the shaded region.	46
Figure 4.2:	The LEBIT direct measurement of the β -decay Q -value of ^{138}La decaying to ^{138}Ce , compared to Quarati <i>et al.</i> , the AME 2016, and the AME 2012. It can be seen that there is strong agreement between the Quarati measurement and this measurement, though this measurement is nearly an order of magnitude more precise. It is also important to note that the AME 2016 value includes the Quarati measurement, which was the most precise value at the time.	50
Figure 4.3:	An example of a resonance of $^{138}\text{Ce}^+$ showing a significant amount of $^{138}\text{Ba}^+$ contamination. In this example, the ^{138}Ba (right) is coming at a rate of approximately five times the amount of ^{138}Ce (left).	52

Figure 4.4:	The weighted average Mass Excesses measured in this work compared to the AME 2016 values.	53
Figure 4.5:	The Mass Excesses measured in this work to check for systematic shifts compared to the AME 2016 values.	55
Figure 4.6:	The measured ^{138}La β -decay spectrum by Quarati <i>et al.</i> (black line) fit using the LEBIT Q -value. The green line shows the classical theoretical calculation while the red line includes the experimental shape factor, C_{exp} . The inset shows the shape factor calculation using the AME 2016 Q -value versus using the LEBIT Q -value.	57
Figure 5.1:	A schematic showing an ultra-low Q -value β -decay from the ground state of the parent to an excited state of the daughter.	61
Figure 5.2:	A sample β -decay spectrum (on the left) and a closer image of the possible shapes of the spectrum at the endpoint (on the right). An example spectrum where the electron neutrino is massless is shown in blue, while an example spectrum where the electron neutrino has a mass of 1 eV is shown in red. Decays with smaller Q -values have a greater percentage of statistics in this crucial endpoint region.	63
Figure 5.3:	A plot from [48] of the HADES half-life measurement plotted against the JYFLTRAP (both [51]) and FSU (labeled BJM) ([52]) ultra-low Q -value measurements of $^{115}\text{In} \rightarrow ^{115}\text{Sn}$. The grey band on the graph is the theoretical relationship between half-life and Q -value, shown here with 30% confidence intervals. The discrepancy between experiment and theory points to missing atomic interference effects causing the half-life to be underestimated.	65
Figure 5.4:	A plot from [57] of their theoretical calculations for $^{115}\text{Cd} \rightarrow ^{115}\text{In}$. The dark grey band on the graph is the theoretical relationship between half-life and Q -value, calculated using multiple values of the axial-vector coupling constant, g_A , and multiple scenarios for the QRPA (quasiparticle random-phase approximation) phonon fits. The light grey band shows the estimated systematic error in the calculations.	68
Figure 6.1:	A schematic of the CaRIBU source and the beamline leading to the CPT facility.	71
Figure 6.2:	The portion of the chart of the nuclides containing ^{252}Cf fission fragments, from [60]. The color corresponds to the yield of the nuclide per 100 fissions of ^{252}Cf	72

Figure 6.3:	A schematic of the CARIBU isobar separator, from [63]. Q are quadrupole doublets, S are sextupole singlets, and M is an electrostatic multipole.	74
Figure 6.4:	The mass separation of ion species using the MR-TOF, from [64]. The top plot shows the initial bunch, with minimal separation of ion species after 40 cycles, with 2 reflections per cycle. The middle plot shows the time of flight separation of the desired ions and the contaminants after 200 cycles, and the bottom plot shows the same after 600 cycles.	77
Figure 6.5:	The Canadian Penning Trap (CPT), shown here with a Canadian gold dollar for scale.	78
Figure 6.6:	A schematic of the tower containing the CPT, from [70].	79
Figure 6.7:	A diagram of the pulse timings for PI-ICR. Step 1 establishes the center of the detector. Step 2 creates a reference spot. Step 3 creates the final spot. The total trap time is the same for steps 2 and 3. . .	80
Figure 6.8:	A diagram of the method of PI-ICR, from [12]. In the schematic view in the upper left, spot (1) is the center of the position-sensitive detector, spot (2) is the location of the reference spot, taken with $t_{acc} = 0$, and spot (3) is the final spot, taken with $t_{acc} > 0$	81
Figure 6.9:	An example of the separation of contamination using PI-ICR, from [71]. Shown here are the projection of ions on the position-sensitive detector as well as histograms of the measured phases of the ions for 0, 2, and 5 ms accumulation times. The ions and contaminants, ^{142}Cs , ^{142}Xe , and ICH_3 , are labeled in the histograms as they are resolved.	83
Figure 7.1:	Data taken at the CPT facility in October of 2016. The top shows the measured $^{112}\text{Ag} \rightarrow ^{112}\text{Cd}$ Q -values while the bottom shows the $^{115}\text{Cd} \rightarrow ^{115}\text{In}$ Q -values. The red bands show the uncertainty in the AME 2016 [1].	88
Figure 7.2:	The measured radii for ^{112}Ag in October of 2016. The red band shows the average radius and its uncertainty.	89
Figure 7.3:	Measured frequencies, with sinusoidal fits, taken of ^{115}Sn in January of 2017. The accumulation time, t_{acc} , was varied by a hundred microseconds at a time over a range of one millisecond to understand the effect t_{acc} has on the measured frequency at CPT.	91

Figure 7.4:	Measured frequencies, with sinusoidal fits, taken of ^{115}In in January of 2017. The accumulation time, t_{acc} , was varied by a hundred microseconds at a time over a range of one millisecond to understand the effect t_{acc} has on the measured frequency at CPT.	91
Figure 7.5:	Measured radii, with sinusoidal fits, taken of ^{115}In in January of 2017. The accumulation time, t_{acc} , was varied by a hundred microseconds at a time over a range of one millisecond to understand the effect t_{acc} has on the measured frequency at CPT.	92
Figure 7.6:	A diagram of the hypothesized cause of the sinusoidal fluctuations of the radius and frequency at the CPT. If not all of the magnetron motion of the ion is converted into cyclotron motion, the residual magnetron motion will cause the ion to precess around the greater orbit. Here, the expected motion is the solid black line, while the residual magnetron motion is the dotted black line. The spot on the detector is the filled blue circle.	93
Figure 7.7:	Frequency data for ^{115}Sn and ^{115}In , with Eq. 7.3 applied and used to correct the systematic shift in the frequency.	95
Figure 7.8:	Q -values for the decays measured in October of 2016, found by applying Eq. 7.3 to correct the systematic shift in the model. The black points are the CPT measurements and the red bands show the uncertainty in the AME 2016.	96
Figure 7.9:	Measured frequencies, with a sinusoidal fit, taken of ^{112}Cd at the CPT facility in November of 2018. The accumulation time, t_{acc} , was varied by a hundred microseconds at a time over a range of one millisecond to allow for fitting and correction of the systematic error.	99
Figure 7.10:	Data taken at the CPT facility in November of 2018. The points show the measured Q -values with the AME 2016 values subtracted out. The red bands show the uncertainty in the AME 2016.	100
Figure 7.11:	Q -values measured at CPT, using combined data from the October 2016 experiment and the November 2018 experiment. The points show the measured Q -values with the AME 2016 values subtracted out. The red bands show the uncertainty in the AME 2016.	101
Figure 8.1:	The decay and level schemes for ^{89}Sr , on the left, and ^{139}Ba , on the right. ^{89}Sr has one potential ultra-low Q -value decay channel while ^{139}Ba has two, all shown by the dotted blue arrows.	103

Figure 8.2:	An example of a time of flight ion cyclotron resonance curve, shown here with ^{89}Y	105
Figure 8.3:	The mass excess (shown here as differences from the AME 2016) of ^{89}Y , calculated using two different references and two different excitation times. The red band is the weighted average for each reference.	107
Figure 8.4:	The weighted average Mass Excesses measured in this work compared to the AME 2016.	108

KEY TO ABBREVIATIONS

- ANL - Argonne National Lab
- ATLAS - Argonne Tandem Linac Accelerator System
- CCF - Coupled Cyclotron Facility
- CPT - Canadian Penning Trap
- DOE - Department of Energy
- LAS - Laser Ablation Source
- LEBIT - Low Energy Beam Ion Trap
- MR-TOF - Multi-Reflection Time of Flight
- NSCL - National Superconducting Cyclotron Laboratory
- NSF - National Science Foundation
- PI-ICR - Phase Imaging Ion Cyclotron Resonance
- PTMS - Penning Trap Mass Spectrometry
- SIS - Stable Ion Source
- TIS - Test Ion Source (also known as the Plasma Ion Source)
- TOF-ICR - Time of Flight Ion Cyclotron Resonance

Chapter 1

Introduction

*I'm supposed to introduce some joke here to hold your attention, so here is a smiley face
you should smile at.*



-Witek Nazarewicz

1.1 Motivation for Mass Measurements

Mass measurements on the molecular, atomic, and nuclear level are integral for a wide variety of scientific applications. Precision requirements range anywhere from $\delta m/m \approx 10^{-6}$ for chemistry applications, such as identification of molecular species, to $\delta m/m \lesssim 10^{-11}$ for metrology applications, such as precision determinations of fundamental constants and tests of the CPT (charge, parity, and time reversal symmetry) theorem. Typical precision requirements for a variety of subfields can be found in Table 1.1. Precision mass measurements of nuclei allow for the study of two important concepts in nuclear physics: binding energy and Q -value.

The binding energy of a nucleus can be understood using Einstein's well-known equation of mass-energy equivalence:

$$E = mc^2. \tag{1.1}$$

The binding energy of a nucleus is the energy that holds the protons and neutrons together.

Table 1.1: The typical mass precisions required for a variety of different subfield applications.

Research Area	$\delta m/m$
Chemistry	10^{-6}
Astrophysics	10^{-7}
Nuclear Physics	10^{-7} – 10^{-8}
Weak Interactions	10^{-8}
Rare Decays	10^{-8} – 10^{-9}
Atomic Physics	10^{-9}
Metrology	10^{-10} – 10^{-11}

It can be determined directly from the absolute mass of the nucleus, as the binding energy is the energy equivalent, from Eqn. 1.1, of the difference between the mass of the nucleus and the sum of the masses of the individual nucleons. Written as an equation, the binding energy of a nucleus is calculated via:

$$E_B = ([m_p Z + m_n(A - Z)] - M)c^2, \quad (1.2)$$

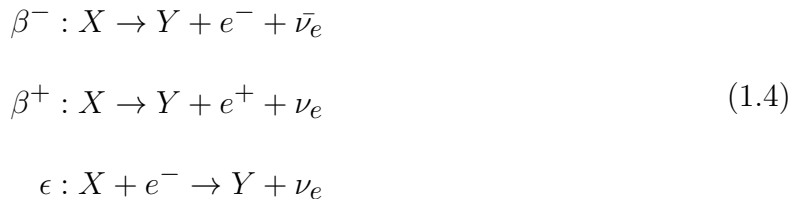
where M is the absolute mass of the atom, m_p is the proton mass, m_n is the neutron mass, Z is the proton number, and A is the mass number. This value is generally reported in units of keV. In nuclear physics, typically the “mass excess” is reported, rather than the binding energy, as it portrays the same information. Mass excess is defined as:

$$ME = (M - m_u(A))C, \quad (1.3)$$

where M is the absolute mass of the atom in atomic mass units, m_u is 1 atomic mass unit, A is the mass number, and C is the conversion factor from atomic mass units to the mass unit usually used in nuclear physics, $m_u = 931494.0954 \text{ keV}/c^2$. Note that beyond the conversion

factor, the mass excess and the binding energy differ minimally in their definition. For the binding energy, the proton and neutron are treated as having different masses. For mass excess, they are both approximated as 1 u.

The Q -value is the energy released or absorbed as a nucleus undergoes a nuclear reaction. For a nuclear decay, the Q -value is more specifically defined as the kinetic energy of the decay products. From Eqn. 1.1, it is known that this is the energy equivalent of the mass difference between the initial and final products. The three main processes relevant to nuclear β -decay are β^- -, β^+ - and ϵ -decay:



For β^- -and ϵ -decay, the Q -value can be further defined as the energy equivalent of the mass difference between the parent and daughter:

$$Q = (M_p - M_d)c^2,\tag{1.5}$$

where M_p is the mass of the parent atom and M_d is the mass of the daughter atom. For β^+ -decay, the mass of two electrons, m_e , must also be taken into account:

$$Q = (M_p - M_d - 2m_e)c^2.\tag{1.6}$$

Fig. 1.1 shows the Chart of the Nuclides, with each square colored based on the currently known mass precision according to the most recent Atomic Mass Evaluation, the AME

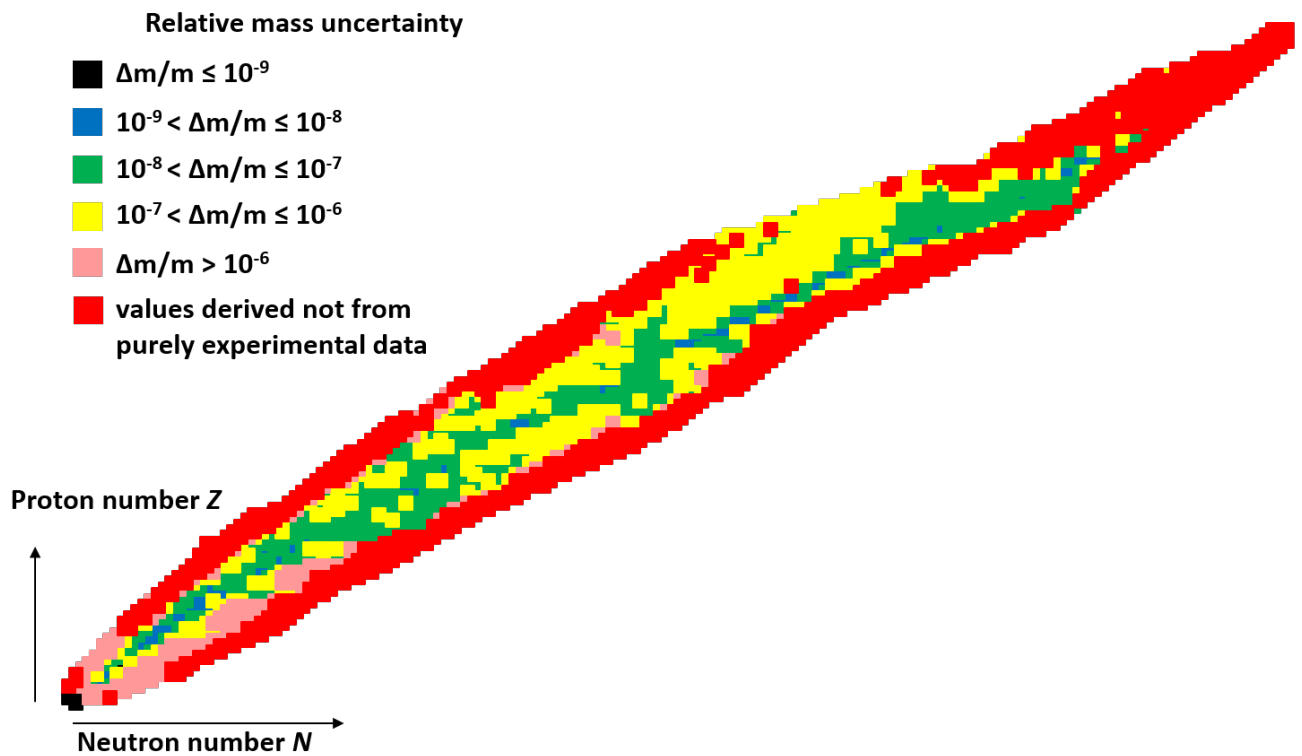


Figure 1.1: The chart of the nuclides, with each nuclide colored according to its known mass precision, using data from the most recent Atomic Mass Evaluation, AME 2016.

2016 [1]. As can be seen, nuclides near the valley of stability are known with precisions of around $\delta m/m \sim 10^{-8}$. Precision drops quickly, however, as one moves farther from stability, and very few of even the stable nuclides are known with precisions of 10^{-9} or better, necessary for the most precise tests of physics. Thus, mass measurement facilities around the world strive to improve mass measurements of both stable and unstable nuclei.

1.2 Penning Trap Mass Spectrometry

Of the wide range of mass spectrometry techniques currently available, Penning Trap Mass Spectrometry (PTMS) is the most accurate and precise method. Penning traps can trace their origin back to 1936, when Frans Penning published in *Physica* that a vacuum tube gauge could work with increased sensitivity by incorporating a magnetic field, which could increase the path length of electrons within the vacuum tube. Michael Holzschteier translates the paper as explaining, “with a magnetic field of sufficient strength, electrons, leaving the cathode, will miss the anode and return to the cathode - thereby reducing the anode current to zero, when the magnetic field is increased beyond a certain value... [2]” More than ten years later, in 1949, J. R. Pierce furthered the idea of confining charged particles using electric and magnetic fields by proposing “end hats” to constrain ions in the axial direction [3]. In the late 1950s and early 1960s, Hans Georg Dehmelt developed the first iteration of what is currently called the “Penning trap,” using hyperbolic electrodes and end caps to create a quadrupolar, electrostatic field for trapping electrons [4]. Dehmelt won the Nobel Prize in Physics in 1989 for developing the Penning trap and using it to perform a precise measurement of the electron g-factor [5]. He shared half of the prize with Wolfgang Paul, who developed the Paul trap.

While Penning traps have been utilized for a wide range of physics subfields, in the 1980s and early 1990s developments began towards utilizing Penning traps in pursuit of high precision mass measurements of rare isotopes [6–8]. Correction tube electrodes, in addition to correction ring electrodes, were introduced to compensate for imperfections in the quadrupolar electrostatic field caused by the relatively large injection and ejection holes that were required in the endcaps for capturing ions from rare isotope beams (see Fig. 1.2)

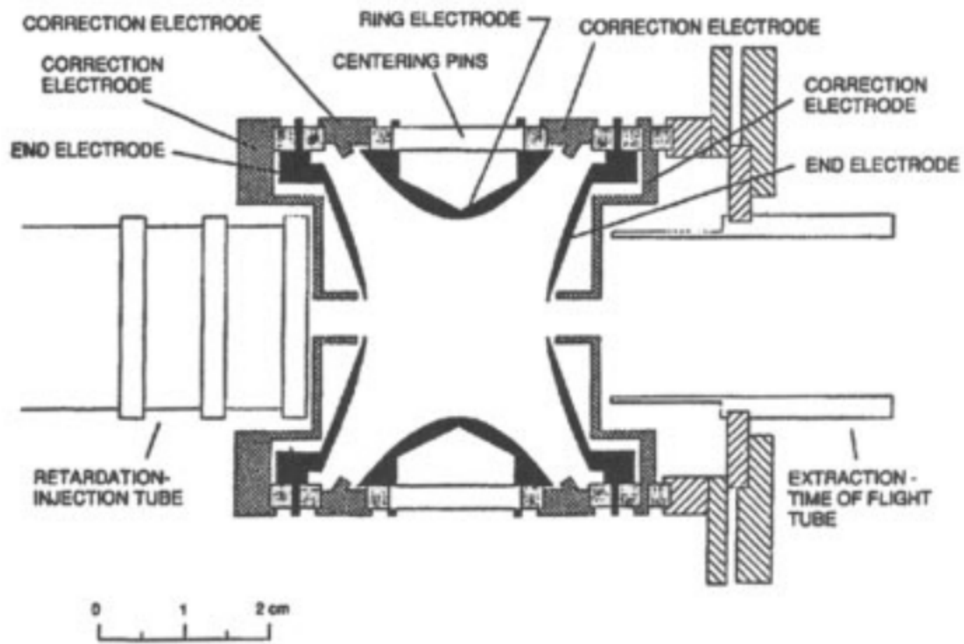


Figure 1.2: A diagram of a high-precision Penning trap used for measurements of radioactive isotopes, taken from [6]. This diagram shows the compensation electrodes, introduced in order to counteract the distortion effects the endcap holes have on the electric field within the trap.

and the first Penning trap for rare isotope mass measurement, ISOLTRAP at ISOLDE, CERN, came online in 1990 [9]. From there, Penning traps were implemented at various nuclear physics facilities around the world. Initially, Penning traps were only found at ISOL (Isotope Separation On Line) facilities, where rare isotopes are produced at rest inside a target and extracted at the low energy necessary for trapping. However, in the early 2000s the first experiments using gas cells to stop higher-energy beams were implemented, paving the way for the use of Penning traps at fragmentation facilities, where isotopes are produced at $\lesssim 100\text{MeV/u}$ [10, 11]. Over the years, different techniques have been developed for using Penning traps to measure nuclear masses. Time of Flight-Ion Cyclotron Resonance (TOF-ICR) is the original method of PTMS used by on-line Penning traps for nuclear physics applications and is discussed in detail in Chapter 3. More recently a new technique of Phase Imaging-Ion Cyclotron Resonance (PI-ICR) was developed [12]. This method is discussed in detail in Chapter 6.

1.3 β -Decay Q -value Measurements

β particle radiation was first discovered and named by Ernest Rutherford in 1899 [13]. Rutherford was studying radiation released by decaying nuclei and classified the three “rays” he observed as α , β , and γ rays based on their ability to penetrate matter, with α radiation having the least penetration and γ radiation having the most. The following year, Henri Becquerel measured the mass-to-charge ratio of Rutherford’s β particles and found it was identical to that of an electron, suggesting that a β particle emitted from a radioactive decay was an electron. This form of β -decay is known as β^- . It wasn’t until 1934, when Frédéric and Irène Joliot-Curie performed an experiment impinging α particles on aluminum, that

β^+ radiation was first observed [14]. The difference between β^- -decay and β^+ -decay can be seen in Fig. 1.3. In β^- -decay, a neutron decays into a proton, releasing an electron and an anti-electron neutrino. In β^+ -decay, a proton decays into a neutron, releasing a positron and an electron neutrino.

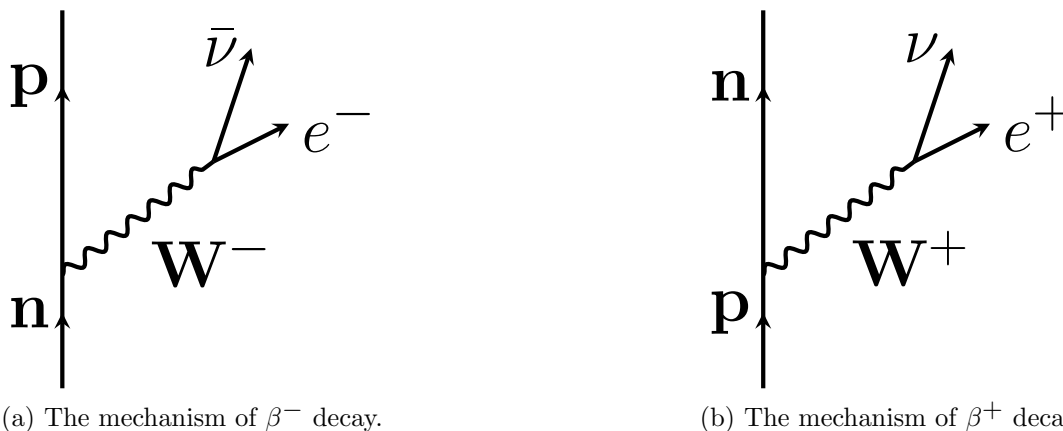


Figure 1.3: Feynman diagrams of the mechanisms of β^- decay (on the left) and β^+ decay (on the right).

Shortly after the Joliot-Curies' experiment was published, Gian-Carlo Wick first discussed the theory of electron capture [15]. Electron capture (ϵ)-decay is functionally identical to β^+ -decay in that the change from parent to daughter nucleus is the loss of a proton and the gain of a neutron. In ϵ -decay, however, an atomic electron is captured by a proton, allowing it to decay into a neutron and release an electron neutrino. This mechanism can be seen in Fig. 1.4. This flip, from a positron being released to an electron being absorbed, is known as crossing symmetry.

Collectively, these three decay mechanisms are called β -decay. β -decay gave the first evidence for the existence of the neutrino. While α -decay and γ -decay spectra have very narrow energy distributions, β -decay spectra, first measured in 1911 by Lise Meitner and Otto Hahn, have wide energy distributions which range from zero to an endpoint that de-

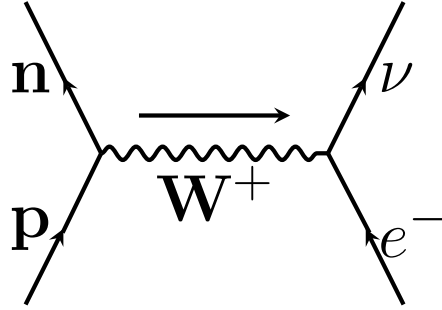


Figure 1.4: A Feynman diagram of the mechanism of electron capture (ϵ)-decay.

depends on the specific decay [16]. This is because the decay energy, equal to the Q -value, is split between the β particle (the electron) and an unobserved particle. This second particle was first called the “neutron” in 1930 by Wolfgang Pauli, but was renamed the “neutrino,” or “little neutron” by Enrico Fermi in 1931. Three years later, Fermi published his theory for β -decay, which included the creation of the neutrino [13].

Today, β -decays are studied for a wide variety of motivations, from determining the mass of the electron neutrino to testing fundamental symmetries. The two forms of β -decay that will be discussed in this thesis are highly-forbidden β -decay (discussed in detail in Chapter 2) and ultra-low Q -value β -decay (discussed in detail in Chapter 5).

Part I

Highly-Forbidden Decays

Chapter 2

Introduction to Highly-Forbidden Decays

Let us be brave and write down this long expression.

-Vladimir Zelevinsky

β -decays can be classified based on the orbital angular momentum relative to the nucleus (here on referred to as L) of the emitted radiation. In most β -decays, known as “allowed” decays, the leptons emitted have a total orbital angular momentum, L , equal to zero. For forbidden decays, however, the parent and daughter nuclear states have different total angular momenta or parities. In these cases, the emitted leptons must carry away angular momentum, which they do by having a non-zero total spin or total orbital angular momentum. These “forbidden” decays are further classified by the exact orbital angular momentum of the leptons. When $L = 1$, the decay is known as “first forbidden.” When $L = 2$, the decay is known as “second forbidden.” This pattern continues, with fourth forbidden being the highest order yet observed. These forbidden decays usually have extremely long half-lives, on the order of $\sim 10^9$ years or greater, with each additional level of forbiddenness further increasing the half-life by several orders of magnitude.

The forbidden decays can then be further separated into “unique” and “non-unique”

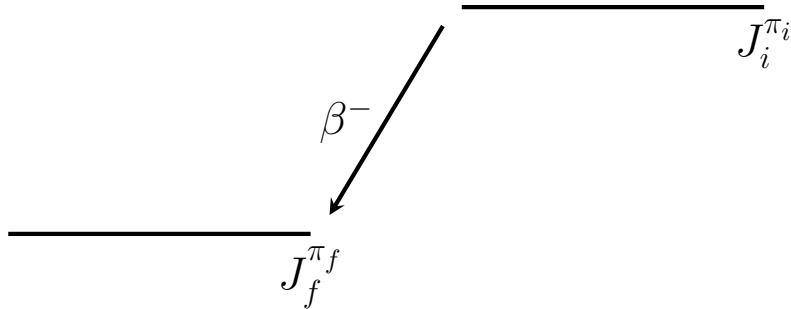


Figure 2.1: The mechanism of β -decay. J is total angular momentum and π is parity, while i denotes the initial parent state and f denotes the final daughter state.

decays. For “non-unique” decays, the orbital angular momentum of the emitted leptons, L , is equal to the change in the total angular momentum of the decay, $\Delta J = L$. For “unique” decays, there is a change in the spin of the leptons emitted in the decay, $S = s_1 + s_2$. Therefore, the orbital angular momentum of the emitted leptons is less than the change in the total angular momentum of the decay, $\Delta J = L + 1$, except for first forbidden decays, in which ΔJ can equal zero. For both of these categories, the change in parity of the decay, $\pi_f \pi_i$, is equal to $(-1)^L$.

2.1 Studying Highly-Forbidden Decays

In general, highly forbidden decays are of interest because they are very difficult to model theoretically. They depend on a wide variety of factors, including the weak coupling constants, g_V and g_A . On a particle physics level, β -decay is the conversion of an up quark to a down quark (for β^+ -decay) or the conversion of a down quark to an up quark (for β^- -decay). The remaining, unchanged quarks can be described as forming a “hadronic current” while the emitted leptons can be described as forming a “lepton current” [17, 18]. These currents are mediated via the W boson and can be expressed as a mixture of vector and axial-vector components. When describing β -decay as an interaction between nucleons,

Table 2.1: The orbital and total angular momentum values and parity changes of various classes of β -decay.

Forbiddenness	Uniqueness	L	$\Delta J = J_f - J_i $	$\pi_f \pi_i$
Allowed	Non-unique	0	0	1
Allowed	Unique	0	0,1	1
1st Forbidden	Non-unique	1	0,1	-1
1st Forbidden	Unique	1	2	-1
2nd Forbidden	Non-unique	2	2	1
2nd Forbidden	Unique	2	3	1
3rd Forbidden	Non-unique	3	3	-1
3rd Forbidden	Unique	3	4	-1
4th Forbidden	Non-unique	4	4	1
4th Forbidden	Unique	4	5	1
5th Forbidden	Non-unique	5	5	-1
5th Forbidden	Unique	5	6	-1

rather than quarks, these currents must be renormalized and the weak coupling constants are introduced. For a bare nucleon undergoing β -decay, the Conserved Vector Current theory (CVC) can be used to determine values for these weak coupling constants of $g_V = 1.00$ and $g_A = 1.27$ [19]. However, for β -decays of nuclei, many-body correlation effects come into account and the constants must be determined experimentally.

The weak coupling constant g_A is particularly important to understand, as the half-lives of neutrinoless double β -decays ($0\nu\beta\beta$) are dependent on g_A^4 . An observation of a $0\nu\beta\beta$ -decay would be groundbreaking, as it would prove that the neutrino is a Majorana particle and not a Dirac particle, meaning that it is its own antiparticle. In order to optimize experimental setups in terms of background requirements, amount of source material, etc., as well as increase chances of obtaining useful observations from experiments searching for $0\nu\beta\beta$, the theoretical predictions themselves must be optimized. One method of improving these theoretical predictions is to compare theoretical forbidden β -decay models to experimental

β -decay spectra. These models include g_A and g_V and can thus be used to “tune” the values of the weak coupling constants, in turn improving the theory to predict the half-lives of $0\nu\beta\beta$ -decays.

The theoretical β -decay spectra is described using the equation,

$$P(W_e)dW_e = \frac{G_F}{(\hbar c)^6} \frac{1}{2\pi^3\hbar} C(W_e) p_e c W_e (W_0 - W_e)^2 F_0(Z, W_e) dW_e, \quad (2.1)$$

where $P(W_e)dW_e$ is the probability of an electron to be emitted in the energy interval W_e to $W_e + dW_e$, G_F is the Fermi coupling constant, $C(W_e)$ is the shape factor, p_e is the electron momentum, W_0 is the endpoint energy, and $F_0(Z, W_e)$ is the Fermi function for β -decays [20]. W_e , W_0 , and p_e can be replaced with the unitless quantities $w_e = W_e/m_e c^2$, $w_0 = W_0/m_e c^2$, and $p = p_e c/(m_e c^2)$. The shape factor can be decomposed into its vector, axial-vector, and vector-axial-vector parts to explicitly include the weak coupling constants and rewritten as,

$$C(w_e) = g_V^2 C_V(w_e) + g_A^2 C_A(w_e) + g_V g_A C_{VA}(w_e). \quad (2.2)$$

In 2016, Haaranen *et al.* initiated a study at the University of Jyväskylä of the β -decay spectra of ^{113}Cd and ^{115}In , both of which are fourth-forbidden, non-unique β -decays. [20] In this study, they found that changing the values of g_V and g_A in the shape factor (Eq. 2.2) when calculating the theoretical decay spectra for the two isotopes dramatically changed the shape of the spectra (see Fig. 2.2). From this discovery, the group developed the “spectrum-shape method,” or SSM. This is a method of using experimental decay spectra data to probe

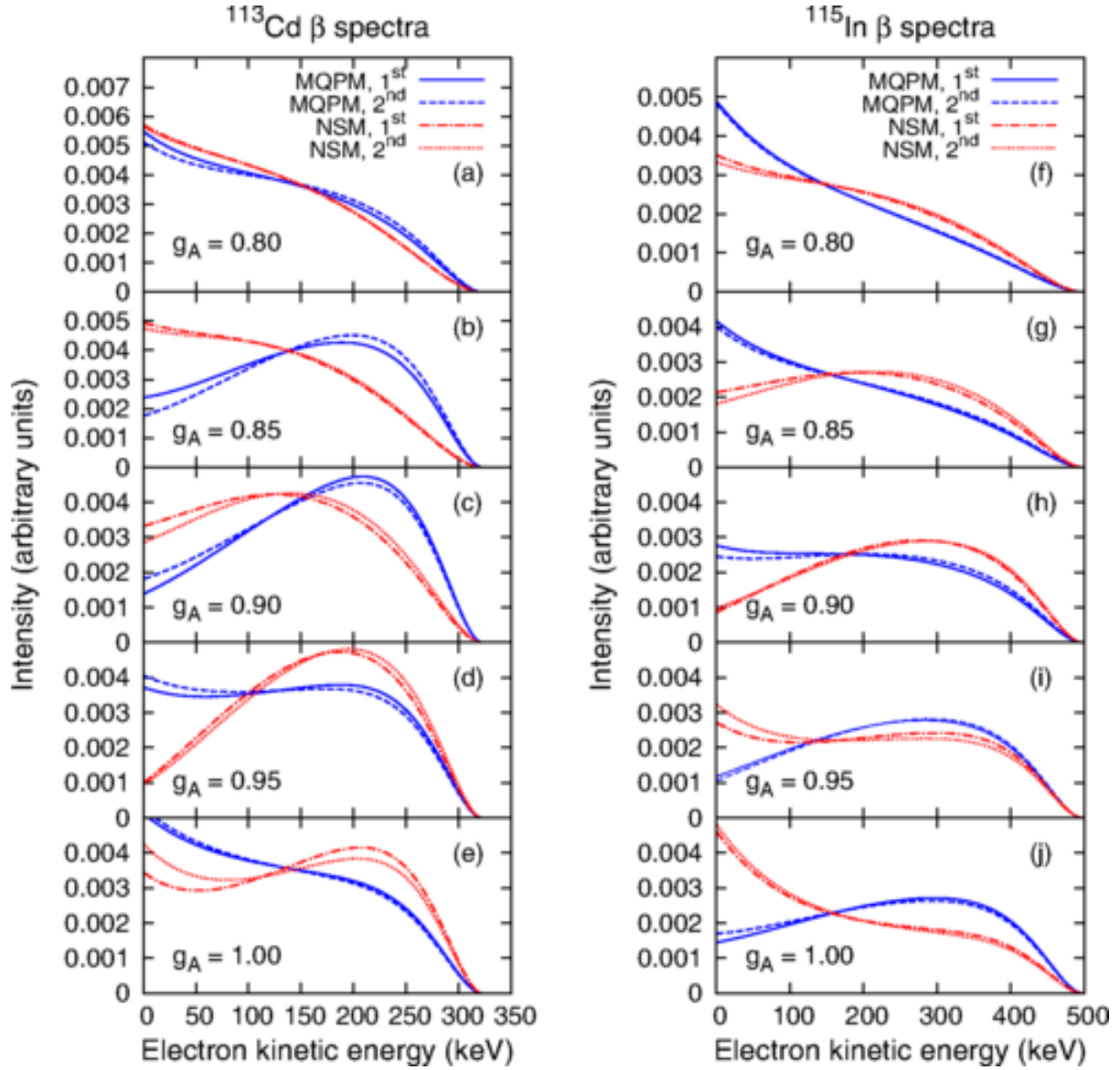


Figure 2.2: The effect found by Haaranen *et al.* of how altering the value of the axial-vector component of the weak coupling constant, g_A , can change the shape of the theoretical spectra [20].

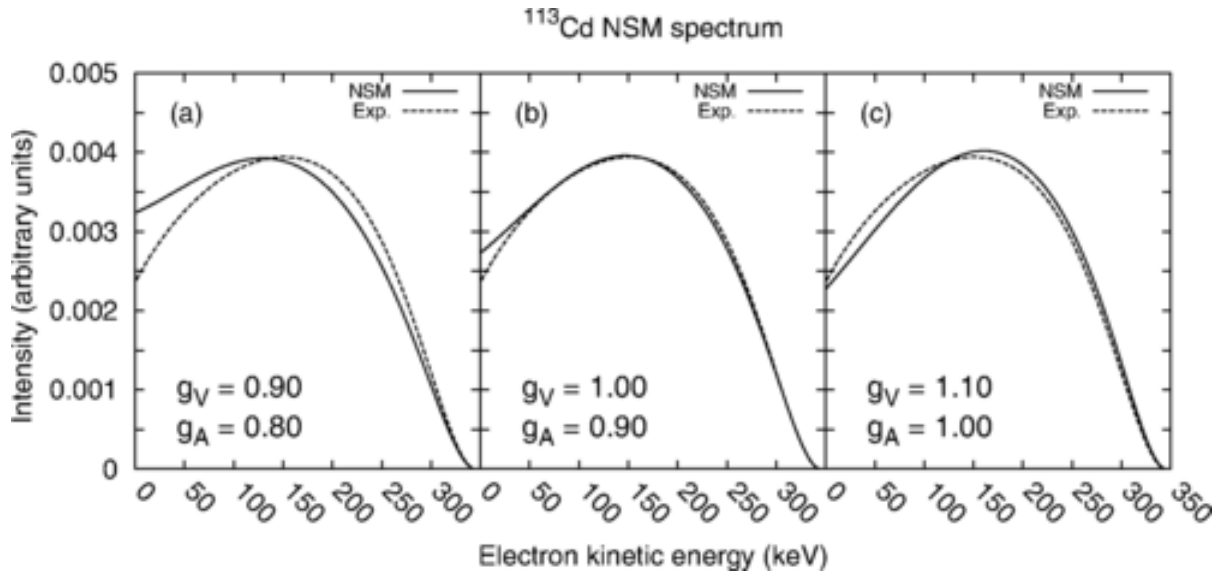


Figure 2.3: An example of the spectral-shape method (SSM) of altering the values of the weak coupling constants, g_V and g_A , to fit a theoretical model to existing experimental data, thus extracting information about the true values of the constants [20].

the values of g_V and g_A . By altering these two coupling constants and seeing what values allow the theory to match the data most closely, it is possible to extract information about the correct value of these constants. With this new information, theorists can be better prepared to predict important information about $0\nu\beta\beta$ -decay and thus may be able to give more insight to experimentalists seeking to measure said decays. In Fig. 2.3, an example can be seen of the SSM. In these plots, g_V and g_A are altered to fit the theoretical model to experimental data. This cannot be done unless the theoretical model is complete and accurate, however.

In 2017, the same group at the University of Jyväskylä expanded their spectral-shape method to look at a variety of β -decays for odd-A nuclei, from first- to fourth-forbidden, both unique and non-unique [19]. Unfortunately, it was found that first- and second-forbidden decays in general did not seem to be affected by changing the weak coupling constants the way third- and fourth-forbidden decays were (see Fig. 2.4). However, it was determined that

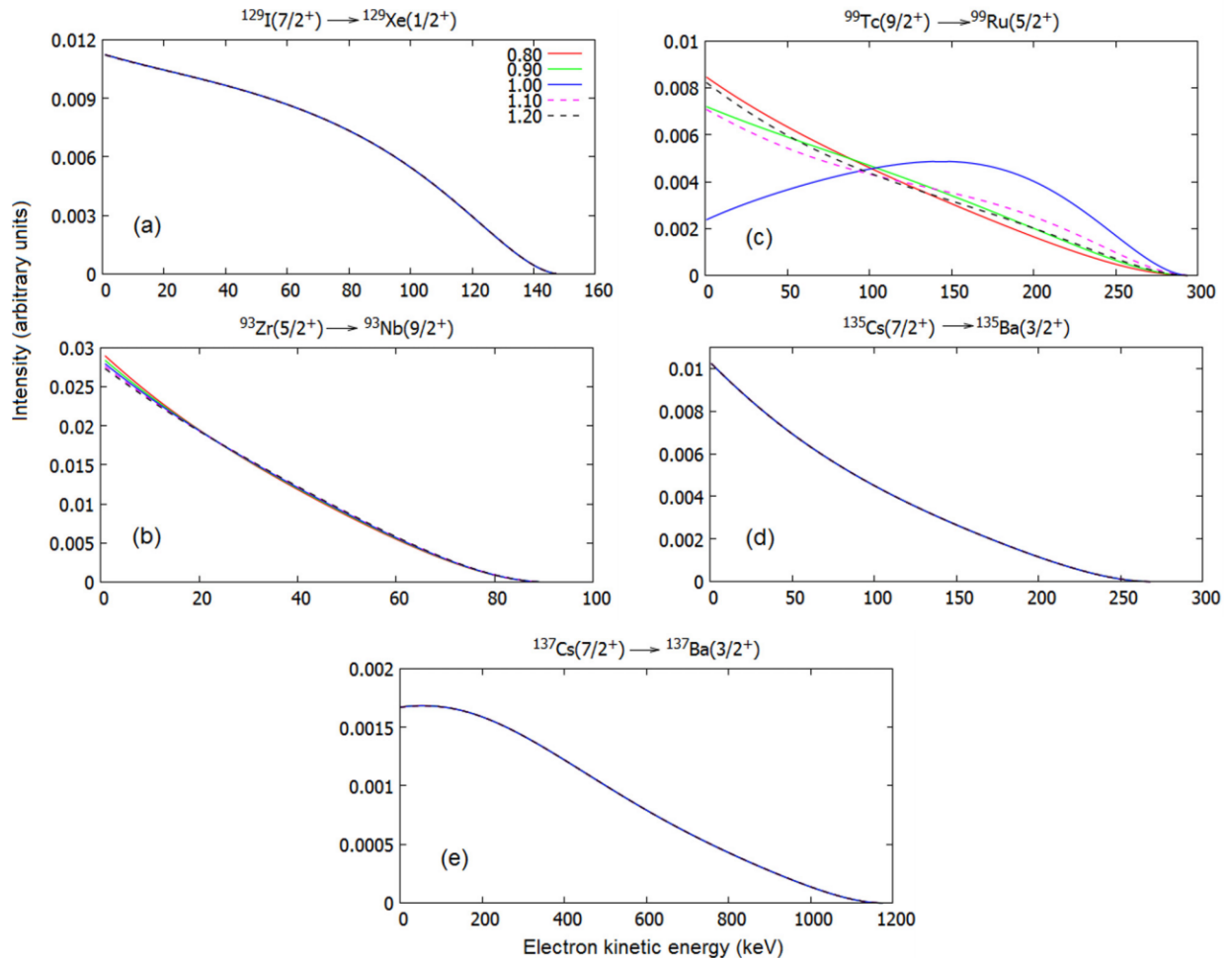


Figure 2.4: Examples of the effects of changing the value of g_A on the theoretical β -decay spectra of second-forbidden decays. Shown here are ^{129}I (unique) and ^{93}Zr , ^{99}Tc , ^{125}Cs , and ^{137}Cs (all non-unique) [19]. It can be seen that, other than ^{99}Tc , which changed shape when $g_A \approx g_V$, changing the value of g_A for these decays has much less of an effect than on the fourth-forbidden decays examined in [20].

they were still of great importance, as they can be used to determine the accuracy of the theoretical spectrum models. It also is uncertain if even- A nuclei behave similarly to odd- A nuclei or if perhaps those decays will be more greatly impacted by tuning g_V and g_A .

2.2 Spectrum Measurement of ^{138}La

^{138}La can decay via β -decay to ^{138}Ce or via ϵ -decay to ^{138}Ba (see Fig. 2.5). Both of these are second-forbidden, unique decays with half-lives on the order of 10^{11} years. Such long half-lives, combined with the low Q -values, make these β -spectra difficult to measure. However, the group of Quarati *et al.* was able to directly measure the β -decay spectrum of ^{138}La in 2012 [21]. This group used a LaBr_3 scintillator and measured the intrinsic activity from the 0.0190 natural abundance of ^{138}La within the detector. By using γ detectors in conjunction with the scintillator for background suppression coincidence measurements, the group was able to make a measurement of the β continuum spectrum of ^{138}La .

When Quarati *et al.* compared their experimental spectrum to the theoretical spectrum they found a large deviation between the two, particularly at lower energies (see Fig. 2.6). This discrepancy was theorized to be caused by missing screening corrections in the theory.

Four years later, in 2016, Quarati's group published an improved data set with a new theoretical calculation of the continuum spectrum [22]. The new theoretical spectrum included an additional screening correction and fit the experimental data far more closely (see Fig. 2.7). This screening correction takes into account the fact that the electron cloud "screens" the Coulomb field of the daughter nucleus. The emission of low energy electrons, which have wavelengths comparable to the size of the atom, is increased because the atomic electrons shrink the effective electric field of the bare nucleus [23].

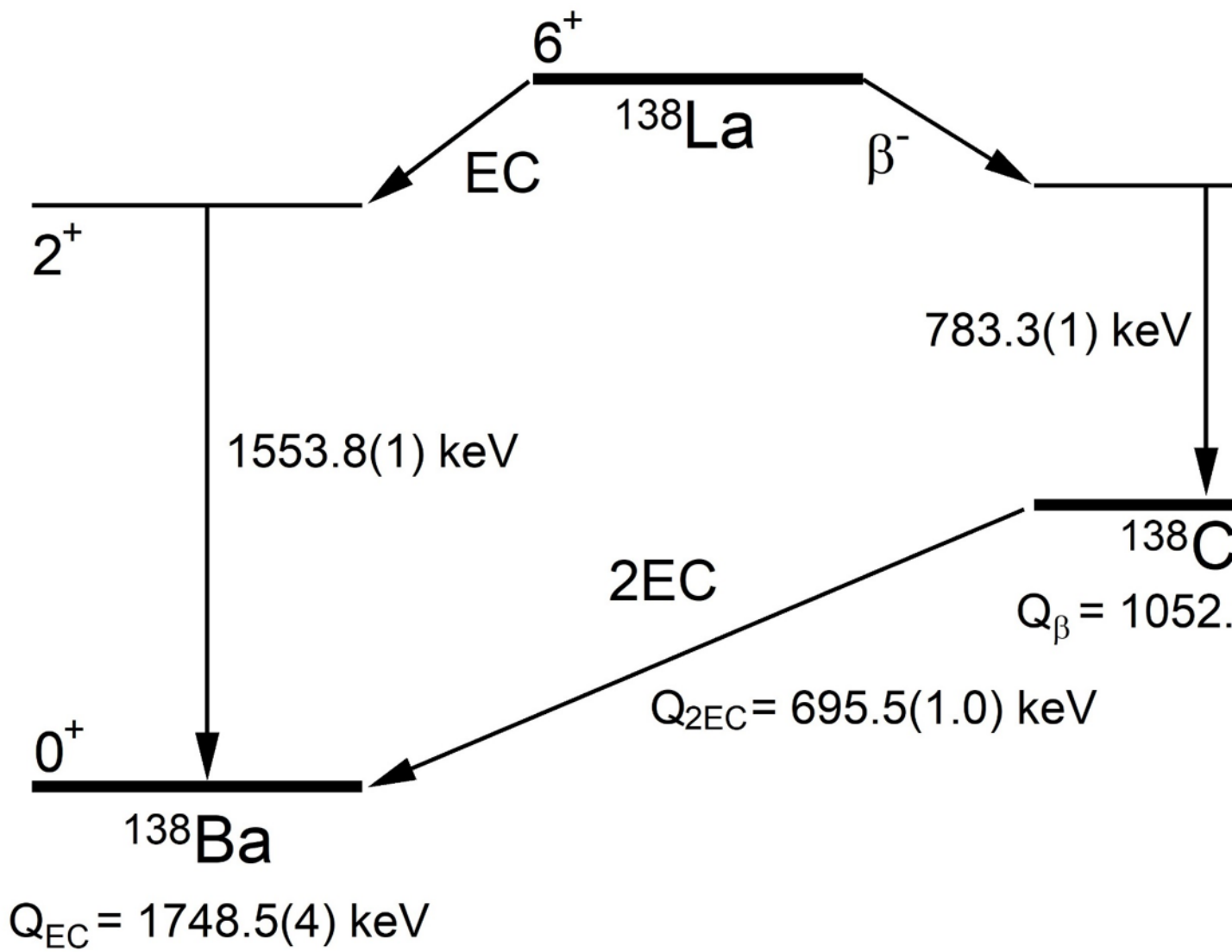


Figure 2.5: The decay scheme of ^{138}La , which can decay via β -decay to ^{138}Ce or via ϵ -decay to ^{138}Ba . Both of these decays are second-forbidden, unique decays and have half-lives on the order of 10^{11} years.

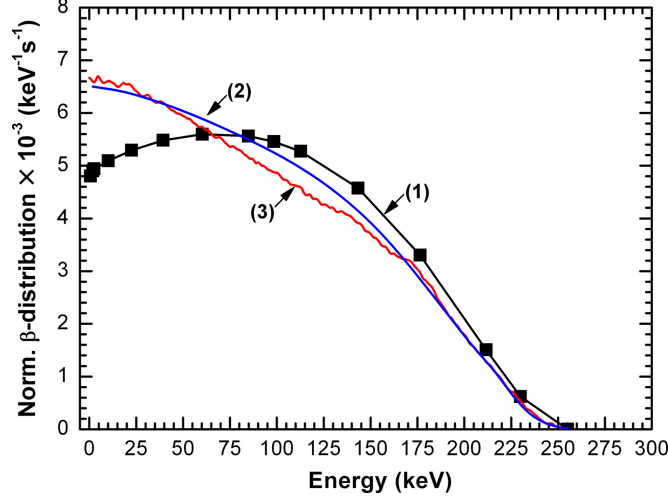


Figure 2.6: Comparison of β -decay continuum spectra of ^{138}La experiment and theory from [21]. Line 1 is the classically calculated theoretical curve while lines 2 and 3 are experimental spectra measured using the coincidence method and the convolution method, respectively.

The theoretical shape calculation, Eqn. 2.1, is found using the endpoint energy of the spectrum, or the ground-state to ground-state Q -value of the decay. Therefore, any uncertainty in the Q -value will cause an uncertainty in the theoretical calculation. This can be seen in Fig. 2.7 by the thickness of the gray band. To evaluate this uncertainty, Quarati *et al.* calculated the theoretical curve twice, once using their measured Q -value and adding its uncertainty and once using their measured Q -value and subtracting its uncertainty. These two calculations were used to determine the top and the bottom of the gray band.

Even with the newly included screening correction, it can be seen that the experimental and theoretical spectra deviate at low energies. This likely points to additional missing theoretical corrections. One potential source of missing information is the atomic exchange effect. This occurs when the β -particle is created in a bound orbital state of the daughter atom which corresponds to an occupied orbital of the parent. Instead of the created electron being released, it is captured in the orbital. Simultaneously, a second electron from the

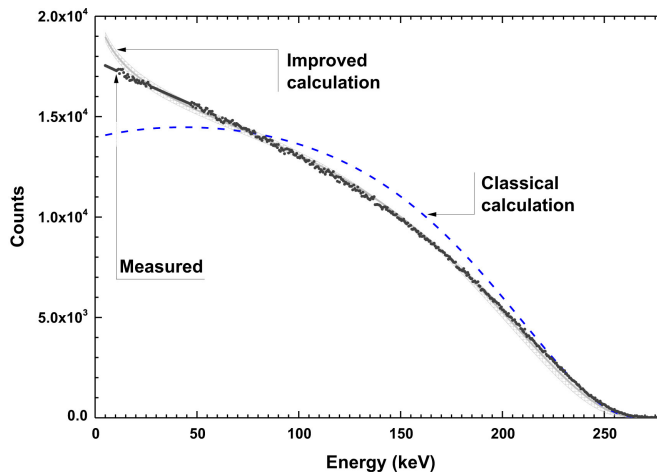


Figure 2.7: Comparison of β -decay continuum spectra of ^{138}La experiment and theory from [22]. The blue dotted line is the classical theoretical calculation and the black solid line is the experimental spectrum, found using the coincidence method. The gray band is the new theoretical calculation. The thickness of the gray band shows the uncertainty in the theory caused by the uncertainty in the endpoint energy (Q -value).

bound orbital is released. It is impossible to distinguish in an experiment whether the decay includes an electron exchange. In 2014, Mougeot and Bisch defined corrections to help account for the screening and exchange effects in β -decay when trying to calculate theoretical continuum spectra [24]. In Fig. 2.8, the effects of these two corrections on the low-energy region of a theoretical spectrum (that of ^{241}Pu decay) can be seen.

In order to meaningfully compare the theoretical and experimental spectra, the scintillator used in the experiment must be tested for systematic errors. An independent measurement of the endpoint energy — the Q -value — of the decay using an established method would simultaneously test the systematics of the new scintillator and lower the uncertainty of the theoretical spectrum caused by the uncertainty in the endpoint energy. As discussed in the introduction, Penning trap mass spectrometry is currently the most precise method of measuring nuclear masses and Q -values. The LEBIT Penning trap at the NSCL was used to measure the ^{138}La β -decay Q -value. This measurement and its results are described in

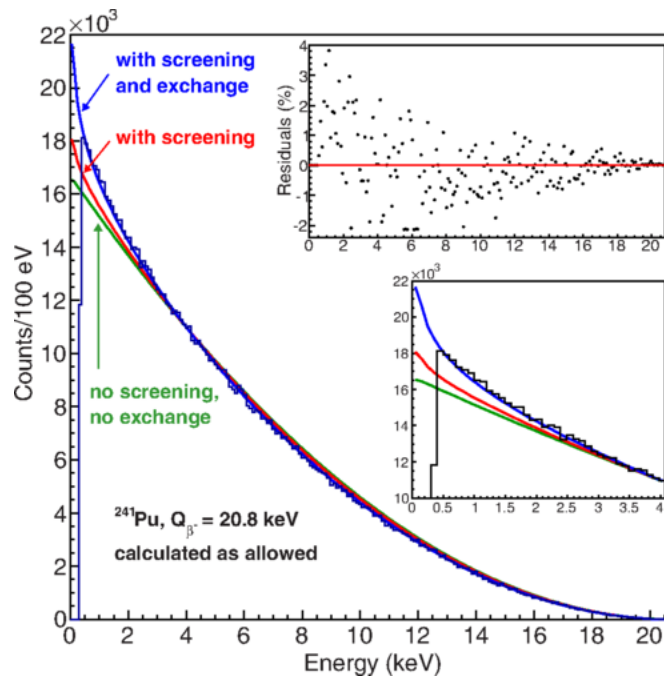


Figure 2.8: Fitting a theoretical spectrum to the experimental data of ^{241}Pu β -decay, from [24]. The green curve is the classical calculation, the red curve includes the screening correction, and the blue curve includes both the screening correction and the exchange correction.

the following chapter.

Chapter 3

The LEBIT Facility

This three-eights is too small. I need a larger three-eights.

-Martin Eibach

The Low Energy Beam and Ion Trap (LEBIT) facility, a schematic of which can be seen in Fig. 3.1, is located at the National Superconducting Cyclotron Laboratory (NSCL). The NSCL is an NSF-funded national laboratory known for producing rare isotope beams by way of projectile fragmentation. The NSCL houses the Coupled Cyclotron Facility (CCF), a series of two superconducting cyclotrons which can produce beams with energies on the order of 100 MeV per nucleon. The LEBIT facility is found in the so-called “low-energy” area of the NSCL. Rare isotopes produced by the CCF are thermalized in a helium-filled gas cell, extracted using DC potential gradients and RF electrodes, then sent to LEBIT and other facilities to perform low energy precision measurements.

3.1 Offline Sources at LEBIT

In addition to being connected to the CCF to receive rare isotope beams, LEBIT houses two offline sources, a Laser Ablation Source (LAS) and a Test Ion Source (TIS), both of which can be seen in Fig. 3.1. These sources can be used to generate beams of stable and long-lived isotopes, including those with low natural abundance. While these sources are

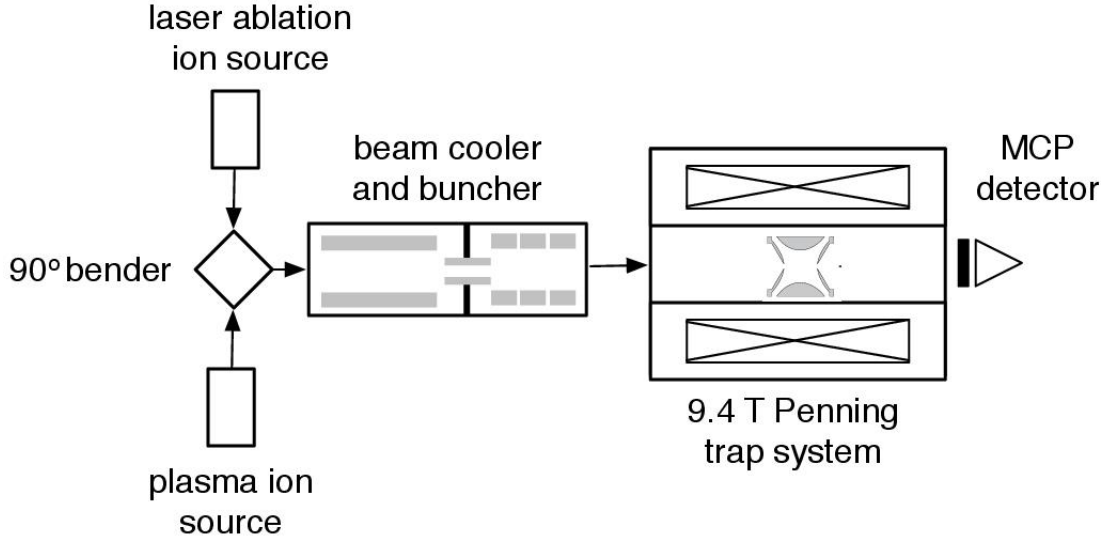


Figure 3.1: A schematic of the relevant section of the LEBIT (Low Energy Beam Ion Trap) facility at the NSCL.

primarily utilized for production of reference nuclei during rare isotope measurements, they also are used to perform measurements of stable and long-lived isotopes that are scientifically interesting in their own right; see, for example, Refs. [25–28].

3.1.1 The Laser Ablation Source

The Laser Ablation Source (LAS) consists of a pulsed, frequency-doubled Nd:YAG Quantum Brilliant laser to output 532 nm light [29]. The 160mJ, 4 ns light pulses, which repeat at a rate of 20 Hz, are focused through a series of prisms and lenses to impinge upon a solid target (see Fig. 3.2). The laser evaporates material from the surface of the target and the evaporated material is ionized by the high temperature of the laser. These ions are then accelerated out of the LAS via a series of extraction electrodes and steered into the cooler-buncher, as shown in Fig. 3.1.

The targets utilized with the LAS, which can be seen in Fig. 3.3, are usually ~ 1 mm thick

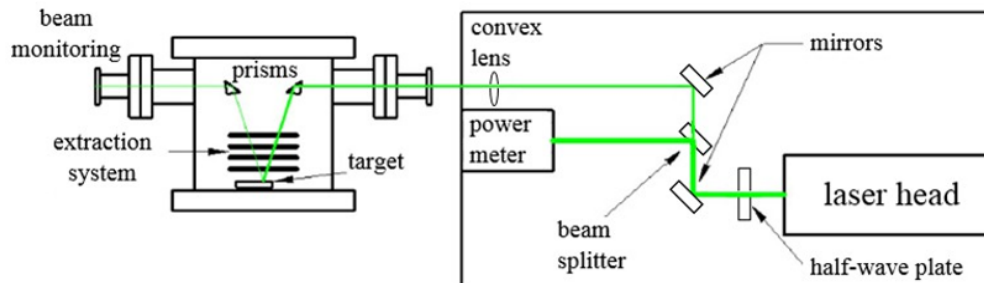


Figure 3.2: A schematic of the Laser Ablation Source.

and are mounted on a target holder which is controlled by a computerized stepper motor. The stepper motor rotates the target holder through an arc of 170° to prevent drilling effects by the laser. Often, targets of two different materials will be mounted on either side of the target holder. The stepper motor can then be used to selectively switch back and forth between the two materials, allowing for consecutive measurements of multiple elements. The targets used in this work are of natural abundance of the element of interest, meaning that all naturally occurring isotopes of the element will be found within the target, as well as contaminants and impurities that may be present in the material.

3.1.2 The Plasma Ion Source

The Plasma Ion Source, also called the Test Ion Source and abbreviated to TIS, is a modified commercial ion source from the Coultron Research Corporation. It consists of an alumina chamber which houses a tungsten filament and an anode plate secured by a cap a few millimeters above the filament. This chamber can be filled with a noble gas via a needle valve to create a plasma. The tungsten filament is heated to produce electrons and is negatively biased. For gas pressures around 10^{-6} mbar, this causes a continuous discharge, ionizing the gas within the chamber and creating a plasma. This method is most commonly

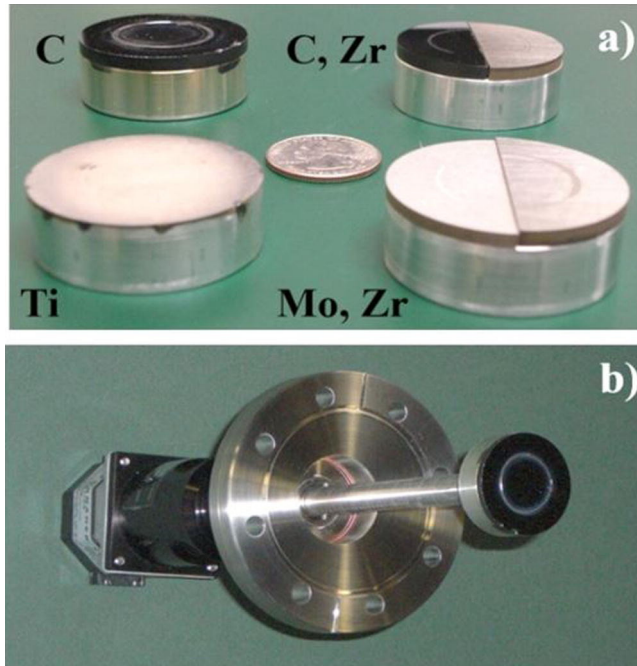


Figure 3.3: The targets used with the LAS, taken from [29]. Picture (a) shows a variety of targets. Clockwise from the top left is a single carbon target, a dual carbon-zirconium target, a dual molybdenum-zirconium target, and a single titanium target. Picture (b) shows the single carbon target mounted on the target holder, which is controlled by a stepper-motor. Also visible is the path the laser takes along the target, seen here as a circular groove.

used to create ions from noble gas which is leaked into the source, but it can also be used to produce ions from other gases or from solid materials with low melting points. A small, powdered amount of such a material is placed within a ceramic charge holder and inserted into the center of the filament in the chamber. Heating by the hot filament causes the material to vaporize. The vaporized material is ionized in the plasma discharge and can be extracted.

Alternatively, the source can be positively biased and operated with no helium support gas. The impure filament then produces trace amounts of the alkali metals via surface ionization when heated and the positive bias accelerates the ions away from the filament. Alkali earth metals can also be created by inserting a small amount of powdered metal into

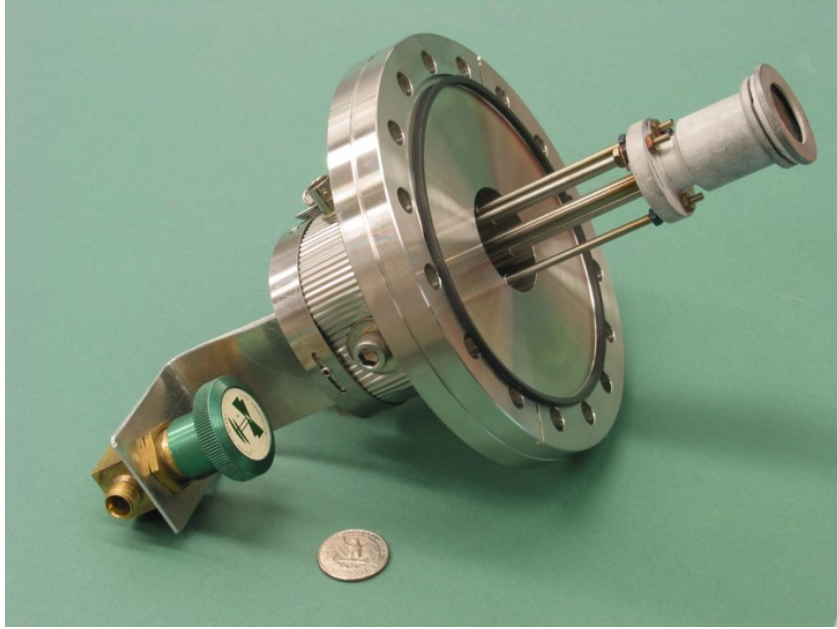


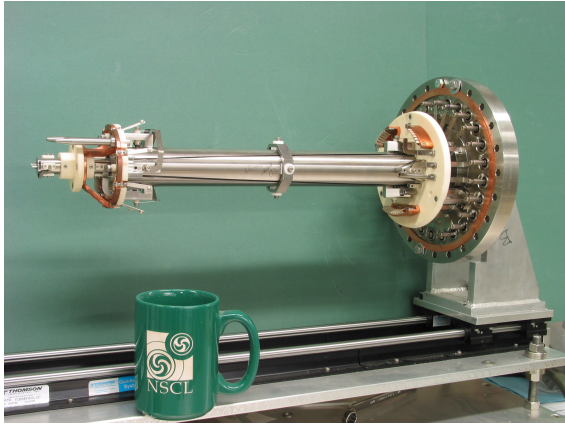
Figure 3.4: A picture of the Thermal Ion Source chamber, with a USD 25 cent piece for scale. Shown here is an older chamber, composed of boron nitride, while the newer chamber is made of alumina. At the end of the chamber, the anode plate is visible through the endcap.

the charge holder, as described above. Ions of the alkali earth metal are then produced via surface ionization as the filament is heated. For both of these surface ionization methods, the technique is limited to elements with ionization energies of less than ~ 7 eV [30, 31].

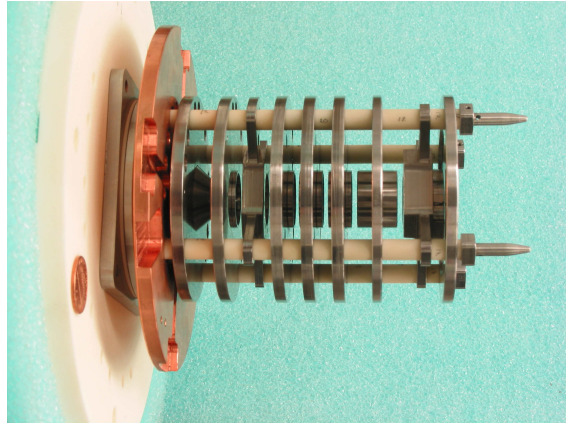
For all of these methods, the ions are extracted through a series of electrodes and steered into the cooler-buncher. As with the LAS, all of the stable and long-lived isotopes of the various available elements are created in ratios similar to the natural abundance of each isotope.

3.2 The Beam Cooler-Buncher

After extraction from the sources, the ions are decelerated to only a few tens of eV of total energy and are steered into the beam cooler-buncher for final preparation before



(a) The pre-cooler and micro-RFQ.



(b) The buncher.

Figure 3.5: Photos of the LEBIT beam cooler-buncher, used to prepare beam for delivery to the Penning trap, shown here in two parts. On the left are the pre-cooler and the micro-RFQ, shown with an NSCL coffee mug for scale. On the right is the buncher.

delivering to the Penning trap [32]. The cooler-buncher is separated into three parts: the pre-cooler, the micro-RFQ, and the buncher. The entire apparatus can be cooled to liquid nitrogen temperatures and is filled with a helium buffer gas in the pre-cooler. A heavier gas, such as neon, can also be added to the buffer gas to instigate collision-induced break-up of molecules, improving beam purity [33]. All three sections utilize four rod electrodes to create a radio frequency quadrupole (RFQ) field and confine the ions radially. Outside of the four rod electrodes are wedge electrodes. The wedges are held at static potentials and create a varying axial electric field to drag the ions through the buffer gas.

The pre-cooler section has the highest concentration of buffer gas, usually around 0.03 mbar. This, combined with an axial DC electric field, quickly cools the ions and reduces the transverse emittance of the beam. Next is the micro-RFQ, which creates a barrier between the pre-cooler and the buncher. This allows for differential pumping of the two sections, as the buncher must be held at a pressure that is more than an order of magnitude lower than that of the pre-cooler to prevent re-heating of the ions during extraction. Mechanically, the

micro-RFQ is the same as the pre-cooler, but it is physically much smaller in size. Finally, the buncher consists of seven disk-shaped electrodes around four RFQ rods. By altering the DC voltages on each of the disk electrodes to form a well, the ions can be trapped. The continuous beam is collected in the buncher for a set amount of time (this time varies based on the experimental needs) and the bunch is held for final cooling for ~ 30 ms. The electrode potentials are then changed to extract the bunch in a low-emittance, sub-microsecond pulse. This low-emittance, bunched beam is required in order to capture within the Penning trap with a low energy spread.

The cooler-buncher improves the overall efficiency of the setup by reducing the number of ions sent to the Penning trap while the trap is closed. It can also be used for rudimentary beam purification. All ions in the bunch are extracted with the same kinetic energy per unit charge, $E = qV = \frac{1}{2}mv^2$. As such, higher mass ions move more slowly and lighter mass ions move more quickly, covering the same distance from the buncher to the Penning trap in different amounts of time. Just before the fringe field of the magnet is a fast electrostatic kicker, held at a high potential to prevent ions from continuing along the beamline. By lowering the potential of the kicker for a short time before switching back to high potential, tuned to the time of flight of the ions of interest, ions and molecules with shorter or longer times of flight are prevented from reaching the trap. The kicker has a resolving power of approximately $\frac{m}{\Delta m} > 400$. This is sufficient to clean most non-isobaric contaminants from the beam, which is important for targets of natural abundance.



Figure 3.6: The LEBIT Penning trap, shown here with one endcap removed and a bottle cap for scale.

3.3 The Penning Trap and Magnet

The LEBIT facility uses a hyperbolic Penning trap, seen in Fig. 3.6. Before and after the trap, within the magnet bore, are a series of drift tubes to assist with injection and ejection. One of the final injection drift tubes is four-fold segmented to create a so-called “Lorentz steerer” [34]. This Lorentz steerer gives increased control over the initial magnetron amplitude and phase of the ions during injection into the trap.

The LEBIT Penning trap is comprised of a hyperbolic ring electrode, two hyperbolic endcap electrodes, and two correction ring and correction tube electrodes. These final two sets of electrodes help to compensate for the fact that the E-field produced by the ring and endcap electrodes is not an ideal quadrupole field. This is due to the holes in the endcap electrodes, which allow for injection and ejection of the ions, and the finite extent of the trap electrodes, as well as potential machining and alignment imperfections [6]. The ring electrode is segmented into eight pieces, which are then paired into segments, so that dipole and quadrupole radio frequency (RF) fields can be applied to address the radial modes of the ions’ motion. The eight-fold segmentation could theoretically allow for octopole excitations,

as well [35]. The trap sits within a 9.4T magnet, which confines the ions radially via their cyclotron motion. Without the addition of the quadrupolar electrostatic field of the Penning trap itself, the ions would have a cyclotron frequency

$$f_c = \frac{qB}{2\pi m}, \quad (3.1)$$

where f_c is the cyclotron frequency, B is the magnetic field, and m/q is the mass-to-charge ratio of the ion. The trap electrodes produce a quadratic electrostatic field which confines the ions axially. The electric field also has the effect of reducing the frequency of the cyclotron motion of the trapped ions and introducing an additional radial motion, known as the magnetron motion [36].

Hence, ions in a Penning trap undergo three normal modes of motion: axial motion, reduced cyclotron motion, and magnetron motion, which can be seen in Fig. 3.7. These three normal modes are described by their eigenfrequencies, f_z , f_+ , and f_- respectively. The frequencies of the reduced cyclotron motion and the magnetron motion are particularly important for the measurement technique used at LEBIT, as they are related to the true cyclotron frequency of Eqn. 3.1 via the equation [37]:

$$f_c = f_+ + f_-. \quad (3.2)$$

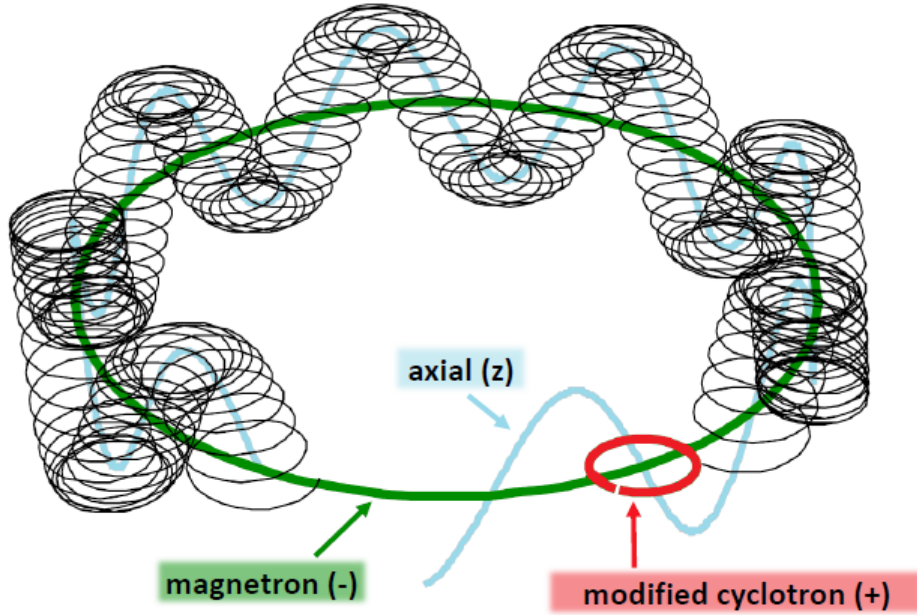


Figure 3.7: The superposition of an ion's three normal modes of motion within the Penning trap. The frequencies of the reduced cyclotron motion and the magnetron motion add to the true cyclotron frequency of the trapped ions.

3.4 Time of Flight-Ion Cyclotron Resonance

3.4.1 Mechanism

While there are several ways to use a Penning trap to measure the cyclotron frequency of an ion, the LEBIT facility specifically uses a technique known as Time of Flight-Ion Cyclotron Resonance, or TOF-ICR. This method was first demonstrated in 1980 when measuring the proton-electron mass ratio in Mainz [38]. The first on-line measurement came in 1990 by Becker, *et al.* at ISOLDE at CERN [35]. In this method, ions are typically injected into the trap along the center axis, then driven at their magnetron frequency to an initial radius. At LEBIT, the Lorentz steerers provide a large amount of control over how the ions are injected, and allow for off-center injection, typically ~ 0.5 mm away from the center of the trap, enabling the ions to be captured with an initial magnetron orbit. The hyperbolic

ring electrodes are then used to apply a quadrupolar radiofrequency (RF) pulse to the ions at a frequency near to the expected true cyclotron frequency, $f_{RF} \approx f_c = f_+ + f_-$. This pulse couples the reduced cyclotron and magnetron modes, which converts the initial magnetron motion into reduced cyclotron motion and increases the radial energy of the ions, $E = \frac{1}{2}m\omega^2r^2$. This conversion can be seen in Fig. 3.8. The ions are then released from the trap in the direction of a microchannel plate (MCP) detector, which is mounted just outside the magnetic field in a Daly configuration [39]. In the Daly configuration, ions are steered into a collecting plate, which creates a cascade of electrons that are detected by the MCP. This configuration improves the efficiency compared to detecting the ions directly with the MCP. The time of flight of the ions from the trap to the detector is measured and recorded. A new bunch of ions is then injected into the trap. The ions are driven with an RF pulse at a slightly different frequency before being released from the trap. This is continued with many ions for a range of frequencies around the expected true cyclotron frequency.

As the ions exit the magnet, they pass through a magnetic field gradient. The ions will experience a force due to this changing magnetic field which is related to their radial energy,

$$F_z = -\frac{E_r}{B_0} \left(\frac{\partial B}{\partial z} \right), \quad (3.3)$$

where F_z is the experienced force, E_r is the radial energy, B_0 is the strength of the magnetic field at the trapping location, and $\partial B/\partial z$ is the change in the magnetic field as the ions approach the MCP.

This force is maximized when the radial energy is maximized, which occurs when the magnetron motion is fully converted into reduced cyclotron motion. This, in turn, occurs

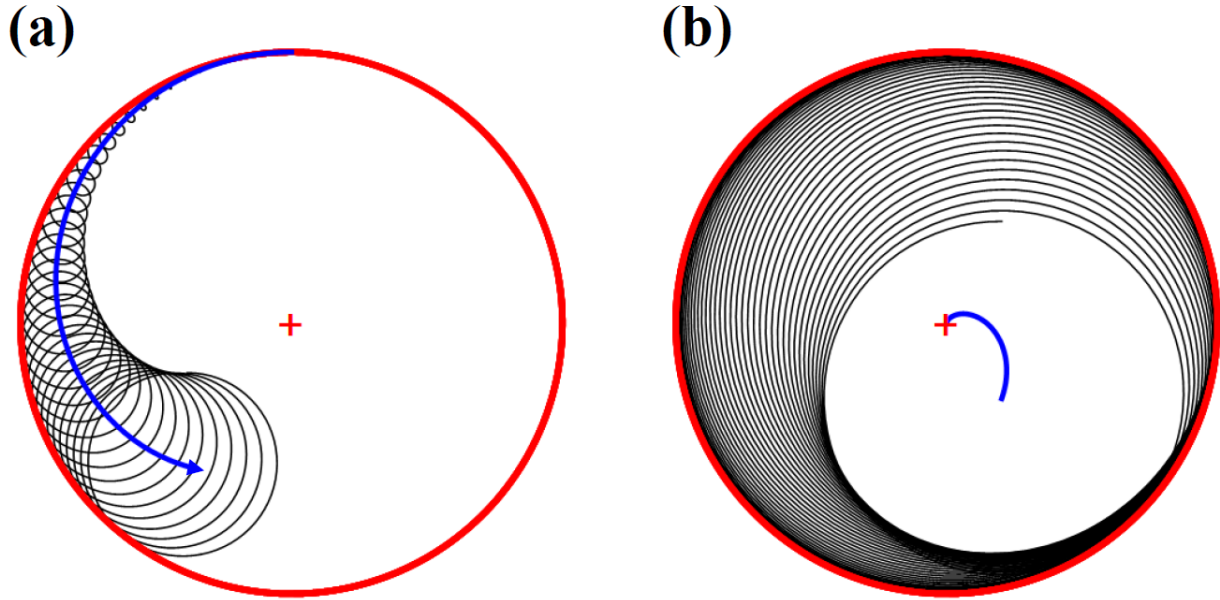


Figure 3.8: A diagram showing the conversion between magnetron and cyclotron motion in a Penning trap. The ion initially begins with pure magnetron motion, shown in red. The quadrupolar RF pulse drives the reduced cyclotron motion and increases its radius while decreasing the magnetron radius, as seen with the growing black circles in part (a). When the applied RF pulse matches the cyclotron frequency of the trapped ion, the magnetron motion is fully converted and the radius of the reduced cyclotron motion matches that of the initial magnetron motion, as seen with the growing black circles in part (b).

when the applied RF pulse is equal to the true cyclotron frequency of the trapped ions. Therefore, f_c is found by measuring the time of flight of the ions between the trap and the MCP detector; the time of flight is minimized when the force is maximized, or when the RF pulse is equal to the true cyclotron frequency of the trapped ions. This can be clearly seen in a so-called “resonance curve,” built with the time of flight measurements of ions driven at a range of frequencies, as seen in Fig. 3.9. The data points are fit with a theoretical lineshape, as described in [40], and the center of the theoretical curve is taken to be the cyclotron frequency of the trapped ions. For the remainder of the TOF-ICR discussion, the term “measurement” will refer to a complete resonance curve of a single ion species.

The width of this curve is proportional to $1/t_{RF}$, where t_{RF} is the duration of the

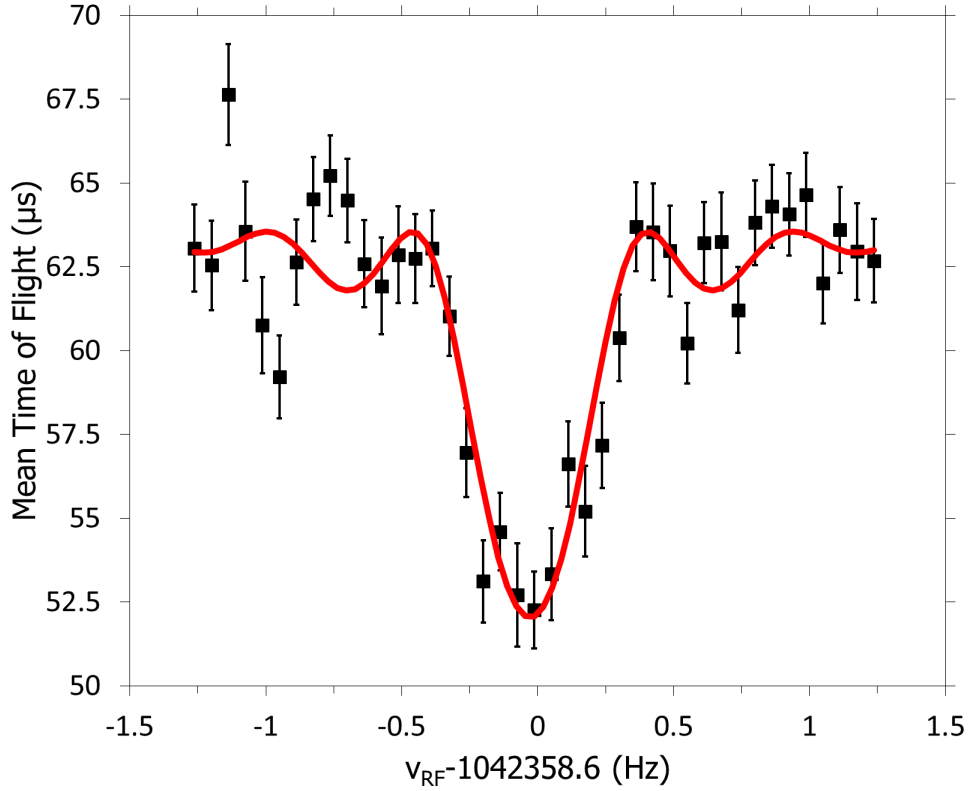


Figure 3.9: An example of a time of flight-ion cyclotron resonance curve, shown here with ^{138}La . The applied RF quadrupole excitation pulse is scanned over a range of frequencies, which includes the true cyclotron frequency of the trapped ions. The data are then fit with a theoretical curve, shown here as a red line, the minimum of which is the cyclotron frequency.

excitation pulse. Thus, ions are driven within the trap for as long as possible without half-life or charge exchange effects taking place to achieve the highest possible precision with each measurement.

3.4.1.1 Cleaning of Contaminant Ions

As mentioned in Section 3.2, the combination of the electrostatic kicker and beam cooler-buncher allow for rough cleaning of non-isobaric contaminants. However, contaminants within the trap can be cleaned more selectively, as well. The LEBIT Penning trap is con-

nected to five additional frequency generators. After contaminant ions and molecules within the trap are identified, the additional frequency generators pulse the ring electrode with a dipole RF pulse at the reduced cyclotron frequency of the identified contaminants. By exciting the reduced cyclotron motion of the unwanted species, the contaminant ions' cyclotron radius is increased until the ions are driven into the sides of the trap or until their radius is large enough that they will no longer exit the Penning trap through the endcap holes and will not perturb the measurement.

When the composition of contamination is not known, it can be identified by setting the main frequency generator to pulse the ring electrode in a dipole excitation scheme. The frequency is then scanned over a range of possible reduced cyclotron frequencies, similar to how the true cyclotron frequency measurement using a quadrupole pulse is performed. The number of ions extracted from the trap are counted for each frequency. When the number of ions is dramatically reduced, the reduced cyclotron motion of the contamination is being excited.

The dipole pulses used for cleaning are generally kept to a short (~ 25 ms) duration and have a high (~ 4 V) amplitude. This broad, strong excitation helps to better drive out contamination even when the exact reduced cyclotron frequency is unknown.

3.4.2 Magnetic Field Calibration

The LEBIT magnet, which can be seen in Fig. 3.10, is a superconducting, solenoidal magnet with a maximum magnetic field strength at the center of about 9.4 Tesla. It is known that the LEBIT magnetic field decays at a rate of approximately 10 ppb/hour. The



Figure 3.10: The LEBIT magnet, a 9.4 Tesla superconducting solenoid.

magnetic field is kept relatively stable with the use of a compensating power supply, which slowly increases the voltage in a secondary wire coil around the magnetic bore to keep the magnetic field at the Penning trap as constant as possible. However, non-linear drifts can still occur. Therefore, it is necessary to take calibration points before and after each measurement of the ion of interest, to know the precise strength of the magnetic field.

Before and after each measurement of the ion of interest, a measurement is taken of a well-known reference ion with a similar mass-to-charge ratio, i.e. mass m_{ref} is measured at times t_1 and t_3 , while mass m_{int} is measured at time t_2 . The two reference measurements are then linearly interpolated to find the frequency of mass m_{ref} at the time t_2 , as shown in Fig. 3.11. From there, the frequency ratio of the reference ion and the ion of interest can be calculated, via the equation

$$R = \frac{f_{cint}(t_2)}{f_{cref}(t_2)} = \frac{m_{ref}}{m_{int}}. \quad (3.4)$$

Typically, many measurements are taken of the ion of interest, each bracketed by mea-

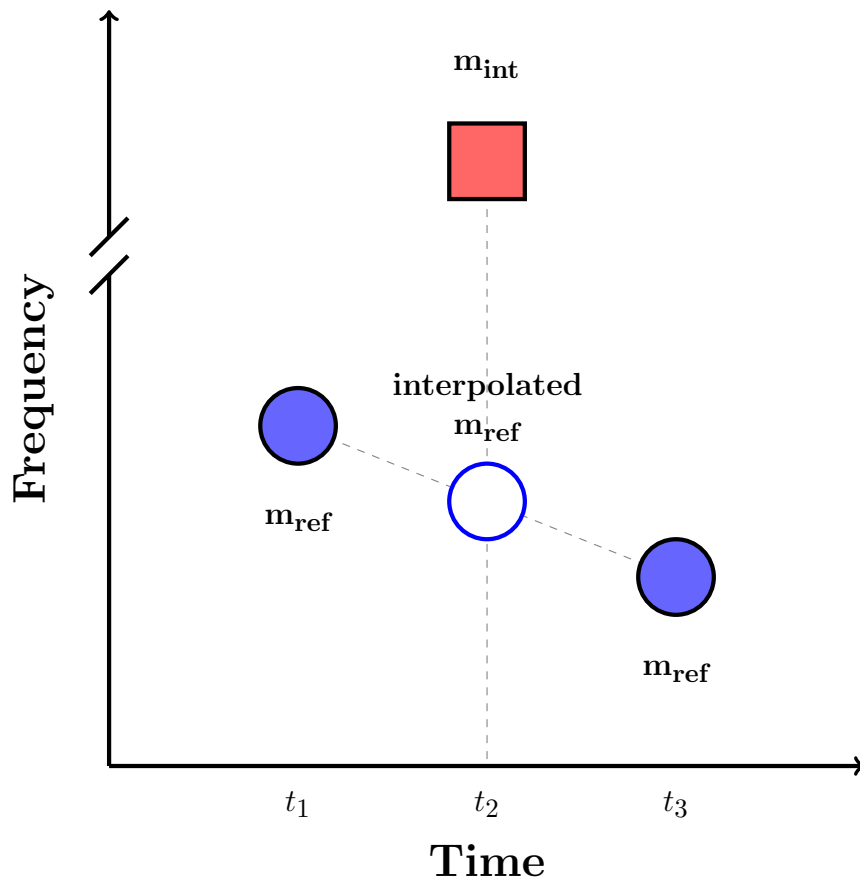


Figure 3.11: An illustration explaining how reference measurements are used to calibrate LEBIT's magnetic field. An ion of well-known mass is measured before and after each measurement of the ion of interest. The two points of the reference ion measurements are then linearly interpolated to find the cyclotron frequency of the reference at the time the measurement of the ion of interest is taken.

measurements of a reference ion. For each measurement, a frequency ratio is calculated for the reference ion compared to the ion of interest, and these many frequency ratios are averaged to find a value \bar{R} . This average frequency ratio can be used to find the mass and Q -value of the ion of interest, as explained in the next section.

This method of interpolation compensates for linear shifts in the magnetic field throughout the course of the experiment. While non-linear B-field fluctuations do occur, such as fluctuations due to atmospheric pressure circulations, it has been found that they produce systematic uncertainties in individual frequency ratios on the order of 10^{-10} , which is negligible compared to the uncertainties of individual resonances, usually around 10^{-8} [41].

3.4.3 Data Analysis

Penning trap mass spectrometry is a powerful tool for finding the mass of an atom. Given Eqn. 3.4 and the knowledge that the frequency ratio is equivalent to the ratio of the ion masses, it is possible to find the mass of the atom of interest via the equation:

$$M_{int} = (M_{ref} - m_e) \frac{1}{\bar{R}} + m_e, \quad (3.5)$$

where M_{int} is the mass of the ion of interest, M_{ref} is the mass of the reference ion, and m_e is the mass of the electron. The electron binding energy is generally smaller than the uncertainty of the measurements, and can be ignored.

Once the absolute masses of the parent and daughter atoms have been calculated, it is possible to find the Q -value of the decay using Eqn. 1.5, as described in the Introduction.

3.4.3.1 Direct Measurements

At the LEBIT facility, there are two methods used for determining the Q -value. The first, called the “direct” method, is when the reference ion is the daughter nuclide of the ion of interest. Alternating measurements are taken of the daughter and parent. In this case, the frequency ratio of the parent and daughter is measured “directly” and \bar{R} is used to directly calculate the Q -value. By dividing out the mass of the daughter atom, Eqn. 1.5 can be rewritten for direct measurements as

$$Q = (M_p - M_d)c^2 = (M_d - m_e)\left(\frac{1}{\bar{R}} - 1\right)c^2, \quad (3.6)$$

where in this case \bar{R} is specifically the average cyclotron frequency ratio of singly-charged ions of the parent and daughter nuclides.

Direct measurements are the preferred method of mass measurement whenever they are possible. These “mass doublets” eliminate potential mass-dependent systematic shifts. They also lead to more precise measurements. The uncertainty propagation for Eqn. 3.6 is

$$\sigma_Q = \sqrt{\left(\frac{1}{\bar{R}} - 1\right)^2 \sigma_{M_d}^2 + (M_d - m_e)^2 \sigma_{\bar{R}}^2}. \quad (3.7)$$

This means the uncertainty in the mass of the daughter only contributes to the overall uncertainty when multiplied by $\frac{1}{\bar{R}} - 1$. For a mass doublet, $\bar{R} - 1$ is typically $10^{-9} - 10^{-10}$. Compared to the contribution of the uncertainty of \bar{R} itself, the contribution of the uncertainty in the mass of the daughter is negligible. The uncertainty in Q , then, is

$$\sigma_Q = (M_d - m_e)\sigma_{\bar{R}}, \quad (3.8)$$

the same as the uncertainty for M_{int} from Eqn. 3.5. For comparison, the uncertainty propagation for Eqn. 1.5 is

$$\sigma_Q = \sqrt{\sigma_{M_p}^2 + \sigma_{M_d}^2}, \quad (3.9)$$

where the uncertainties in the absolute masses of the parent and daughter nuclei add in quadrature, leading to an error of a factor of $\sqrt{2}$ larger.

3.4.3.2 Indirect Measurements

The second method of measurement used at LEBIT, called the “indirect” method, is when the reference ion is an unrelated, well-known stable ion or molecule. In this case, the frequency ratio measured is the ratio between the ion of interest and the well-known ion. If the parent and daughter are measured separately against the same reference ion, it is possible to take a “ratio of ratios,” where $R = \frac{M_d}{M_{ref}} \frac{M_{ref}}{M_p} = \frac{M_d}{M_p}$. If the parent and daughter are not both measured, the ratio of the ion of interest and the reference ion must be used to find the absolute mass of the ion of interest, which can then be used with the Atomic Mass Evaluation and Eqn. 1.5 to find the Q -value. Often, both of these methods are used to measure a Q -value. This allows for checks of consistency.

For indirect measurements, it is preferred to use a reference ion with a mass-to-charge ratio as close as possible to that of the ion of interest. This helps to prevent possible mass-dependent shifts. However, these mass-dependent shifts are regularly checked at LEBIT and are found to cause shifts in the frequency ratio on the order of 2×10^{-10} per mass unit difference between the reference and the ion of interest [25]. For most measurements at LEBIT, this level of uncertainty is negligible compared to the statistical uncertainty and can thus be ignored.

3.4.3.3 The Birge Ratio

Once the cyclotron frequency ratios have been calculated and the average found, the Birge Ratio of the data is determined. The Birge Ratio, initially defined by Raymond Birge in 1932, is a method of quantifying the scatter of a data set, σ_e compared to the error bars on the individual points, σ_i [42]. If fluctuations of the data are within what is expected for Gaussian statistics, the ratio σ_e/σ_i should be close to unity. If the ratio is much greater than one, the fluctuations within the data cannot be accounted for by statistics and show that the statistical uncertainties, σ_i of the individual measurements could be underestimated or that there are potentially systematic errors which have not been accounted for.

When the Birge ratio is greater than one, the statistical uncertainty of \bar{R} is inflated by multiplication with the Birge Ratio. As measurements at LEBIT are expected to all have equal reliability, and thus the uncertainties are all underrated by the same factor, this Birge adjustment is valid. For more information on how LEBIT calculates the Birge Ratio, see [33].

Chapter 4

Measurement of ^{138}La β - and ϵ -Decay

Q -values

Ninety percent of my time in this lab is spent looking for the tool I was using thirty seconds ago.

-Rachel Sandler

The measurement of the ^{138}La β -decay and ϵ -decay Q -values were performed at the LEBIT facility at the NSCL (see Chapter 3 for a full description of the facility). The experiment was run in two stages: a “direct measurement” stage and an “indirect measurement” stage. For both stages, isotopes of ^{138}La , ^{138}Ce , and ^{138}Ba were created via the Laser Ablation Source (LAS), discussed in Sec. 3.1. The LAS was fitted with pairs of sheets of naturally abundant lanthanum, barium, and cerium that were approximately $25\text{ mm} \times 12.5\text{ mm} \times 1\text{ mm}$ thick. For the indirect measurement stage, the Test Ion Source (TIS) was fitted with a canister of naturally abundant xenon gas to produce ^{136}Xe . The natural abundances of these isotopes, as well as ^{136}Ba and ^{134}Xe used for systematic checks, can be seen in Table 4.1 [43].

The results presented in this chapter were recently published in Physical Review C [44]. Portions of the text in this chapter and several of the figures presented here are reproduced from this reference. Additional details and discussion are included here, as well.

Table 4.1: The natural abundances of the isotopes used in this experiment.

Ion	Mass Number	Abundance (%)
La	138	0.089
	139	99.911
Ce	138	0.251
Ba	136	7.854
	138	71.698
Xe	134	10.436
	136	8.857

4.1 Direct Measurement of the ^{138}La β -Decay Q -value

The LAS was initially fit with targets of lanthanum and cerium. The cyclotron frequencies of $^{138}\text{La}^+$ and $^{138}\text{Ce}^+$ were measured alternately using the time-of-flight ion cyclotron resonance (TOF-ICR) technique described in Sec. 3.4. Each $^{138}\text{La}^+$ measurement was bracketed by two $^{138}\text{Ce}^+$ measurements, which were interpolated to find the cyclotron frequency of cerium at the time of the lanthanum measurements. An example of a $^{138}\text{La}^+$ resonance can be seen in Fig. 3.9. The ions within the trap were driven with an RF pulse of two seconds and approximately thirty measurements of each isotope were taken, leading to thirty measurements of $R = f_c(^{138}\text{La}^+)/f_c(^{138}\text{Ce}^+)$. These were combined into a single average value of \bar{R} , which was then used with Eqn. 3.6 to find the β -decay Q -value for ^{138}La . These individual ratio measurements, as well as \bar{R} , can be seen in Fig. 4.1.

The overall process was repeated a second time, replacing the cerium target in the LAS with a target of barium to measure the ratio $R = f_c(^{138}\text{La}^+)/f_c(^{138}\text{Ba}^+)$ so that the ^{138}La ϵ -decay Q -value could be measured. This time, nearly fifty measurements of each ion were taken and used to find \bar{R} . Finally, the lanthanum target in the LAS was replaced with the previously-used cerium target to enable measurement of $R = f_c(^{138}\text{Ce}^+)/f_c(^{138}\text{Ba}^+)$ and

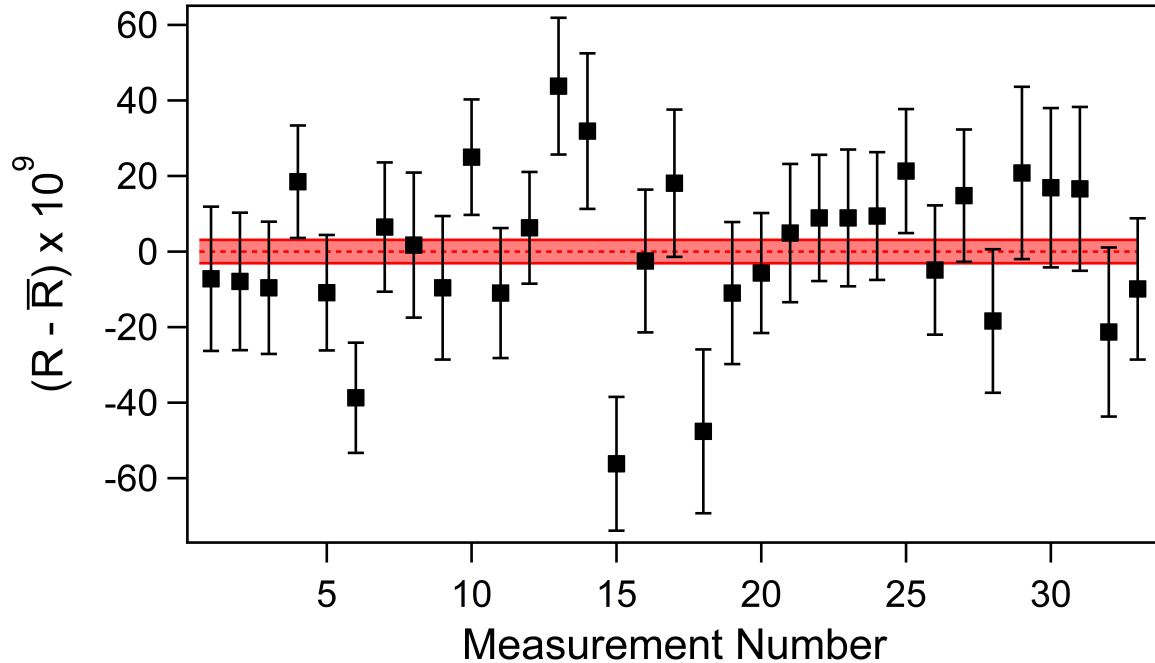


Figure 4.1: Cyclotron frequency ratio measurements for $^{138}\text{La}^+ / ^{138}\text{Ce}^+$, with the 1σ uncertainty in \bar{R} shown by the shaded region.

allow for the ^{138}Ce 2ϵ -decay Q -value to be measured. This measurement was desired to act as a check of systematics for the other two measurements, as the energy difference between the ^{138}La ϵ -decay and the ^{138}La β -decay Q -values should be equal to the ^{138}Ce 2ϵ Q -value (see Fig. 2.5). At this point, it was noticed that the large abundance of ^{138}Ba compared to the much smaller abundances of ^{138}La and ^{138}Ce was causing increased difficulty. While the LAS uses a stepper motor (described in Sec. 3.1) to selectively change between two targets on a target holder, it was found that ^{138}Ba was produced regardless of which target was selected. It was believed this was caused by the vaporization of the barium target by the laser pulse, which then coated the inner chamber of the LAS. It was conjectured that reflected laser light was then able to ionize the barium coating, sending it to the Penning trap along with ions produced by ablation of the targets. Nevertheless, it was possible to take about thirty measurements of each isotope, with ^{138}Ba used as the bracketing reference

mass. The three ratio measurements can be found in Table 4.2.

Table 4.2: Measured frequency ratios, $f_c(\text{parent})/f_c(\text{daughter})$, of $^{138}\text{La}^+$, $^{138}\text{Ba}^+$, and $^{138}\text{Ce}^+$ against each other for direct Q -value measurements. The uncertainties provided for \bar{R} include inflation by the Birge Ratio where necessary (see Sec. 3.4.3.3).

Num.	Ion Pair	N	BR	\bar{R}
(1)	$^{138}\text{La}^+ / ^{138}\text{Ce}^+$	33	1.2	0.999 991 810 7(37)
(2)	$^{138}\text{La}^+ / ^{138}\text{Ba}^+$	48	1.1	0.999 986 387 2(29)
(3)	$^{138}\text{Ce}^+ / ^{138}\text{Ba}^+$	32	1.0	0.999 994 589 6(56)

From the ratios in Table 4.2, it is possible to find the Q -values for the three decays using Eqn. 3.6. It is also possible to find the absolute masses of ^{138}La and ^{138}Ce , using ^{138}Ba as a reference and Eqn. 3.5. The resulting masses are listed in Table 4.3. Previous to this work, the mass of ^{138}Ba was known via neutron capture measurements and linked to the ^{133}Cs mass standard via ^{133}Cs neutron-capture and ^{144}Cs β -decay Q -value. Thus, in the AME 2016 the uncertainty for the mass excess of ^{138}Ba is only 0.3 keV [1]. In the AME 2016, the mass of ^{138}Ce is determined almost entirely from the Quarati *et al.* β -decay endpoint energy measurement and the mass of ^{138}La . The mass of ^{138}La on the other hand is partially obtained from a $^{138}\text{La}(d,p)^{139}\text{La}$ reaction measurement, and a $^{139}\text{Ba} \rightarrow ^{139}\text{La}$ β -decay measurement that link it to the barium isotopes and ultimately ^{133}Cs and ^{136}Xe , as discussed above. It is also partially determined from a network of neutron capture, β -decay and α -decay measurements that link the lanthanides up to ^{163}Dy and ^{163}Ho for which precise Penning trap measurements have been performed [45]. The uncertainties for the mass excesses of ^{138}Ce and ^{138}La were 3 and 5 keV, respectively. As can be seen in Table 4.3, the mass values for ^{138}La and ^{138}Ce have been improved by a factor of 6 over the AME 2016. These mass values are given as “mass excesses,” or the difference between the atomic mass and the mass number in atomic mass units (in this case, 138 for all three isotopes in

Table 4.3: Absolute mass measurements of ^{138}La and ^{138}Ce , given as the mass excess, calculated using ^{138}Ba as a reference ion. The column DM is the amount the measured mass excess deviates from the AME 2016.

Nuclide	ME (keV/c ²)		DM (keV/c ²)
	This Work	AME 2016	
^{138}La	-86 513.44(0.57)	-86 519.2(3.2)	5.8(3.2)
^{138}Ce	-87 567.12(0.84)	-87 570.9(4.9)	4.7(4.9)

question), which is then converted to keV. This equation is given in the Introduction, but is repeated here for convenience:

$$ME = (M - m_u(A))C, \quad (4.1)$$

where M is the absolute mass of the atom in atomic mass units, m_u is 1 atomic mass unit, A is the mass number, and $C = 931494.0954$ is the conversion factor from atomic mass units to energy. For both isotopes, there was a clear shift away from the AME 2016, with both masses measured to be ~ 5 keV larger than the AME 2016 values. As the isotopes were connected in the AME 2016 by the ^{138}La β -decay Q -value, it is unsurprising that they both shifted in the same direction.

Using the frequency ratios and the calculated absolute masses, the Q -values of the decays were then found using two different methods, as listed in Table 4.4. “Direct” measurements were calculated using Eqn. 3.6 and measurements listed as “Masses” were calculated using Eqn. 1.5 and our absolute mass values. The column ΔQ is the difference between the average of these measurements and the AME 2016. The β -decay Q -value of ^{138}La to ^{138}Ce was improved over the AME 2016 by nearly a full order of magnitude. This result is compared to that of Quarati *et al.*, the AME 2016, and the AME 2012 in Fig. 4.2. It is important

Table 4.4: Q -values based on the direct measurement of f_{cd}/f_{cp} and absolute mass measurements, along with the 2016 AME value.

Decay	Met.	Q -value (keV)		ΔQ (keV)
		This Work	AME 2016	
^{138}La (β^-)	^{138}La - ^{138}Ce	1051.98(48)		
	Masses	1053.67(81)	1051.7(4.0)	0.7(4.0)
	Avg.	1052.42(41)		
^{138}La (ϵ)	^{138}La - ^{138}Ba	1748.67(37)		
	Masses	1746.98(86)	1742.5(3.2)	5.9(3.2)
	Avg.	1748.41(34)		
^{138}Ce (2ϵ)	^{138}Ce - ^{138}Ba	695.01(72)		
	Masses	695.68(1.58)	690.7(4.9)	5.3(4.9)
	Avg.	695.35(44)		

to note that the AME 2016 includes the Quarati measurement, which was the most precise measurement at the time. It can be seen that the Quarati measurement agrees strongly with the LEBIT value, suggesting that there were no uncorrected systematic errors in the LaBr_3 detector measurement and confirming the validity of this relatively new detector technology.

4.2 Indirect Measurement of the ^{138}La β -Decay Q -value

After completing the direct measurements in the previous section, additional absolute mass measurements were taken of ^{138}La , ^{138}Ce , and ^{138}Ba against the reference ^{136}Xe . This would allow for testing of LEBIT systematics and check the AME 2016 value of ^{138}Ba , which had never before been directly measured. The TIS was fit with a canister of naturally abundant xenon gas to produce ^{136}Xe ions, the closest stable isotope of xenon to the ions of interest, previously measured at FSU [46]. First ^{138}Ba was measured against ^{136}Xe . As the isotope with the highest natural abundance—and with the contamination problem mentioned

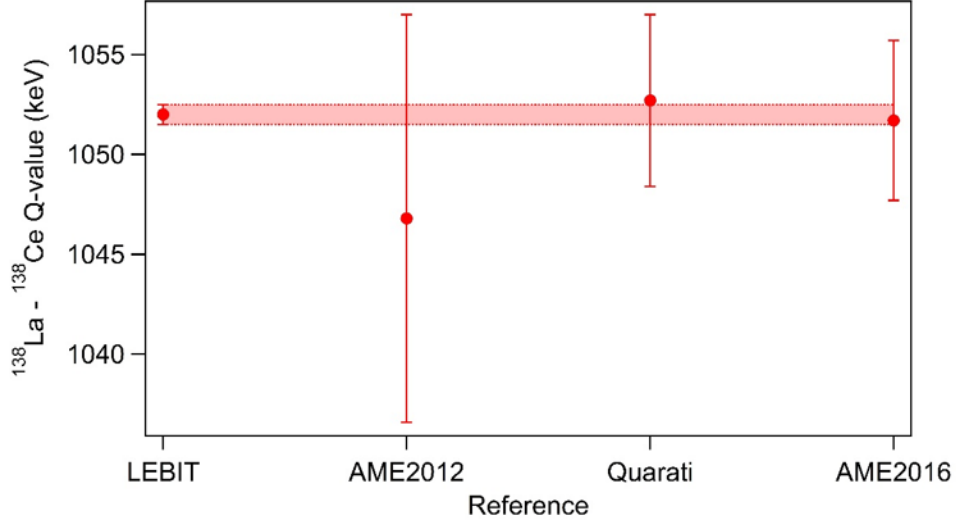


Figure 4.2: The LEBIT direct measurement of the β -decay Q -value of ^{138}La decaying to ^{138}Ce , compared to Quarati *et al.*, the AME 2016, and the AME 2012. It can be seen that there is strong agreement between the Quarati measurement and this measurement, though this measurement is nearly an order of magnitude more precise. It is also important to note that the AME 2016 value includes the Quarati measurement, which was the most precise value at the time.

in the previous section—it was hoped that the measurement would be straight-forward and the LAS could be scoured afterwards to remove the barium contamination. It was possible to successfully measure the mass of ^{138}Ba to a precision of 0.44 keV, which showed very good agreement with the AME 2016 value.

Next, the barium and cerium targets were removed from the LAS. The LAS chamber and the extraction electrodes were disassembled and the inner surfaces were scrubbed with methanol before reassembling. A fresh cerium target was placed on the target holder, this one approximately $25\text{ mm} \times 25\text{ mm} \times 1\text{ mm}$ thick, to cover the entire 360° that can be impinged upon by the laser. The target holder was replaced and the LAS used to produce ^{138}Ce isotopes. While the desired cerium isotopes were seen, unfortunately ^{138}Ba contamination was also still seen and came in a much greater proportion than ^{138}Ce . An example of the result of this contamination can be seen in Fig. 4.3. When both resonances were visible,

it was determined that approximately five times as much ^{138}Ba as ^{138}Ce was entering the trap. At times, it was not possible to see a resonance of ^{138}Ce at all, and it is likely that the fraction of ^{138}Ba was even higher. At 9.4 T, the cyclotron frequency of $^{138}\text{Ba}^+$ is only 8 Hz away from $^{138}\text{Ce}^+$, which makes it very difficult to clean by RF dipole excitation, as described in Sec. 3.4.1.1, without damaging the quality of the resonances. When a large amount of uncleaned contamination is in the trap, it dampens the signal of the ion of interest. This is because the contaminant ions have a much larger time of flight compared to the ions of interest at the expected cyclotron frequency. The disparate times of flight are averaged together, leading to less of a time of flight effect overall and a more shallow resonance. In Fig. 4.3, it can be seen that the $^{138}\text{Ce}^+$ resonance is much more shallow than the $^{138}\text{Ba}^+$ resonance, as the non-resonating $^{138}\text{Ba}^+$ contamination is overwhelming the resonating $^{138}\text{Ce}^+$ ions. Eventually the mass of ^{138}Ce was measured against ^{136}Xe , but only a precision of 1.54 keV was reached. This measurement did, however, have good agreement with the previous measurement of the mass of ^{138}Ce , taken against ^{138}Ba .

Finally, the LAS chamber was disassembled and the inner surfaces of the chamber and extraction electrodes were scrubbed a second time, replacing the cerium target on the target holder with a new lanthanum target, this one also 25 mm \times 25 mm \times 1 mm thick. The target holder was replaced and it was attempted to use the LAS to produce ^{138}La . Unfortunately, due to the very low natural abundance of ^{138}La (see Table 4.1), the background contamination from ^{138}Ba completely overwhelmed the ^{138}La signal and it was not possible to perform an absolute mass measurement against ^{136}Xe . The measurements that we did perform of $^{138}\text{Ba}^+$ and $^{138}\text{Ce}^+$ against $^{136}\text{Xe}^+$ to obtain mass values can be seen in Table 4.5

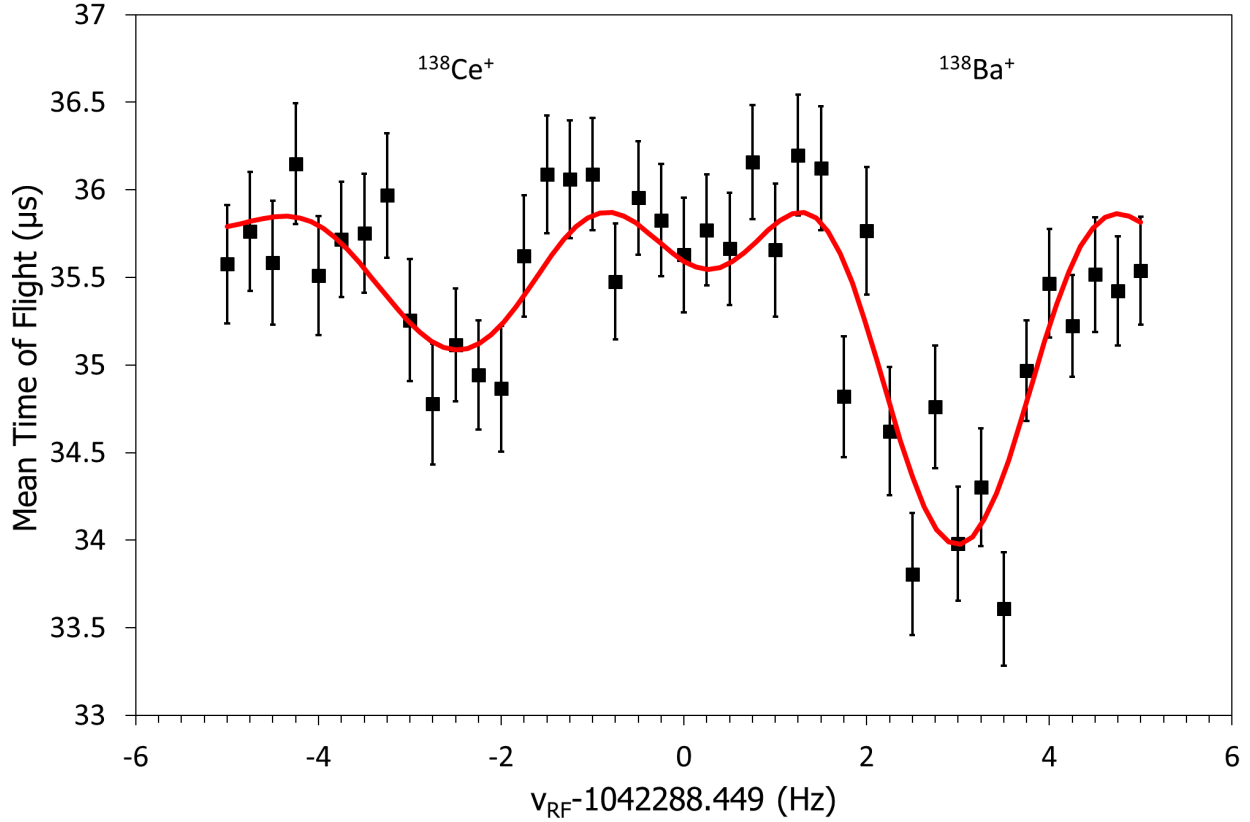


Figure 4.3: An example of a resonance of $^{138}\text{Ce}^+$ showing a significant amount of $^{138}\text{Ba}^+$ contamination. In this example, the ^{138}Ba (right) is coming at a rate of approximately five times the amount of ^{138}Ce (left).

along with the values from the AME 2016.

The mass excesses for ^{138}Ba , ^{138}La , and ^{138}Ce , calculated by taking weighted averages of the values in Tables 4.3 and 4.5, can be found in Table 4.6 and Fig. 4.4. The black data points with error bars are the LEBIT measurements minus the AME 2016 values, while the red bands are the AME 2016 uncertainty. The value of ^{138}Ce was calculated in three different ways, using ^{138}Ba , ^{136}Xe , and ^{138}La as reference masses. The three values are in good agreement and were used to calculate a weighted average value.

Table 4.5: Absolute mass measurements of ^{138}Ba and ^{138}Ce , given as the mass excess, calculated using ^{136}Xe as a reference ion. The column DM is the amount this measured mass excess deviates from the AME 2016.

Nuclide	ME (keV/c ²)		DM (keV/c ²)
	This Work	AME 2016	
^{138}Ba	-88 262.13(0.44)	-88 261.64(0.32)	-0.49(0.54)
^{138}Ce	-87 566.45(1.54)	-87 570.9(4.9)	4.45(4.9)

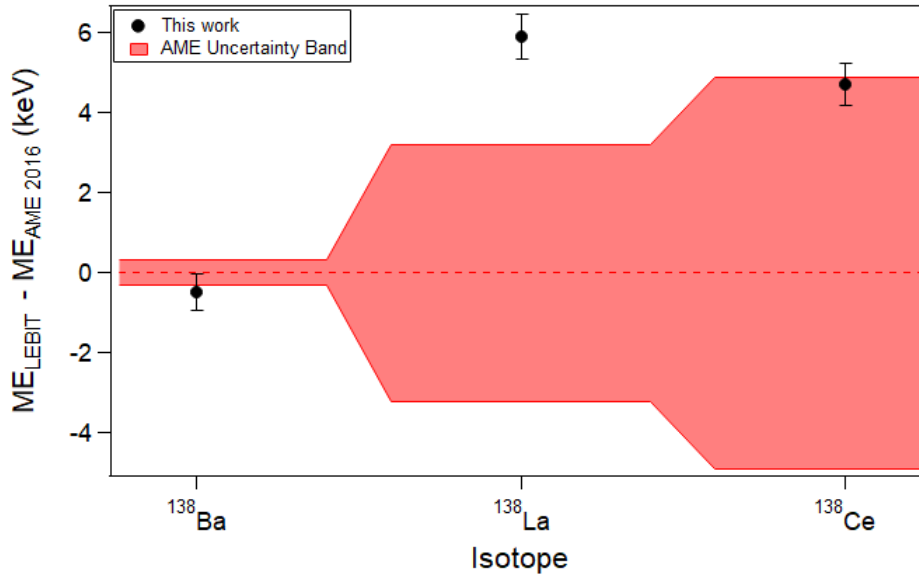


Figure 4.4: The weighted average Mass Excesses measured in this work compared to the AME 2016 values.

Table 4.6: Mass excesses, ME, for ^{138}Ba , ^{138}La , and ^{138}Ce . The results are compared to those listed in the AME 2016 [1]. The column ΔM is calculated as $\text{ME}_{\text{LEBIT}} - \text{ME}_{\text{AME2016}}$

Nuclide	Ref.	ME (keV/c ²)		ΔM (keV/c ²)
		LEBIT	AME 2016	
^{138}Ba	^{136}Xe	-88 262.13(0.44)	-88 261.64(0.32)	-0.49(0.54)
^{138}La	^{138}Ba	-86 513.44(0.57)	-86 519.2(3.2)	5.8(3.2)
	^{138}Ba	-87 567.12(0.84)		
	^{136}Xe	-87 566.45(1.54)		
	^{138}La	-87 565.43(0.74)		
^{138}Ce	Avg.	-87 566.21(0.52)	-87 570.9(4.9)	4.7(4.9)

4.3 Checking Systematics

The strong shift of both ^{138}La and ^{138}Ce away from the AME 2016 values, along with the heavy ^{138}Ba contamination, prompted checking of the systematics of the mass measurement technique. As mentioned in Ch. 3, the mass-dependent shifts of the system are regularly measured [25]. To reassure ourselves that the two mass unit difference between the isotopes of interest and ^{136}Xe would not affect the final results and to confirm that the contamination did not cause a frequency shift, measurements of $^{134}\text{Xe}^+$ and $^{136}\text{Ba}^+$ were performed using $^{136}\text{Xe}^+$ as a reference. These three isotopes are known to precisions of 0.009 keV, 0.3 keV, and 0.007 keV respectively, and thus would give an excellent test for any potential systematic errors [1]. A fresh barium source was placed on the LAS target holder to produce $^{136}\text{Ba}^+$ while the TIS, still fitted with a canister of xenon gas, was used to produce both $^{136}\text{Xe}^+$ and $^{134}\text{Xe}^+$. The ratios $^{136}\text{Ba}^+ / ^{136}\text{Xe}^+$ and $^{134}\text{Xe}^+ / ^{136}\text{Xe}^+$ were measured and used to calculate the mass excesses of ^{136}Ba and ^{134}Xe to a precision of approximately 0.3 keV. Both were in excellent agreement with the AME 2016, as can be seen in Table 4.7 and Fig. 4.5.

These results suggest that the ^{138}Ba contamination did not introduce any systematic

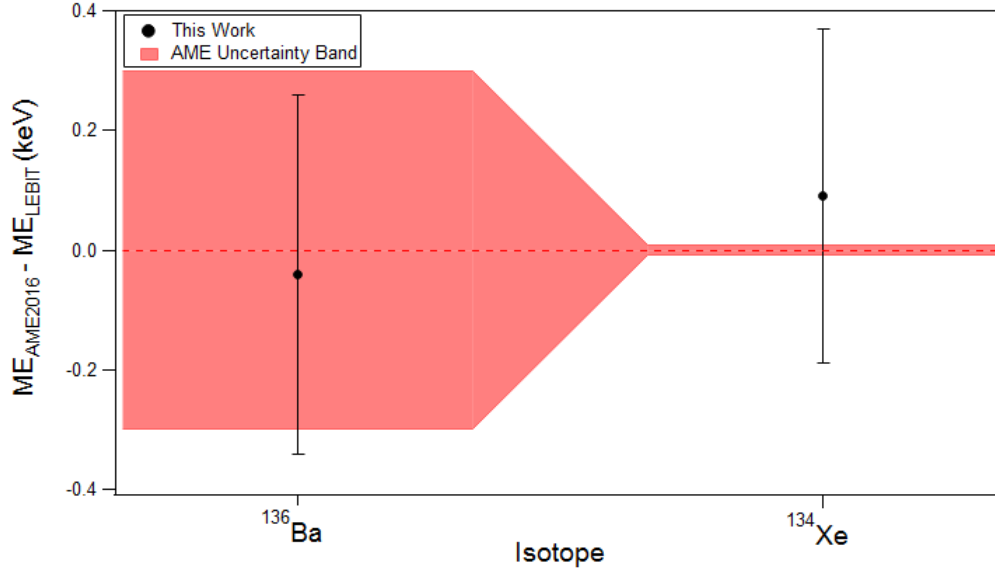


Figure 4.5: The Mass Excesses measured in this work to check for systematic shifts compared to the AME 2016 values.

errors and that the simultaneous shift of ^{138}La and ^{138}Ce away from the AME 2016 value was due to their connection in the literature.

Table 4.7: Absolute mass measurements of ^{136}Ba and ^{134}Xe , given as the mass excess, calculated using ^{136}Xe as a reference ion. The column DM is the amount the measured mass excess deviates from the AME 2016.

Nuclide	ME (keV/c ²)		DM (keV/c ²)
	This Work	AME 2016	
^{136}Ba	-88 886.94(0.30)	-88 886.9(0.30)	-0.04(0.30)
^{134}Xe	-88 125.73(0.28)	-88 125.822(0.009)	0.09(0.28)

4.4 Theoretical Calculations

4.4.1 Calculating the β -decay Spectrum Shape

Nuclear theorist collaborator Xavier Mougeot used the new Q -value as an input in the theoretical calculations for the $^{138}\text{La} \rightarrow ^{138}\text{Ce}$ β -decay spectrum. In this situation, the theoretical curve was fit to the spectrum measured by Quarati, *et al.* in Ref. [22] by applying an additional experimental shape factor, which took the form

$$C_{exp}(W) = 1 + aW + bW^2. \quad (4.2)$$

The parameters a and b can be found in Table 4.8, where they were calculated using the AME 2016 Q -value and again with the LEBIT Q -value. The LEBIT Q -value led to parameters with uncertainties more than an order of magnitude more precise.

Table 4.8: Adjusted parameters of the experimental shape factor $C_{exp}(W) = 1 + aW + bW^2$, to be applied on the theoretical shape factor to get the measured spectrum from [22]. Fitting procedure has been applied using the AME 2016 Q -value and the LEBIT Q -value.

Parameter	AME 2016	LEBIT
a	-1.32 (0.07)	-1.319 (0.006)
b	0.499 (0.043)	0.4982 (0.0038)
χ^2	9.0×10^5	8.8×10^5

The effect of this increased precision can be seen in Fig. 4.6. Shown here is the experimentally measured spectrum in black, with the classical theoretical curve shown in green and the theoretical spectrum, described in Sec. 2.1, with the addition of C_{exp} shown in red. The inset shows just the experimental shape factor, calculated using the AME 2016 Q -value and the LEBIT improved Q -value. The theoretical spectrum fits the experiment very closely

and the uncertainty in the fit is dramatically reduced.

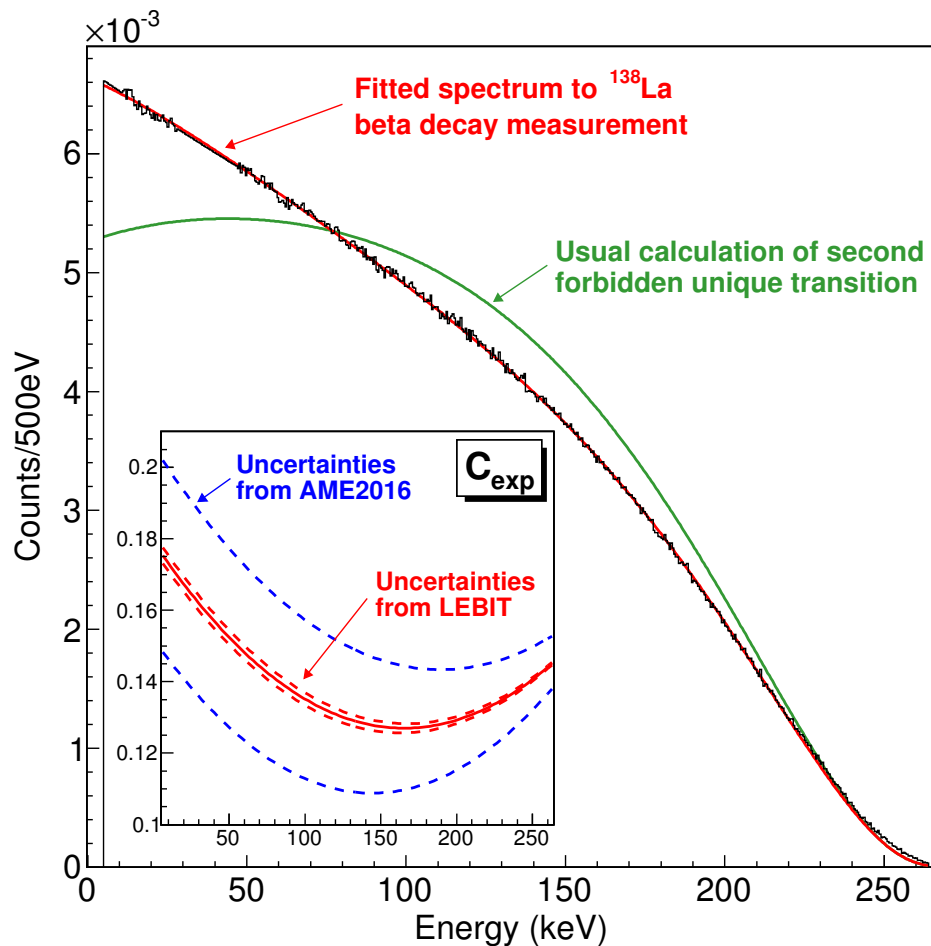


Figure 4.6: The measured ^{138}La β -decay spectrum by Quarati *et al.* (black line) fit using the LEBIT Q -value. The green line shows the classical theoretical calculation while the red line includes the experimental shape factor, C_{exp} . The inset shows the shape factor calculation using the AME 2016 Q -value versus using the LEBIT Q -value.

4.4.2 Calculating the Electron capture Probability Ratios

Additionally, the ϵ probability ratios for the decay of ^{138}La to ^{138}Ba were calculated for the L , K , and M shells. In ϵ -decay, an electron is absorbed by the nucleus from either the L , K , or M shell. This causes a proton to decay into a neutron and release an anti-electron

neutrino, as explained in the Introduction. Understanding the probability of electrons being absorbed from the different shells is necessary for a variety of applications, from radio nuclide metrology to nuclear energy [47]. In general, rather than calculating the absolute probabilities of an electron being absorbed from a specific shell, the ratios of probabilities of two shells are calculated, allowing nuclear structure components that are assumed to be constant for different electron orbitals to cancel. The capture probability ratios, calculated using the LEBIT Q -value, are a factor of three more precise than those calculated using the AME 2016 Q -value, as can be seen in Table 4.9. Using the LEBIT Q -value, there is excellent agreement between the experimental and theoretical values for the L/K ratio. These ratios can also be used to test nuclear models which assume that the L , K , and M subshells have different nuclear structure components, that do not cancel when taking the ratio.

Table 4.9: Theoretical predictions of the capture probability ratios for ^{138}La , using the AME 2016 Q -value and the LEBIT Q -value, compared with experimental results made by Quarati, *et al.*

EC Ratio	Experiment	AME 2016	LEBIT
L/K	0.391(3)	0.403(8)	0.3913(26)
M/K	0.102(3)	0.0996(24)	0.0964(10)
M/L	0.261(9)	0.247(8)	0.2464(30)

Part II

Ultra-Low Q -Value Decays

Chapter 5

Introduction to Ultra-Low Q -Value

Decays

Those spherical cows. You know, they're very hard to milk.

-Guy Savard

When discussing Q -value measurements taken by Penning trap mass spectrometry, what is being discussed is known as the “ground-state to ground-state” Q -value. This is because of the method by which Penning trap Q -value measurements are performed, mainly by measuring the ground-state masses of the parent and daughter nuclei and using Eqn. 1.5 to calculate the Q -value. However, the ground-state to ground-state Q -value is not the only decay channel possible and is often not the dominant one. It is also common for the parent nucleus to decay to an excited state of the daughter nucleus. When a decay occurs between the ground state of the parent nucleus and excited state of the daughter nucleus with an energy difference less than 1 keV, it is known as an ultra-low Q -value decay [48]. A diagram of this decay, specifically of ultra-low Q -value β -decay, can be seen in figure Fig. 5.1.

5.1 Studying Ultra-Low Q -value Decays

The first and only ultra-low Q -value decay observed was by Cattadori *et al.* in 2005, when the group at San Grasso National Laboratory measured the decay of ^{115}In to the first

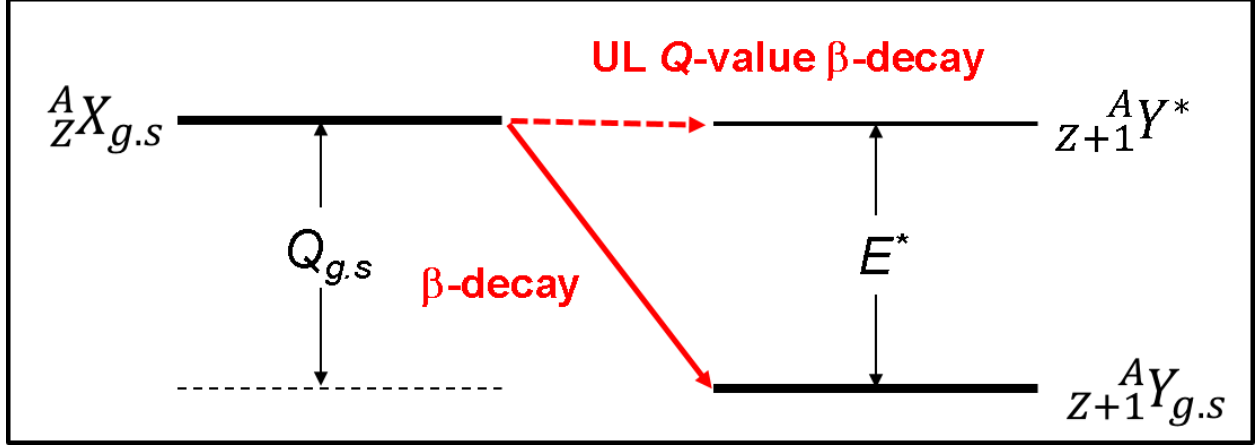


Figure 5.1: A schematic showing an ultra-low Q -value β -decay from the ground state of the parent to an excited state of the daughter.

excited state of ${}^{115}\text{Sn}$ [49]. From this discovery, ultra-low Q -value decays were discussed as potential probes for electron neutrino mass measurements independently in 2010 by Kopp and Merle [50] and by Mustonen and Suhonen [48]. The reason ultra-low Q -value decays could be useful for neutrino mass determination experiments is illustrated in Fig. 5.2. The most precise method currently used to evaluate the absolute mass of the electron neutrino is by studying the β -decay spectrum of low Q -value decays. The effect of the electron neutrino mass on the spectral shape near the endpoint can be seen in the right half of Fig. 5.2. If the electron neutrino is massless, the β -decay spectrum will end at the ground-state to ground-state Q -value energy, commonly called the endpoint. If the electron neutrino has a non-zero mass, the spectrum shape will change and end away from the Q -value energy. This can be described with the equation

$$\frac{dN}{dW} \propto pW(W_0 - W)[(W_0 - W)^2 - m_\nu^2]^{1/2} F_0 L_0 C(W), \quad (5.1)$$

where $\frac{dN}{dW}$ is the probability of an electron being released with a given energy W , p is the electron momentum, W_0 is the endpoint energy, F_0L_0 is the Fermi function, and $C(W)$ is a theoretical shape factor, also discussed in Sec. 4.4. Thus, collecting statistics very close to the endpoint of β -decay spectra is very important in order to gather information about the mass of the electron neutrino. For most decay spectra measurements, however, only a very small percentage of the statistics are found in this region. The smaller the Q -value of the decay, the smaller the range of possible electron energies and the larger the percentage of statistics found in the region close to the endpoint. Thus, ultra-low Q -value decays are good candidates for neutrino mass determination experiments. Currently, experiments attempting to measure the mass of the electron neutrino have focused on tritium, with a Q -value of 18.594(8) keV, ^{163}Ho , with a Q -value of 2.833(0.045) keV, and ^{187}Re , with a Q -value of 2.469(4) keV [1]. Ultra-low Q -value decays to excited states of the daughter nuclei could have Q -values more than an order of magnitude smaller than these three. As such, there has been a push in recent years to identify potential ultra-low Q -value decay candidates [50]. This requires high-precision measurements of the ground-state to ground-state Q -value, usually via Penning trap mass spectrometry, as well as high-precision measurements of the excited states of the daughter nucleus. By lowering the uncertainties on these two values, potential ultra-low Q -value decay candidates can be identified for further study.

It is important to note that discussing the “mass of the electron neutrino,” while appropriate for the cases discussed in this thesis, is misleading. The electron neutrino does not have a definite mass because it is a weak eigenstate, not a mass eigenstate. It is instead a superposition of the mass eigenstates ν_1 , ν_2 , and ν_3 , although it is predominantly ν_1 .

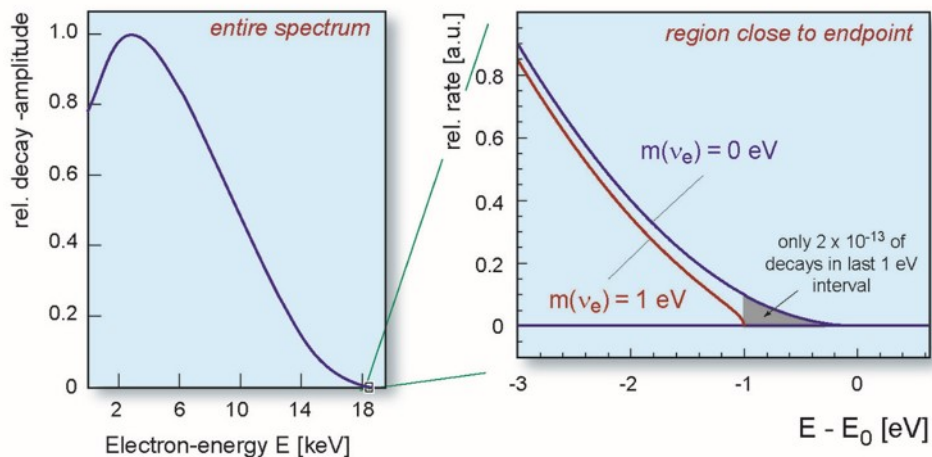


Figure 5.2: A sample β -decay spectrum (on the left) and a closer image of the possible shapes of the spectrum at the endpoint (on the right). An example spectrum where the electron neutrino is massless is shown in blue, while an example spectrum where the electron neutrino has a mass of 1 eV is shown in red. Decays with smaller Q -values have a greater percentage of statistics in this crucial endpoint region.

5.2 Theoretical Calculations of Ultra-low Q -value Decays

In response to the call in the 2005 Cattadori *et al.* paper for improved measurements of the $^{115}\text{In} \rightarrow ^{115}\text{Sn}$ ground-state to ground-state Q -value and half-life, Wieslander *et al.* at the University of Jyväskylä in Finland measured the transition using Penning trap mass spectrometry in 2009 [51]. The group also collaborated with HADES, an underground laboratory, to provide an improved measurement of the half-life of the decay through γ -ray spectrometry measurements. With a Q -value of only 0.35(17) keV from the ground state of ^{115}In to the first excited state of ^{115}Sn , it was the smallest known Q -value ever recorded by an order of magnitude, with the previous record being the decay of ^{187}Re , with a Q -value of 2.469(4) keV. The same year, the transition was measured independently by Mount *et*

al. at Florida State University with Penning trap mass spectrometry to the even greater precision of 0.155(24) keV [52]. In 2010, Mustonen and Suhonen began to investigate other aspects of nuclear theory that could be studied with the aid of what they coined “ultra-low Q -values” [48], beyond that of the mass of the neutrino. Using the two Q -value measurements from JYFLTRAP and FSU, as well as the half-life measurement from HADES, they plotted the experimental data alongside the theoretical relationship between half-life and Q -value:

$$T_{1/2} = \frac{1}{M^2 f_K(w_0, Z_f, R)} \quad (5.2)$$

Here, M is a nuclear matrix element and f_K is the phase space integral, which depends on the endpoint energy w_0 , the final nuclear charge Z_f , and the nuclear radius R . As can be seen in Fig. 5.3, there is a large discrepancy between this theoretical relationship and that actually seen in the experimental data. Mustonen and Suhonen attributed this discrepancy to four atomic interference effects whose current formulas do not extrapolate to the ultra-low Q -value regime. These effects are electron screening corrections and exchange effects, both discussed in Ch. 2, as well as atomic overlap and final-state interactions. Atomic overlap refers to the overlap of the wave function of the final state of the parent and the initial state of the daughter. The atomic wavefunctions are not perfectly equal—the ground state of the parent and the excited state of the daughter have different configurations. This imperfect overlap reduces the theoretical decay rate, increasing the half-life of the decay [53]. Final-state interactions are interactions between the released β particle (an electron or a positron) and the remaining atomic system, particularly with the atomic electrons [54].

Mustonen and Suhonen presented these findings at the Exotic Nuclei and Nuclear/Particle Astrophysics conference in Romania later in 2010. They reiterated the discrepancy between

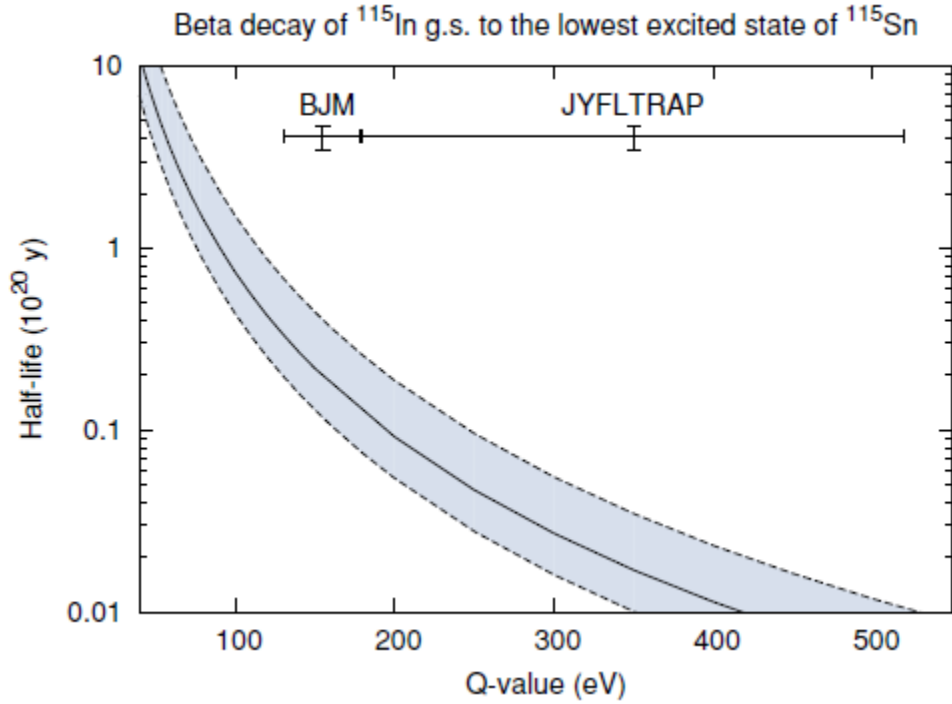


Figure 5.3: A plot from [48] of the HADES half-life measurement plotted against the JYFLTRAP (both [51]) and FSU (labeled BJM) ([52]) ultra-low Q -value measurements of $^{115}\text{In} \rightarrow ^{115}\text{Sn}$. The grey band on the graph is the theoretical relationship between half-life and Q -value, shown here with 30% confidence intervals. The discrepancy between experiment and theory points to missing atomic interference effects causing the half-life to be underestimated.

Table 5.1: A list of possible ultra-low Q -value decay candidates, from [50, 55, 56]. The column E^* gives the excitation energy of the daughter nucleus. The column Q_{UL} is calculated as $Q_{GS} - E^*$.

Parent	Daughter	Decay	Q_{GS} (keV)	E^* (keV)	Q_{UL} (keV)
^{75}Se	^{75}As	ϵ	864.7(0.9)	865.4(5)	-0.7(1.0)
^{75}Ge	^{75}As	β^-	1177.2(0.9)	1172.0(6)	5.2(1.1)
^{77}As	^{77}Se	β^-	683.2(1.7)	680.1035(17)	2.8(1.8)
^{79}Kr	^{79}Br	β^+	604(3)	606.03(6)	-2.2(3.3)
^{89}Sr	^{89}Y	β^-	1499.3(1.6)	1507.41(9)	-8.1(1.6)
^{109}In	^{109}Cd	β^+	993(4)	998(6)	-5(6)
^{111}In	^{111}Cd	ϵ	860(3)	864.8(3)	-4.8(3.0)
^{112}Ag	^{112}Cd	β^-	3991.1(2.4)	3990.4(1)	0.7(2.4)
^{113}Ag	^{113}Cd	β^-	2016(17)	2015.6(3)	0.4(17.0)
^{115}Cd	^{115}In	β^-	1451.9(0.7)	1448.787(9)	3.1(0.7)
^{115}In	^{115}Sn	β^-	497.489(0.01)	497.334(22)	0.155 (24)
^{139}Ba	^{139}La	β^-	2312.5(2.0)	2313(1)	-0.5(2.2)
^{131}I	^{131}Xe	β^-	970.8(6)	971.22(13)	-0.4(7)
^{135}Cs	^{135}Ba	β^-	268.9(1.0)	268.218(20)	0.5(1.1)
^{156}Eu	^{156}Gd	β^-	2452(3)	2449.7(1)	-0.6(5.8)
^{157}Eu	^{157}Gd	β^-	1365(4)	1377.4(2.2)	-12.9(5.1)
^{159}Gd	^{159}Tb	β^-	970.9(8)	971 ¹	-0.1
^{159}Dy	^{159}Tb	ϵ	365.2(1.2)	363.544(1)	1.7(1.2)
^{188}W	^{188}Re	β^-	349(3)	353.574(1)	-4.6(3.0)
^{193}Os	^{193}Ir	β^-	1141.9(2.4)	1145.61(1)	-3.7(2.4)
^{194}Ir	^{194}Pt	β^-	2228.4(1.3)	2223(2)	5.4(2.4)

the theoretical predictions and the experimental data, calling for both improved theoretical calculations for these effects and improved experimental data to guide and test the theory [55]. Along with the request, they included a table of potential ultra-low Q -value decay candidates. These candidates, along with several found by Kopp and Merle (see [50]) and our own search [56], can be found in Table 5.1.

In 2013, Haaranen and Suhonen examined the possibility of a $^{115}\text{Cd} \rightarrow ^{115}\text{In}$ ultra-low Q -value decay, specifically from the ground state of ^{115}Cd to the $9/2^+$ excited state of ^{115}In [57].

¹No uncertainty given in the Nuclear Database

Calling for improved experimental measurements of the ground-state to ground-state Q -value of the decay, they examined the theoretical half-life for the decay for a range of possible Q -values, creating a plot similar to that above made for the decay of ^{115}In to ^{115}Sn (see Fig. 5.4). To make this plot, they used the quasiparticle random-phase approximation (QRPA). In the paper, Haaranen and Suhonen used six values for the renormalization parameters for the QRPA fits and utilized two different values for the axial-vector coupling constant, g_A , which is described in detail in Ch. 2. With these six scenarios and two coupling constant values, they had a total of twelve plots for the dependence of the half-life of the decay on the Q -value of the decay. In Fig. 5.4, the dark grey band represents the area containing all twelve distinct plots. The light grey band represents the approximated systematic uncertainty in the calculations.

In order to test these theoretical calculations, it is necessary to have experimental data. Haaranen and Suhonen cited the value 1446(4) keV for the ground-state to ground-state Q -value. With an excited energy level of 1448.786 keV, this yields a potential ultra-low Q -value of -2.8(4.0) keV. The 2009 measurement by FSU of ^{115}In improved the uncertainty by an order of magnitude, from 4 keV to 0.012 keV [52]. Using this and the mass of ^{115}Cd available at the time gives a new ground-state to ground-state Q -value of 1445.8(2.7) keV and a potential ultra-low Q -value of -3.0(2.7). Since 2013, the uncertainty in the mass of ^{115}Cd has decreased from 2.7 keV/ c^2 to 0.7 keV/ c^2 . The current best mass value, taken from the AME 2016, gives a ground-state to ground-state Q -value of 1452.0(0.7) keV and a potential ultra-low Q -value of 3.2(0.7) keV. However, the improved precision of the ^{115}Cd mass did not come from direct measurements. Instead, it came from improved mass measurements of ^{114}Cd and ^{116}Cd , both of which are connected to ^{115}Cd in the AME by reaction measurements. Thus, it is necessary to measure ^{115}Cd directly to confirm the Q -value in the AME 2016 and

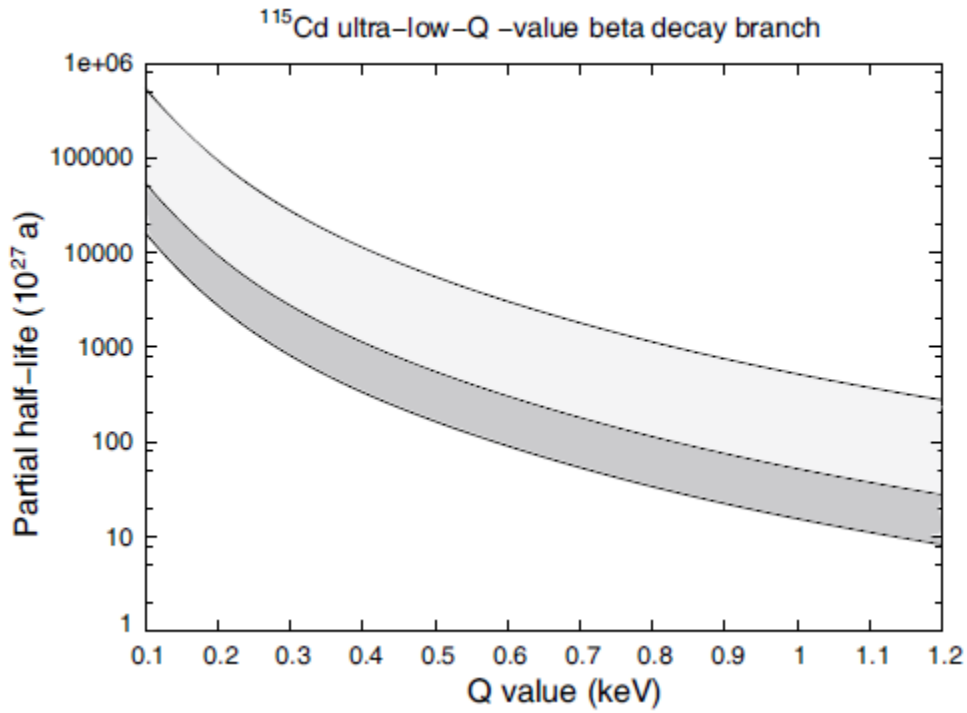


Figure 5.4: A plot from [57] of their theoretical calculations for $^{115}\text{Cd} \rightarrow ^{115}\text{In}$. The dark grey band on the graph is the theoretical relationship between half-life and Q -value, calculated using multiple values of the axial-vector coupling constant, g_A , and multiple scenarios for the QRPA (quasiparticle random-phase approximation) phonon fits. The light grey band shows the estimated systematic error in the calculations.

determine if an ultra-low Q -value is energetically possible. Additionally, other potential ultra-low Q -value decays should be measured in order to find the most potentially useful decays for neutrino mass determination studies. As discussed in the Introduction, Penning trap mass spectrometry is currently the most precise method of measuring nuclear masses and Q -values.

Chapter 6

The CPT Facility

Where is the signal? Oh, there it is, it just looks like crap.

-Rodney Orford

The Canadian Penning Trap (CPT) facility can be found at Argonne National Laboratory (ANL). ANL is a DOE-funded national laboratory which houses the CALifornium Rare Isotope Breeder Upgrade (CARIBU). CARIBU is a 1 Ci ^{252}Cf source housed inside a gas catcher [58]. ^{252}Cf decays via spontaneous fission and creates fission fragments with two fission peaks centered around $A = 107$ and $A = 141$ [59]. With the gas catcher enabling the stopping and extraction of these isotopes, CARIBU can create a variety of usable beams. A schematic of the CARIBU source, as well as the beamline to the CPT facility, can be seen in Fig. 6.1.

6.1 CARIBU

CARIBU consists of a ~ 1 Ci ^{252}Cf source, a recent upgrade from the initial 100 μCi source. ^{252}Cf decays via α -decay and spontaneous fission. The α -decay, which accounts for approximately 97% of the decays, yields ^{248}Cm , which itself can decay via α -decay and spontaneous fission. The remaining 3% of decays are spontaneous fission, producing a large number of neutron-rich nuclides. In Fig 6.2, the portion of the chart of the nuclides created

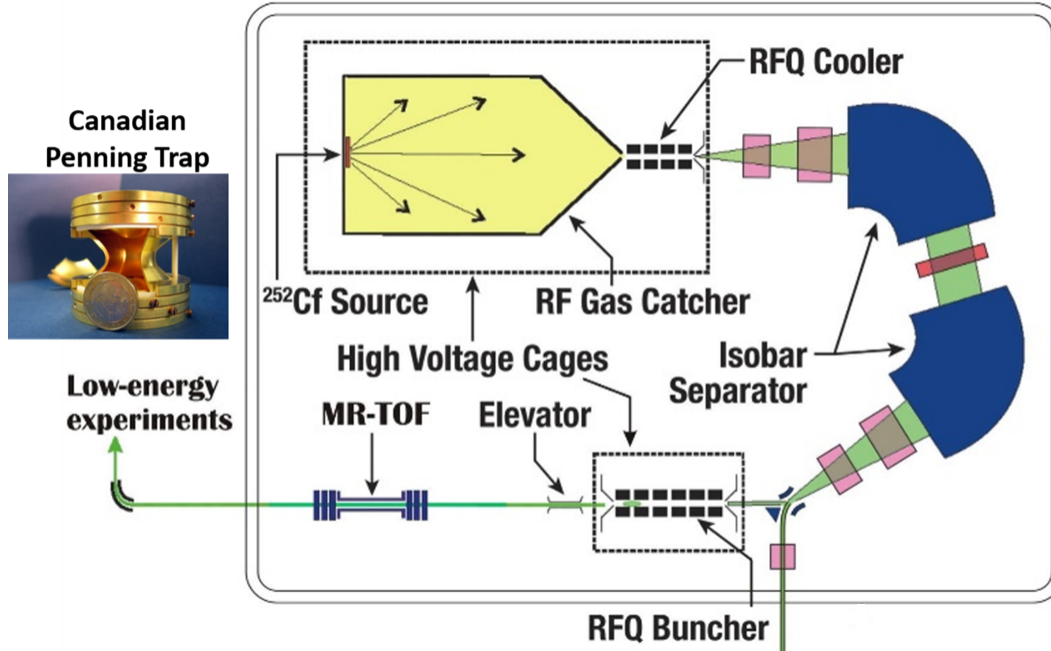


Figure 6.1: A schematic of the CaRIBU source and the beamline leading to the CPT facility.

by CARIBU fission fragments can be seen with approximate yields per hundred fissions of ^{252}Cf [60].

Unfortunately, the fragments created by this spontaneous fission sources are high in energy. For ^{252}Cf specifically, fission fragments have an average kinetic energy of 182 MeV as measured by Mitton and Fraser [61]. As mentioned in the Introduction, it is necessary for beams to have only a few tens of eVs as they enter a Penning trap. Fragments from spontaneous fission sources also have a high transverse emittance, meaning there is a large spread in the position and momentum of the fragments. Beams must have a low position spread to efficiently enter the small aperture in a Penning trap endcap and a low momentum spread to be efficiently trapped. CARIBU resolves this problem by placing the entire ^{252}Cf source within a gas catcher (see Fig. 6.1).

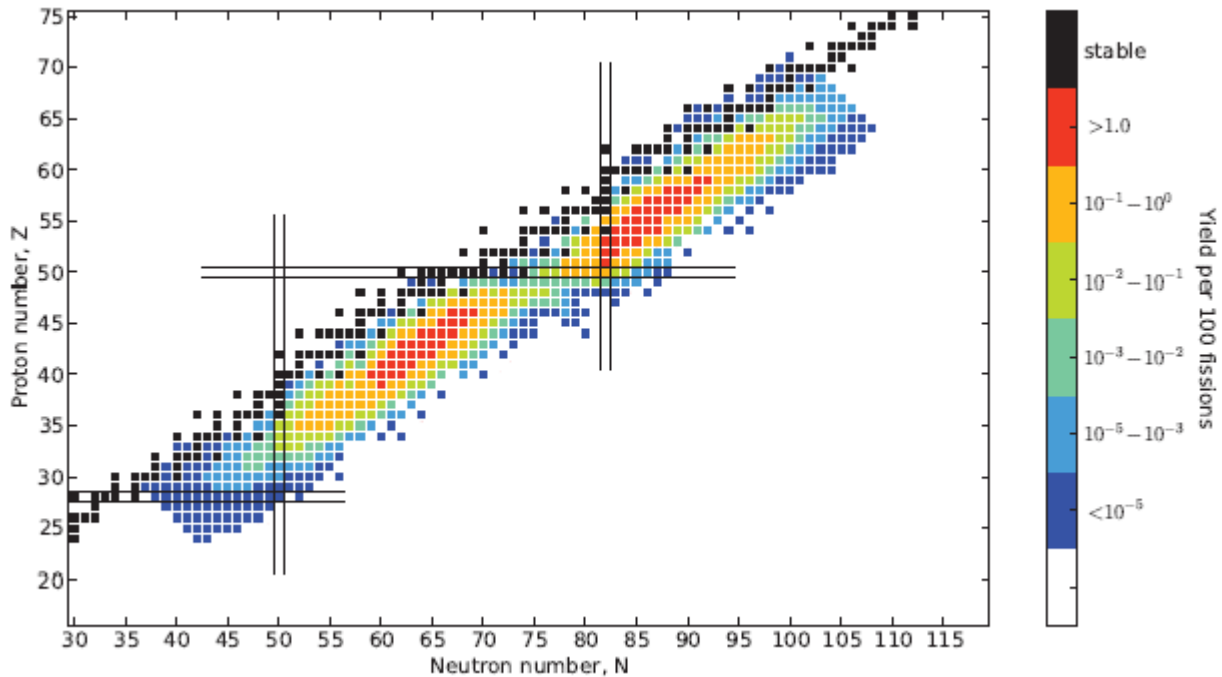


Figure 6.2: The portion of the chart of the nuclides containing ^{252}Cf fission fragments, from [60]. The color corresponds to the yield of the nuclide per 100 fissions of ^{252}Cf .

6.1.1 The Gas Catcher

The gas catcher currently in use at CARIBU was developed at Argonne in 1998. As mentioned in the Introduction, gas cells were a necessary addition to precision mass measurement facilities at laboratories that produce rare isotopes at high energies, such as fragmentation facilities. As such, the gas catcher was originally designed to allow fusion-evaporation products to be injected into the CPT [62]. With the implementation of CARIBU, it has been re-purposed to thermalize ^{252}Cf fission fragments. The gas catcher consists of two parts, a cylindrical body and a conical head, tapering to an aperture. The catcher is filled with high-purity helium gas and includes a radiofrequency quadrupole (RFQ) field and an axial DC electric field. The fragments are thermalized by interacting with the helium gas, the RFQ confines them radially, and the DC field drags them through the gas catcher to eject

them.

The gas catcher can be seen in Fig. 6.1, in yellow. The entirety of the ^{252}Cf source sits within the catcher, mounted on a stainless steel plate at the back of the cylindrical body. Fission fragments are released at a variety of angles and energies, shown in the figure by black arrows. These fragments pass through a gold degrader foil, which lowers their energy before they are further thermalized by the helium gas. Collisions with the helium further lowers the energy and transverse emittance of the fragments. As ions move from the cylindrical body of the catcher to the conical head, the RFQ of the cone can be tuned to provide a measure of contamination removal. By lowering the power of the field, large contamination molecules maintain a large radius as the cone narrows, preventing them from exiting the gas catcher. The remaining ions then pass through the aperture at the end of the gas catcher to enter an RFQ cooler. Again, this is similar in design and function to the cooler described in Chapter 3.2 and reduces the energy and emittance of the beam to the point where it is usable as a source of rare ions for a variety of experiments and measurements [60].

6.1.2 The Isobar Separator

Ions are extracted from the cooler and sent into an isobar separator, which can be seen in Fig. 6.3. The separator is composed of two bending magnets, both making 60° angles, and is capped with quadrupolar focusing and defocusing magnets [63]. It was designed with the constraints of the CARIBU in mind—it needed to be compact enough to fit on the high voltage platform, visible in Fig. 6.1, while maintaining a high resolution and a high transmission rate for the desired ions. Ions enter the separator and are defocused before entering the bending magnets. This allows for a high mass dispersion and improves selection. The bending magnets are focused such that the ions of interest are kept near the

center of the beamline, while heavier and lighter ions are pushed to the sides to bend too steeply or too shallowly. The ions which successfully make it through both bending magnets are refocused into a tight, usable beam. From here, the ions are sent either to ATLAS (the Argonne Tandem Linac Accelerator System) to be accelerated to medium energies or to low-energy experiments such as CPT or β -decay studies.

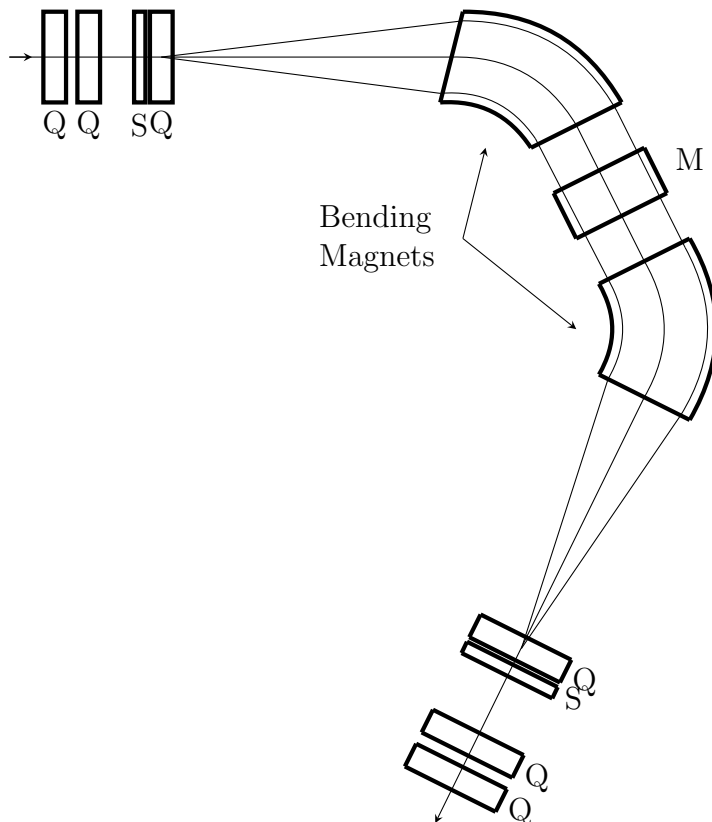


Figure 6.3: A schematic of the CARIBU isobar separator, from [63]. Q are quadrupole doublets, S are sextupole singlets, and M is an electrostatic multipole.

The isobar separator in theory can reach a separation resolution of $\frac{m}{\Delta m} \sim 20000$, but in practice operates around $\frac{m}{\Delta m} \sim 14000$ [64]. At mass number $A = 115$, this allows for separation of masses of about 8.2 mu. For comparison, ^{115}In and ^{115}Cd are approximately 1.6 mu apart. Therefore, to further remove contamination species, a multi-reflection time of

flight mass separator (MR-TOF) was installed after the buncher in 2015. This addition is visible in Fig. 6.1.

6.2 The Multi Reflection Time of Flight Mass

Separator

Multi-reflection time of flight mass separators (MR-TOFs) are fast, high-resolution mass separators that work by reflecting bunches of ions back and forth between two electrostatic mirrors [65]. MR-TOFs have been in use since the early 1990s and, due to their speed, resolution, and compact size, are becoming more and more popular at various laboratories as ways of quickly removing contamination from beams before they are sent to precision experiments.

The MR-TOF at CARIBU was installed in 2015 and commissioned in 2016 as a way to improve the removal of contaminant ions from the beam before it is sent to CPT or other low-energy experiments connected to CARIBU [64]. The MR-TOF consists of a drift electrode capped on either side by electrostatic mirrors. The mirrors include six mirror electrodes separated by shielding electrodes. The voltage on each mirror electrode can be changed independently while the shielding electrodes are held at midway voltages to prevent sharp changes.

Ions are injected into the MR-TOF in bunches. The drift electrode voltage is lowered to trap the bunches, which are then reflected between the mirror electrodes several hundred times [66]. When injected, the ions in each bunch all have the same kinetic energy, $E = \frac{1}{2}mv^2$. Ions of different species have different masses, and thus travel at different velocities. The MR-TOF increases the distance ions travel between the buncher and the experimental

setups. The further the ions travel, the larger the separation between ions of different species and mass (see Fig. 6.4). Once the ions are sufficiently separated by their time of flight, they are ejected from the MR-TOF. CPT uses a Bradbury-Nielsen Gate (BNG) after the MR-TOF. A BNG is a series of wires forming a grid orthogonal to the path of the beam. A high-frequency voltage is applied to alternating wires. The beam can only pass through the gate undeflected when the potential between adjacent wires is zero. Theoretically, the resolving power of the MR-TOF is $\delta m/m \sim 10^{-5}$, but in practice operates around $\delta m/m \sim 2 \times 10^{-4}$. Additionally, for ions with shorter half-lives, mass resolution must be sacrificed to maintain a sufficiently short amount of time in the MR-TOF (under 30 ms).

6.3 The Stable Ion Source

The Argonne Stable Ion Source (SIS) sits at the base of the CPT tower, which will be described in the following section. The SIS provides stable ions, used to calibrate the Penning trap. It consists of a cesium salt on top of a heating element, which creates $^{133}\text{Cs}^+$ ions via surface ionization [60]. ^{133}Cs is the only stable isotope of cesium and is one of the most precisely measured masses, at $0.009 \mu\text{u}$, or $\delta m/m \sim 7 \times 10^{-11}$ [67]. This precision and availability make it an ideal isotope for calibration uses.

6.4 The Penning Trap and Magnet

The CPT facility uses a hyperbolic Penning trap, seen in Fig. 6.5. The trap was originally built at the Tandem Accelerator Superconducting Cyclotron Facility at Chalk River

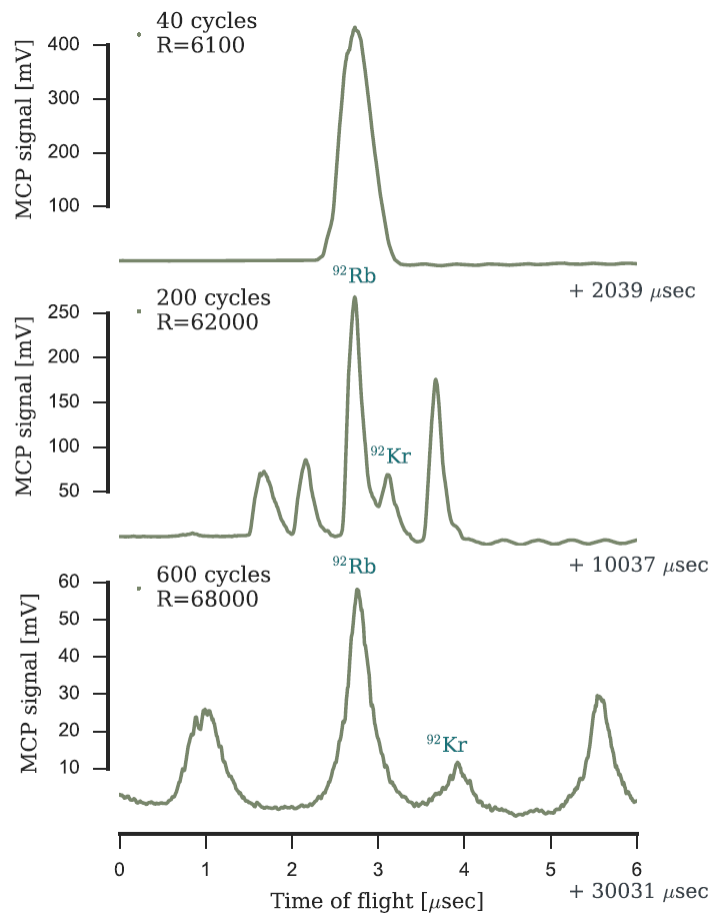


Figure 6.4: The mass separation of ion species using the MR-TOF, from [64]. The top plot shows the initial bunch, with minimal separation of ion species after 40 cycles, with 2 reflections per cycle. The middle plot shows the time of flight separation of the desired ions and the contaminants after 200 cycles, and the bottom plot shows the same after 600 cycles.

Laboratories in Ontario, Canada [68]. The facility was shut down in 1997, however, and the trap was moved to ANL for continued use [69].

The trap itself sits within a 5.7 T superconducting magnet at the top of a four meter tower [60]. A simplified schematic of the tower can be seen in Fig. 6.6. Ions exit the MR-TOF and are injected near the base of the tower, above the SIS, where they pass through a 90° bender.



Figure 6.5: The Canadian Penning Trap (CPT), shown here with a Canadian gold dollar for scale.

The Penning trap itself at CPT is identical in its construction and basic operation to the LEBIT Penning trap, which is described in detail in Sec. 3.3. For brevity, the description will not be repeated here and instead only the difference in techniques will be described.

6.5 Phase Imaging Ion Cyclotron Resonance

6.5.1 Mechanism

The CPT facility was initially designed to use Time of Flight Ion Cyclotron Resonance (TOF-ICR), which is discussed in detail in Section 3.4. Over the past several years, however, the facility was modified to use a new technique known as Phase Imaging Ion Cyclotron Resonance, or PI-ICR. This method was first developed and demonstrated in 2012 by Eliseev

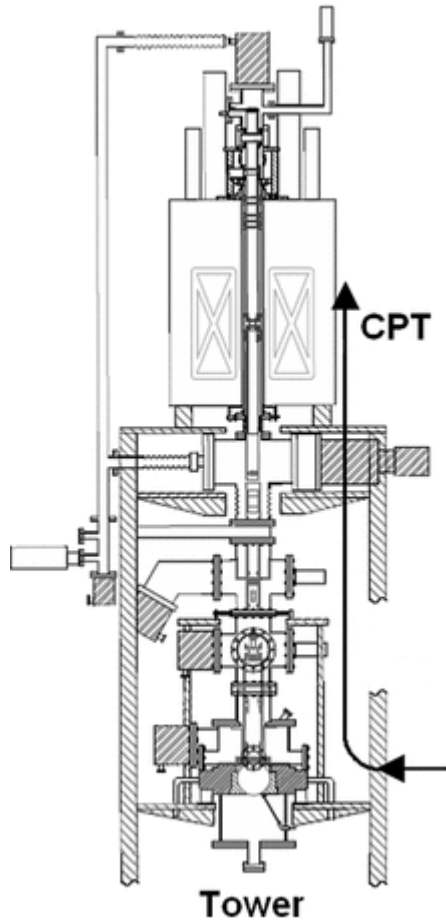


Figure 6.6: A schematic of the tower containing the CPT, from [70].

et al. at the SHIPTRAP facility at GSI [12]. In this method, ions are injected into the trap. An initial, dipolar RF pulse is applied at the modified cyclotron frequency, f_+ of the ions to give them an initial average cyclotron radius, ρ_+ . The ions are then allowed to revolve freely inside the trap for a pre-determined accumulation time, t_{acc} . During this time, they accumulate a frequency and mass-dependent phase. After the time t_{acc} has elapsed, a quadrupolar RF pulse is applied at the true cyclotron frequency, f_c , to convert the motion of the ions from modified cyclotron motion to pure magnetron motion. The ions are then ejected from the trap towards a position-sensitive detector. They pass through a changing magnetic field to be projected onto the detector and the position around the circle of radius

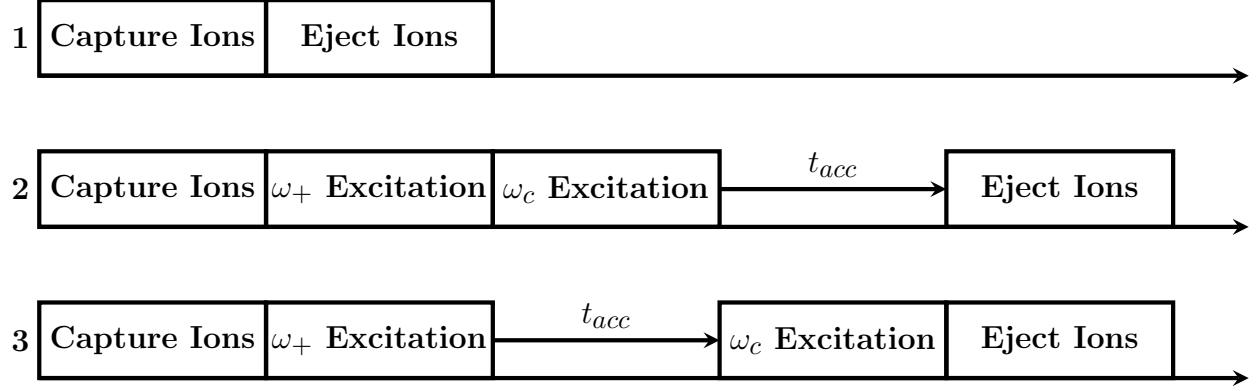


Figure 6.7: A diagram of the pulse timings for PI-ICR. Step 1 establishes the center of the detector. Step 2 creates a reference spot. Step 3 creates the final spot. The total trap time is the same for steps 2 and 3.

R is measured. By converting the ion motion from modified cyclotron motion to magnetron motion before ejection, the ion motion is slowed and potential smearing of the spot on the detector is prevented. To obtain a reference spot, a quadrupolar RF pulse at the cyclotron frequency is applied immediately after the ions reach their initial radius, ρ_+ . The ions remain in the trap without accumulating phase for the same t_{acc} so the overall time in the trap is consistent. The ions are then ejected from the trap towards the position-sensitive detector and the position of the reference spot around the circle of radius R is measured (see Fig. 6.7).

The angle between the reference spot and the final spot (see Fig. 6.8, where the reference spot is labeled 2 and the final spot is labeled 3), here labeled as ϕ , can be measured and used to find the true cyclotron frequency of the ion, via the relation:

$$f_c = \frac{\phi + 2\pi n}{2\pi t_{acc}}, \quad (6.1)$$

where n is the number of full rotations the ions make during t_{acc} . The value of n cannot be determined directly, so it is calculated using a B-field calibration with a reference ion

of well-known mass and the mass of the ion of interest from the AME. The center of the detector, the spot labeled 1 in Fig. 6.8, is measured regularly but remains relatively constant.

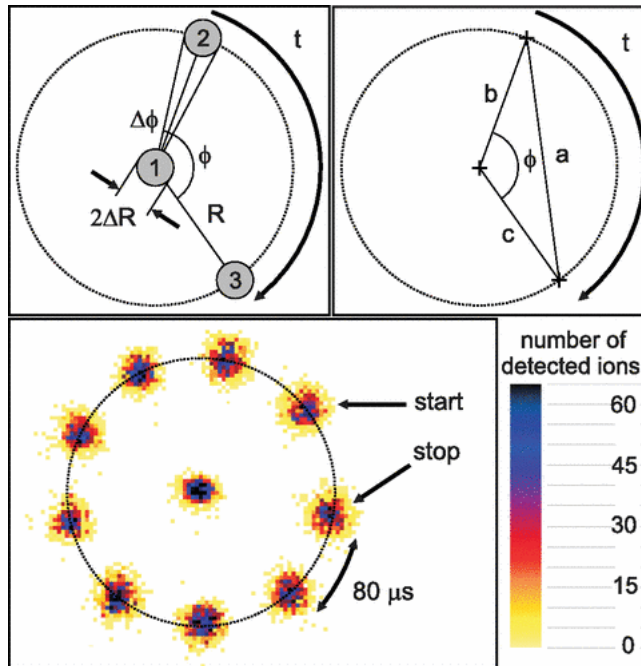


Figure 6.8: A diagram of the method of PI-ICR, from [12]. In the schematic view in the upper left, spot (1) is the center of the position-sensitive detector, spot (2) is the location of the reference spot, taken with $t_{acc} = 0$, and spot (3) is the final spot, taken with $t_{acc} > 0$.

6.5.2 Magnetic Field Calibration

At CPT, the magnetic field is calibrated by taking a precise PI-ICR measurement of ^{133}Cs from the SIS every few days. Then, during measurements of ions, a reference spot is established approximately every three to five measurements. This is significantly less frequent than what is used with TOF-ICR at LEBIT, where a reference measurement of a well-known ion is taken before and after every measurement of an ion of interest (described in Sec. 3.4.2). This is possible because the CPT magnet is very stable, with a magnetic

field change of only about 3×10^{-10} T per day [60]. With a low decay rate, reference measurements only need to be taken every few hours. Additionally, stable contaminants in the beam (see the next section) create separate spots from the ions of interest during the f_c measurements. The cyclotron frequency of these spots can be determined with Eqn. 6.1 identically to the spots created by the ions of interest, serving as additional checks of the magnetic field strength and stability during the measurements themselves.

6.5.3 Contamination Separation

The resolving power of PI-ICR is highly lauded in its ability to quickly resolve molecular contaminants, isobars, and even nuclear isomers. Seen in Fig. 6.9, several contaminants coming in the beam hit the detector at the same point during the reference measurement. After a short accumulation time of 2 ms, however, the ion of interest, $^{142}\text{Cs}^+$, began to separate from the contamination. With a slightly longer accumulation time of 5 ms, $^{142}\text{Cs}^+$ was fully resolved from the $^{142}\text{Xe}^+$ and the molecular contaminant, ICH_3^+ . Resolving similar contaminants using TOF-ICR would take approximately 200 ms, a factor of 40 lower resolving power [71].

An additional advantage the PI-ICR contamination separation has over the in-trap cleaning for TOF-ICR (discussed in detail in Sec. 3.4.1.1) is the avoidance of additional modified cyclotron excitation. With in-trap cleaning pulses, the contaminants are driven at their modified cyclotron frequencies to drive them into the trap walls. When the contaminants are too close to the ions of interest, however, the cleaning pulse may also drive the modified cyclotron motion of the ions of interest, either cleaning them or damaging the quality of the resonances. While this can sometimes be mitigated by increasing the length of the cleaning pulse to make it more narrow, it is often not possible to clean close contamination without

damaging or destroying the resonance. The time necessary for this in-trap cleaning can also sometimes make it impossible to measure ions with short half-lives, as they may decay in the trap before the cleaning is complete.

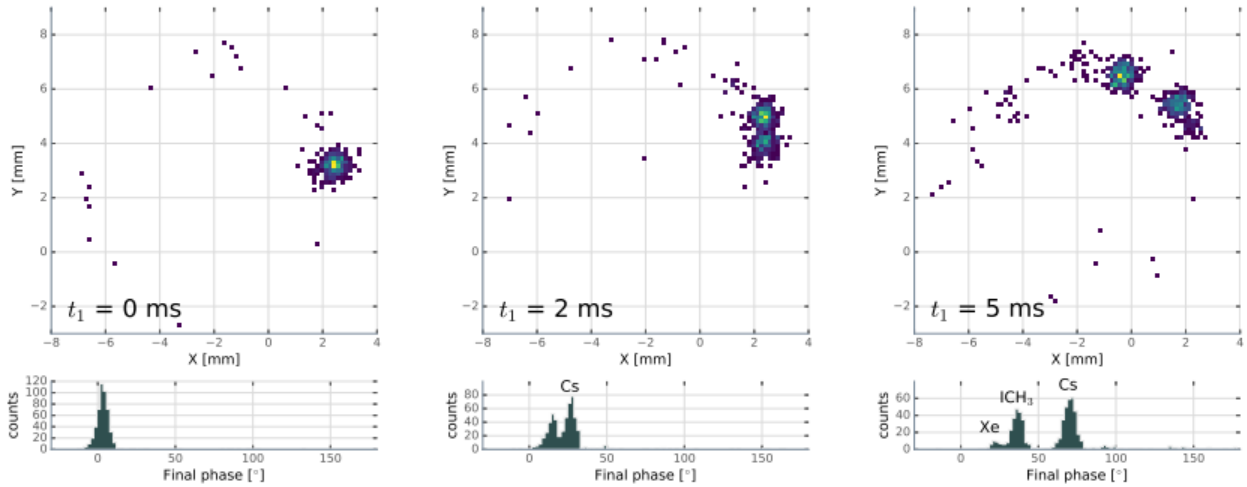


Figure 6.9: An example of the separation of contamination using PI-ICR, from [71]. Shown here are the projection of ions on the position-sensitive detector as well as histograms of the measured phases of the ions for 0, 2, and 5 ms accumulation times. The ions and contaminants, ^{142}Cs , ^{142}Xe , and ICH_3 , are labeled in the histograms as they are resolved.

Chapter 7

Measurement of $^{112,113}\text{Ag}$ and ^{115}Cd

β -Decay Q -values

Everything is broken. Nothing works.

-Sam Lipschutz

The measurements of $^{112,113}\text{Ag}$ and ^{115}Cd β -decay Q -values were performed at the CPT facility at ANL (see Chapter 6 for a full description of the facility). The measurements were performed over two beam times, with data being taken first in October of 2016 and then again in November of 2018. Additionally, data of the stable and long-lived isotopes ^{115}Cd , ^{115}Sn , and ^{115}In were taken in January of 2017 by Rodney Orford, at the time a graduate student working with the CPT. The decays in question can be seen in Table 7.1. The data for the ground state Q -values and the excited state energy levels were taken from the AME 2016 and the NNDC [1, 43]. For both sets of beam time data, isotopes of $^{112,113}\text{Ag}$, $^{112,113,115}\text{Cd}$, $^{112,115}\text{Sn}$, and ^{115}In were created via the CARIBU source (discussed in Section 6.1).

The results presented in this chapter are being prepared for publication in the Physical Review C. Additional details and discussion are included here, as well.

Table 7.1: The list of potential ultra-low Q -value decay candidates studied using the Canadian Penning Trap at Argonne National Laboratory. Q_{gs} values were obtained using mass data from the AME 2016 [1]. The column E^* gives the excitation energy of the daughter nucleus from the NNDC [43]. The column Q_{UL} is calculated as $Q_{GS} - E^*$.

Parent	Daughter	Decay	Q_{GS} (keV)	E^* (keV)	Q_{UL} (keV)
^{112}Ag	^{112}Cd	β^-	3991.1(2.4)	3990.4(1)	0.7(2.4)
^{113}Ag	^{113}Cd	β^-	2016(17)	2015.6(3)	0.4(17.0)
^{115}Cd	^{115}In	β^-	1451.9(0.7)	1448.787(9)	3.1(0.7)
^{115}In	^{115}Sn	β^-	497.489(0.01)	497.334(22)	0.155 (24)

7.1 First Experiment—October 2016

7.1.1 Data Collection

The first beam time at the Canadian Penning Trap facility ran from October 20, 2016 to October 23, 2016. The 20th, 21st, and 22nd were used to measure ^{112}Ag , ^{112}Cd , and ^{112}Sn , respectively. ^{113}Ag and ^{113}Cd were also briefly measured on the 22nd. The 23rd was used to measure ^{115}Cd , ^{115}In , and ^{115}Sn .

For the first beam time, measurements were alternated following the pattern: reference measurement, daughter measurement, reference measurement, and parent measurement. While the description in Chapter 6 indicated that regular reference measurements are not necessary, an unstable power supply in use at the time led to field fluctuations and additional reference measurements were taken in order to correct systematic errors. The in-trap accumulation time, t_{acc} was kept constant for each measurement set. For most of the parent-daughter pairs, multiple sets of data were taken, each with a different t_{acc} . For example, for the $^{115}\text{Cd} \rightarrow ^{115}\text{In}$ measurements, five measurements were taken where t_{acc} for ^{115}In was 348.724 μs and t_{acc} for ^{115}Cd was 348.847 μs . Later, seven measurements were taken where t_{acc} for ^{115}In was 640.000 μs and t_{acc} for ^{115}Cd was 630.052 μs . The accu-

Table 7.2: The parent-daughter ion pairs measured in October of 2016, along with the accumulation times for each and the number of measurements taken for each accumulation time.

Parent	P t_{acc}	Daughter	D t_{acc}	N
^{112}Ag	90.003	^{112}Cd	145.236	5
	145.015		145.236	5
	345.017		340.240	6
	845.452		845.449	3
^{112}Sn	310.492	^{112}Cd	340.240	6
^{113}Ag	545.007	^{113}Cd	545.146	2
^{115}Cd	348.847	^{115}In	348.724	5
	348.848		348.725	4
	630.052		640.000	7
^{115}Sn	348.817	^{115}In	348.724	5
	348.818		348.725	4

mulation times were chosen to put all four measurement spots and the reference spots at the same location on the position sensitive MCP detector, to prevent systematic errors from possible detector misalignment and dead spots.

7.1.2 Data Analysis

Through the rest of 2016, the frequencies measured for the various isotopes were analyzed and the measured ratios were used to calculate the Q -values for each decay. Q -values were calculated for the decays of $^{112}\text{Ag} \rightarrow ^{112}\text{Cd}$ and $^{115}\text{Cd} \rightarrow ^{115}\text{In}$, as described in the proposal, as well as for the decays of $^{112}\text{Sn} \rightarrow ^{112}\text{Cd}$ and $^{115}\text{In} \rightarrow ^{115}\text{Sn}$ to use as systematic checks. Only two measurements were taken for the decay of $^{113}\text{Ag} \rightarrow ^{113}\text{Cd}$ because the measured Q -values were substantially larger than the AME 2016 values, eliminating it as an ultra-low Q -value decay candidate. Thus, high precision was decided to be unnecessary and the beam time was devoted to continuing measurements of the 112 and 115 mass regions.

Table 7.3: The average Q -values measured by CPT in October of 2016, along with the ranges measured and values from the AME 2016 [1].

Decay	AME 2016 (keV)	CPT Ave. (keV)	CPT Range (keV)	N
$^{112}\text{Ag} \rightarrow ^{112}\text{Cd}$	3991.1(2.4)	3992.50	21.96	19
$^{112}\text{Sn} \rightarrow ^{112}\text{Cd}$	1919.80(16)	1931.75	5.24	6
$^{113}\text{Ag} \rightarrow ^{113}\text{Cd}$	2016(17)	2084.81	3.54	2
$^{115}\text{Cd} \rightarrow ^{115}\text{In}$	1451.9(0.7)	1450.28	6.51	16
$^{115}\text{In} \rightarrow ^{115}\text{Sn}$	497.489(0.010)	499.90	4.16	9

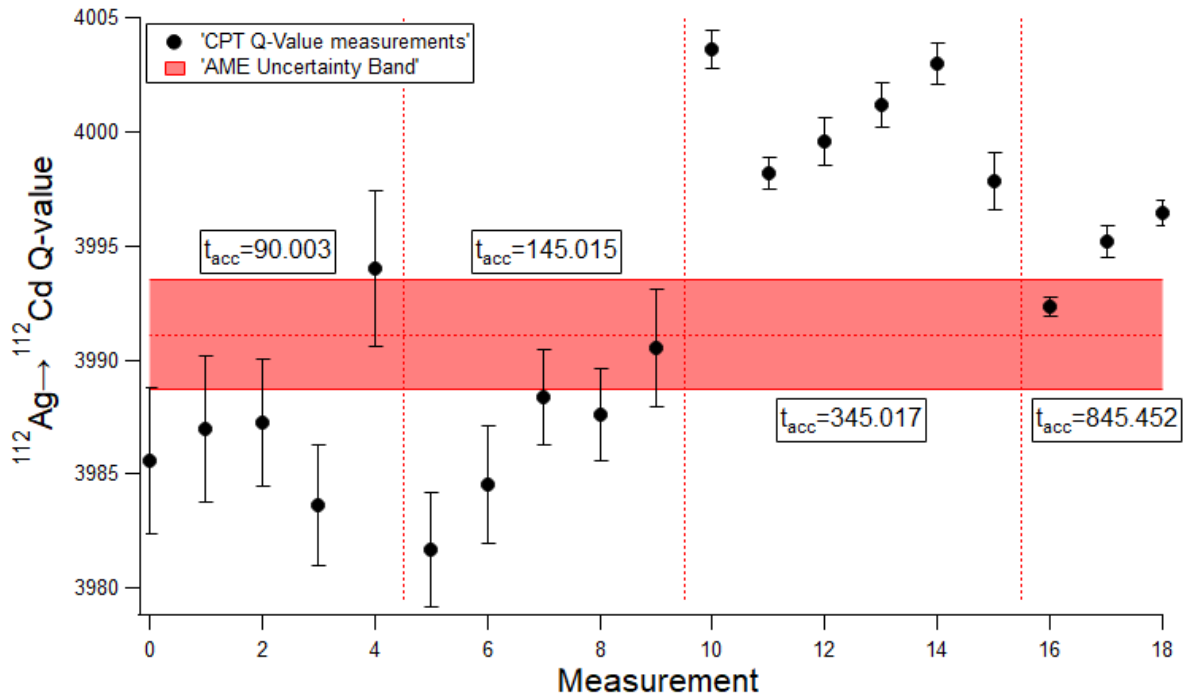
During initial data analysis, it was realized that the measured Q -values were widely scattered. In Table 7.3, the average Q -values can be seen compared to the AME 2016, as well as the range of values in which the data fell. This is further illustrated in Fig. 7.1. When plotting the data, it was apparent that the Q -values formed clusters. For a given accumulation time, the data were fairly self-consistent. However, changing t_{acc} created dramatic changes in the measured Q -values.

Further analysis revealed that the change in the Q -value was correlated to a change in the radius for different t_{acc} times (see Fig. 7.2). The angle between the reference spot and the final spot, ϕ , is calculated as

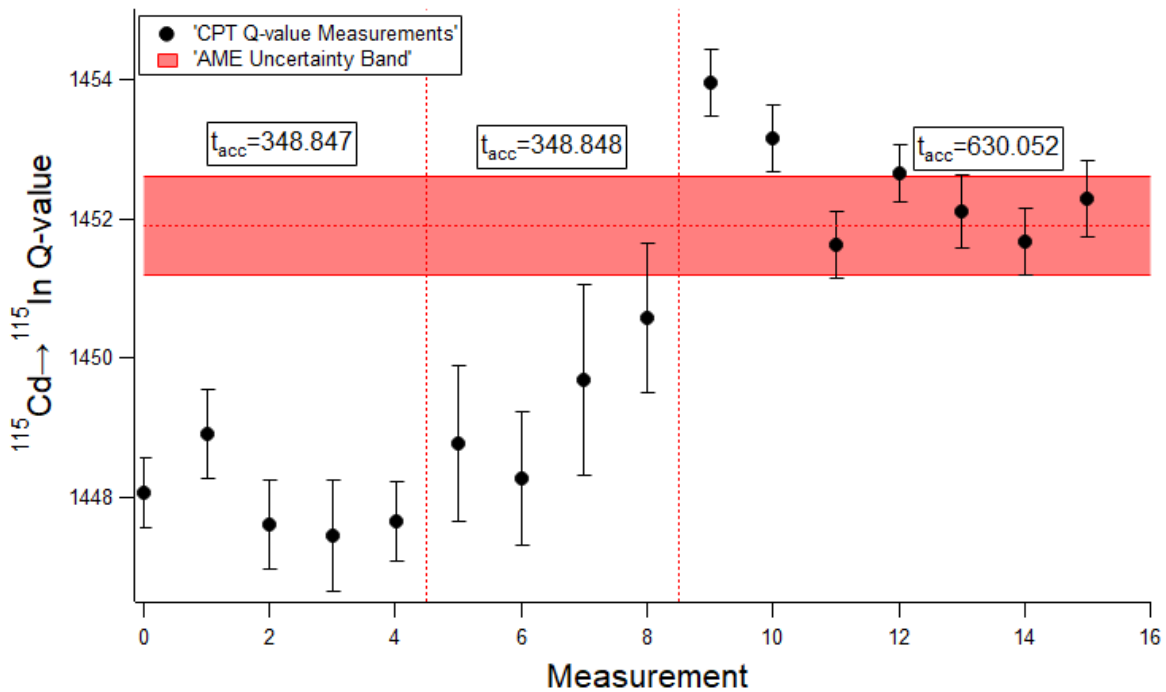
$$\phi = \cos^{-1} \left(\frac{r_{ref}^2 + r_{ion}^2 - a^2}{2r_{ref}r_{ion}} \right), \quad (7.1)$$

where r_{ref} is the radius the reference spot, r_{ion} is the radius of the final spot, and a is the chord between the reference spot and the final spot. Theoretically, the reference and final spots should lie on a common circle and ϕ should be calculated as

$$\phi = \cos^{-1} \left(1 - \frac{a^2}{2r^2} \right). \quad (7.2)$$



(a) $^{112}\text{Ag} \rightarrow ^{112}\text{Cd}$ Q -value measurements.



(b) $^{115}\text{Cd} \rightarrow ^{115}\text{In}$ Q -value measurements.

Figure 7.1: Data taken at the CPT facility in October of 2016. The top shows the measured $^{112}\text{Ag} \rightarrow ^{112}\text{Cd}$ Q -values while the bottom shows the $^{115}\text{Cd} \rightarrow ^{115}\text{In}$ Q -values. The red bands show the uncertainty in the AME 2016 [1].

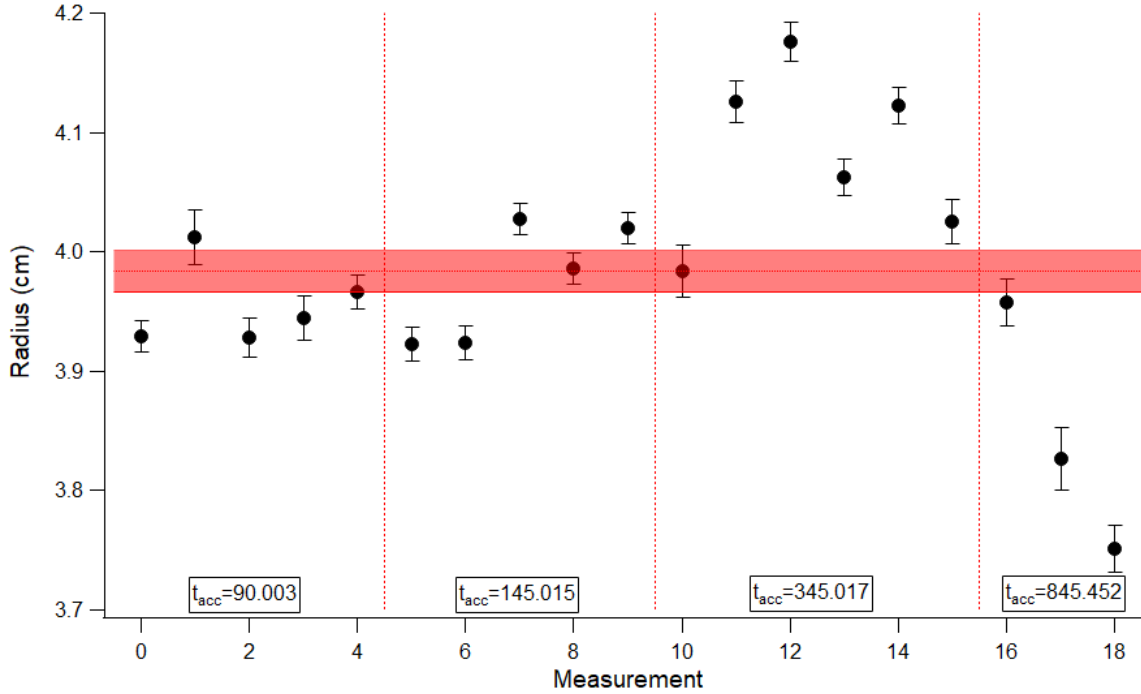


Figure 7.2: The measured radii for ^{112}Ag in October of 2016. The red band shows the average radius and its uncertainty.

However, the measured radii varied between the accumulation times. As these were the first on-line measurements taken with PI-ICR at the CPT, this problem had never been seen before and had not been anticipated. It was eventually determined that there was not enough data to accurately understand or correct for this systematic error, but it provided the hint that the systematic shift was due to a t_{acc} dependent position of the ions on the MCP, which would produce a systematic shift in the phase and therefore the frequency determination.

7.2 Testing Systematics—January 2017

7.2.1 Data Collection

Additional CARIBU beam time was acquired in January of 2017, with the explicit goal of understanding the systematic error seen in the October 2016 data and producing a method

to correct for the error. Over the course of two days, additional data were collected by then-graduate-student Rodney Orford for the isotopes ^{115}Sn , ^{115}In , and ^{115}Cd . ^{115}In decays into ^{115}Sn with a half-life of 4.4×10^{14} years. With a Q -value measured to a precision of 10 eV and individual masses measured to precisions of just over 10 eV/ c^2 for each, this was an ideal set of isotopes to use to test the systematic problems seen in the October 2016 data.

Data were collected for one isotope at a time, with a single reference measurement preceding a set of four to six final spot measurements. The accumulation times of these final spot measurements were varied over a range of about one millisecond, with differences of 100 to 200 microseconds between subsequent measurements. As with the data taken in October of 2016, the exact accumulation times were chosen so that all reference and final spots hit approximately the same position on the MCP detector, minimizing sources of systematic error.

Accumulation times were varied around 159 ms, 245 ms, 318 ms, and 348 ms for ^{115}Sn and around 159 ms and 318 ms for ^{115}In . These individual measurements were each used to calculate the cyclotron frequencies for ^{115}Sn and ^{115}In . The calculated frequencies were plotted against accumulation time to search for possible trends. Additionally, the radius between the final spot center and the center of the position sensitive detector was calculated for each measurement and plotted against accumulation time to search for possible trends and to compare against the fluctuations of the frequency measurements.

7.2.2 Data Analysis

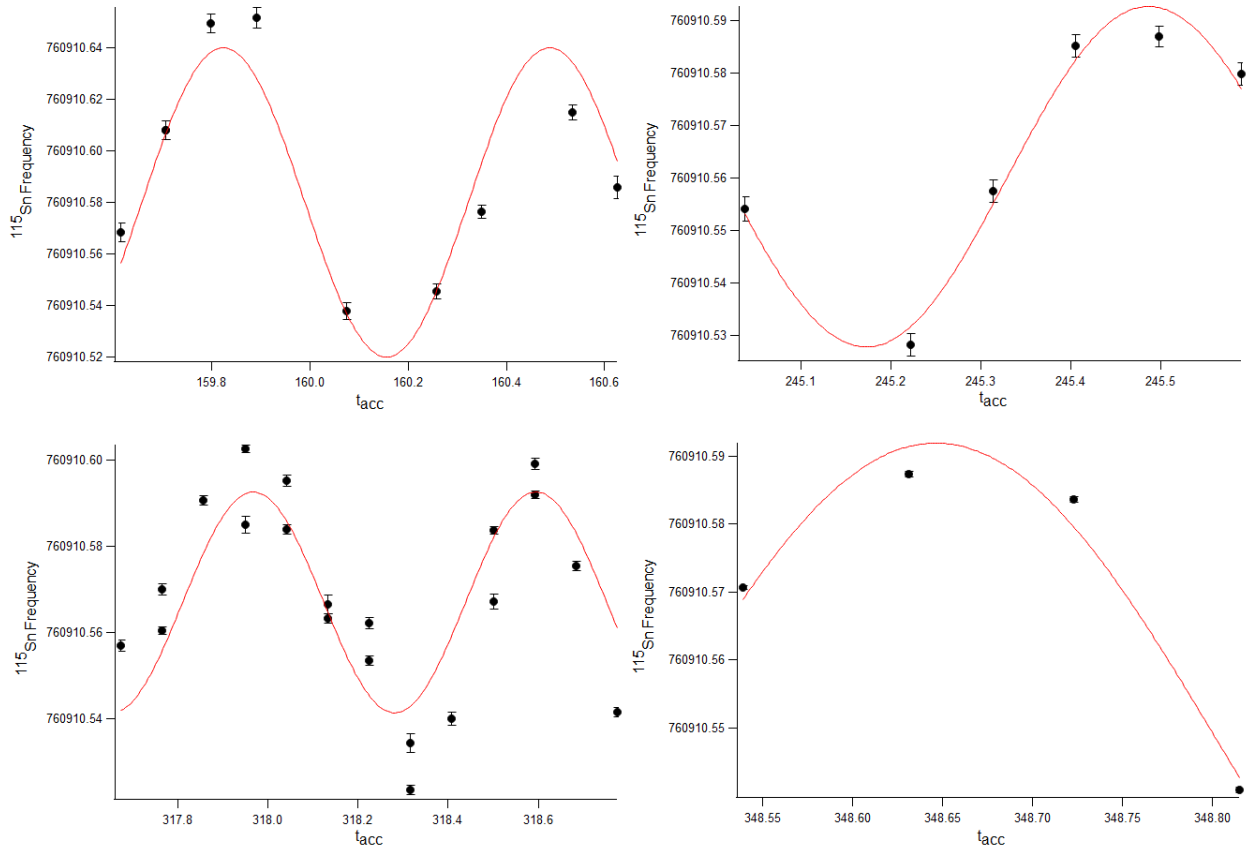


Figure 7.3: Measured frequencies, with sinusoidal fits, taken of ^{115}Sn in January of 2017. The accumulation time, t_{acc} , was varied by a hundred microseconds at a time over a range of one millisecond to understand the effect t_{acc} has on the measured frequency at CPT.

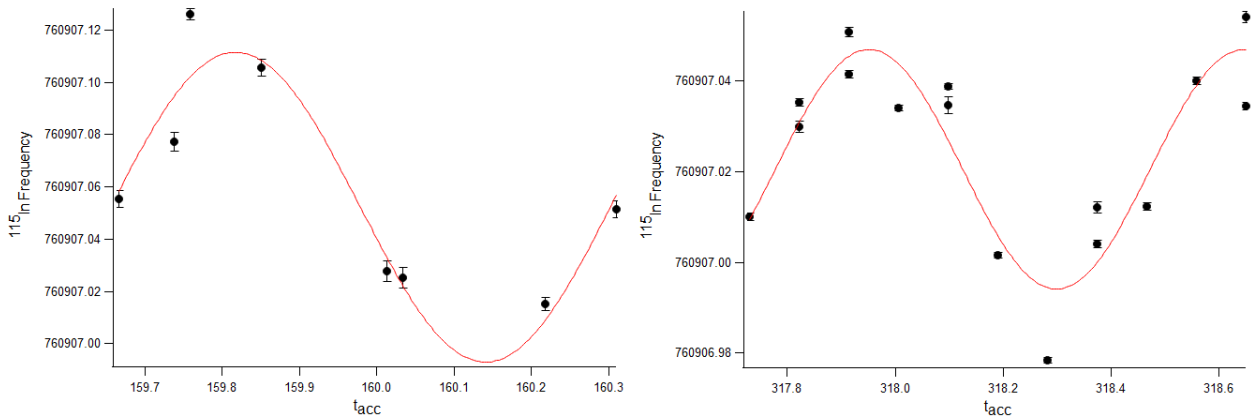


Figure 7.4: Measured frequencies, with sinusoidal fits, taken of ^{115}In in January of 2017. The accumulation time, t_{acc} , was varied by a hundred microseconds at a time over a range of one millisecond to understand the effect t_{acc} has on the measured frequency at CPT.

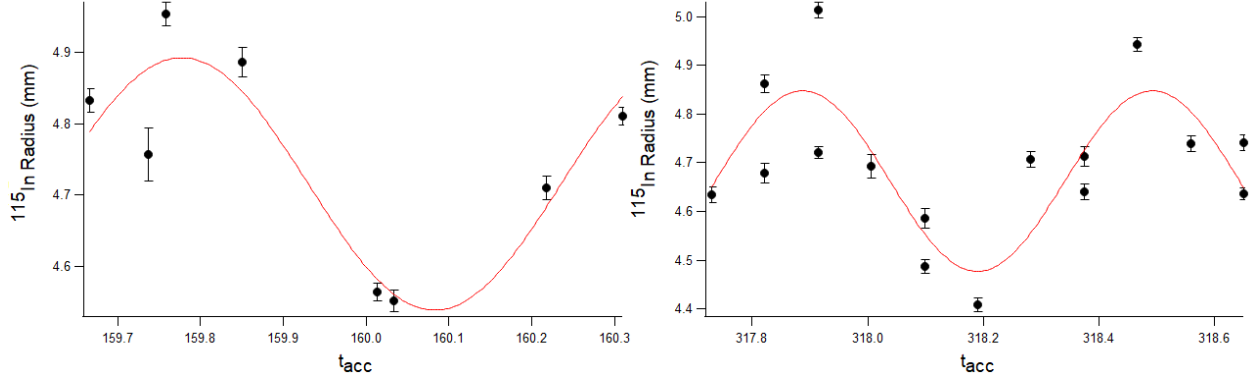


Figure 7.5: Measured radii, with sinusoidal fits, taken of ^{115}In in January of 2017. The accumulation time, t_{acc} , was varied by a hundred microseconds at a time over a range of one millisecond to understand the effect t_{acc} has on the measured frequency at CPT.

As can be seen in Figs. 7.3 and 7.4, the newly collected data showed a clear sinusoidal dependence of frequency on t_{acc} . A similar sinusoidal dependence was found in the radius of each measurement, as seen in Fig. 7.5. The sinusoidal change of the measured radius allowed for theories to be formed regarding the cause of the fluctuations. It was speculated that there was some residual magnetron motion when the ions are injected into the trap before the initial dipole RF pulse at ω_+ is applied. This residual magnetron frequency is then superimposed onto the reduced cyclotron motion, causing a small precession of radius r_m on top of the reduced cyclotron motion with r_+ . The phases of ρ_+ and ρ_- evolve separately. Therefore, the relative phase between the two motions when the ω_c quadrupolar RF pulse is applied depends on t_{acc} . After conversion, the final radius is $\rho_+ \pm r_m$ depending on the relative phase. The phase measured, ϕ , is therefore different based on where the spot is in its precession. In Fig. 7.6, a diagram describing the result of this superimposition can be seen. The expected, fully-converted motion is shown with the solid black line. The addition of the residual magnetron motion is shown with the dashed black line. The position of the reference spot is in the expected location. However, the position of the final spot can vary by up to r_m , causing a change in phase by up to $\delta\phi$.

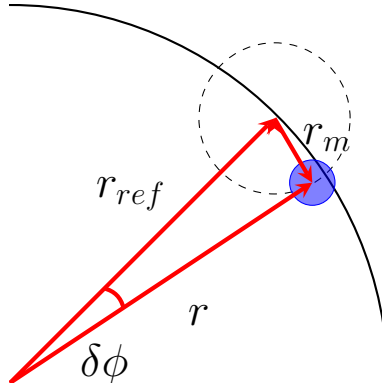


Figure 7.6: A diagram of the hypothesized cause of the sinusoidal fluctuations of the radius and frequency at the CPT. If not all of the magnetron motion of the ion is converted into cyclotron motion, the residual magnetron motion will cause the ion to precess around the greater orbit. Here, the expected motion is the solid black line, while the residual magnetron motion is the dotted black line. The spot on the detector is the filled blue circle.

By taking data points at a variety of different t_{acc} values, the measured frequencies can be plotted and fit with a sine wave. The frequency of the sine wave should be the magnetron frequency of the system. The baseline of this sine wave is the expected true cyclotron frequency of the ion being measured. Looking at Fig. 7.6, the sine wave crosses the baseline when the spot lands in line with the reference spot. The amplitude of the sine wave corresponds to the radius of the residual magnetron motion, with the peaks and troughs corresponding to $\phi + \delta\phi$ and $\phi - \delta\phi$ respectively.

Table 7.4 shows the parameters of the sine waves fit to the data shown in Figs. 7.3 and 7.4. The frequency, ω , corresponding to the magnetron frequency of the system, is in agreement for all fits. The baseline, y_0 , corresponding to the true cyclotron frequency of the ions, is also internally consistent for each set of data, with fit uncertainties on the order of only 10^{-9} . The desired precision of 1 keV for ^{112}Ag , $^{112,115}\text{Cd}$, and ^{115}In corresponds to 10^{-8} uncertainty, and so taking data in such a way to correct for this systematic effect will not prevent us from reaching the statistical precision goal.

Table 7.4: The baseline and frequencies of the sine waves fit to the data seen in Figs. 7.3 and 7.4. The baseline is expected to be the actual cyclotron frequency of the ions measured, while the frequency is the magnetron frequency of the system.

^{115}Sn			
t_{acc}	y_0	A	ω
160	760910.5799 (0.0066)	0.060 (0.009)	9.45 (0.35)
245	760910.5602 (0.0024)	0.032 (0.004)	10.00 (0.49)
318	760910.5669 (0.0029)	0.026 (0.004)	9.99 (0.50)
348	760910.5477 (0.0042)	0.044 (0.006)	10.00 (0.50)
^{115}In			
t_{acc}	y_0	A	ω
160	760907.0522 (0.0059)	0.059 (0.01)	9.72 (0.53)
318	760907.0206 (0.0025)	0.026 (0.003)	9.045 (0.48)

Table 7.5: The Q -values measured for the decay $^{115}\text{In} \rightarrow ^{115}\text{Sn}$, using the corrected data from Table 7.4 compared to the AME2016 [1]. The column ΔQ is calculated as CPT-AME.

t_{acc}	CPT Q -value	AME 2016	ΔQ
160	494.98 (0.93)	497.489 (0.010)	-2.51 (0.93)
318	498.15 (0.46)		0.67 (0.46)

It was therefore determined that taking data points over a range of t_{acc} values and fitting them with a sine wave would be a successful way to compensate for this source of systematic error. In order to employ this strategy, however, more data would need to be collected, at a variety of different t_{acc} values rather than several data points taken at the same t_{acc} . More beam time was requested using the CARIBU source and CPT, this time without the initially proposed $^{113}\text{Ag} \rightarrow ^{113}\text{Cd}$ and instead measuring ^{112}Ag , $^{112,115}\text{Cd}$, $^{112,115}\text{Sn}$, and ^{115}In .

7.2.3 Correcting the Data from the First Experiment

The corrections found from the January 2017 data were used to create a model, which could then be applied to the October 2016 experiment:

$$\Delta f_c = \frac{A}{t} \sin(\omega t + \phi), \quad (7.3)$$

where $A = 8.340 \text{ Hz}\cdot\text{s}$, $\omega = 9.5361(5) \text{ krad/s}$, and $\phi = -2.92(10) \text{ rad}$. This model was used to correct the systematic shift to f_c in each point, as can be seen in Fig. 7.7.

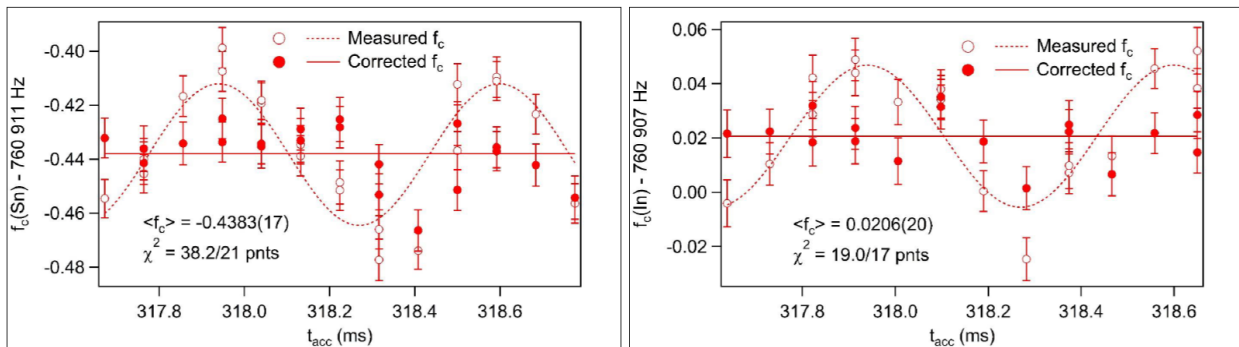


Figure 7.7: Frequency data for ^{115}Sn and ^{115}In , with Eq. 7.3 applied and used to correct the systematic shift in the frequency.

Table 7.6: The Q -values measured at the CPT facility in October of 2016, shown in Fig. 7.8, with the AME 2016 values for comparison.

Decay	CPT Q -value	AME 2016 Q -value	ΔQ
$^{112}\text{Ag} \rightarrow ^{112}\text{Cd}$	3996.5 (2.2)	3991.1 (2.4)	5.4
$^{113}\text{Ag} \rightarrow ^{113}\text{Cd}$	2083 (3)	2016.5 (16.6)	66.5
$^{115}\text{Cd} \rightarrow ^{115}\text{In}$	1451.78 (0.71)	1451.9 (0.7)	-0.12

With this newly corrected data, it was possible to extract Q -values for the decays measured, which can be found in Table 7.6 and Fig 7.8.

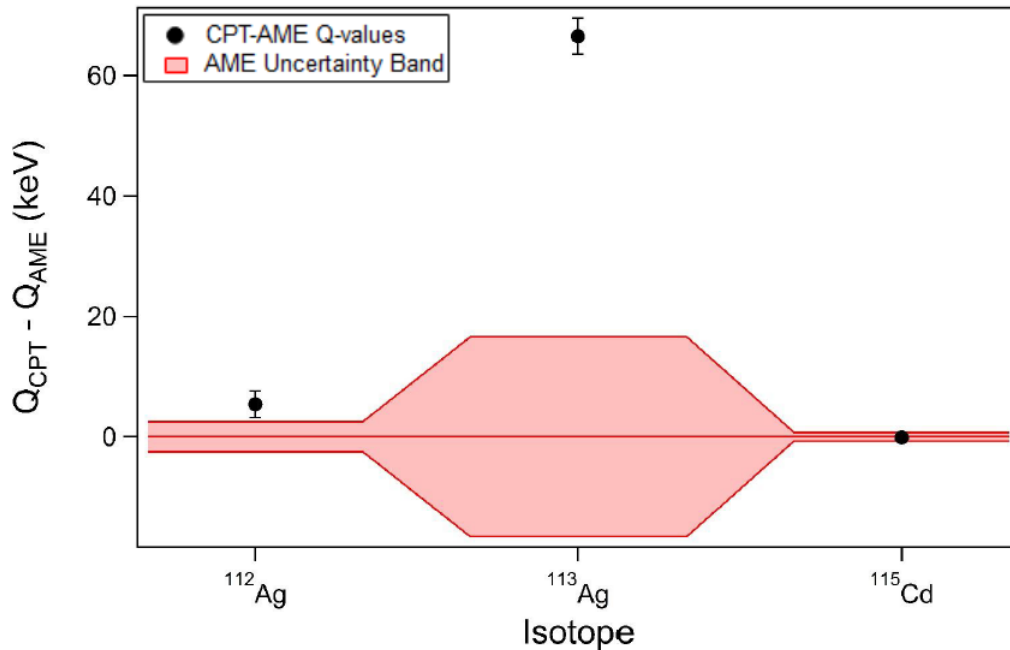


Figure 7.8: Q -values for the decays measured in October of 2016, found by applying Eq. 7.3 to correct the systematic shift in the model. The black points are the CPT measurements and the red bands show the uncertainty in the AME 2016.

7.3 Second Experiment—November 2018

7.3.1 Data Collection

The second beam time at the Canadian Penning Trap facility ran from November 19, 2018 to November 21, 2018. The 19th was used to measure ^{112}Ag , ^{112}Cd , and ^{112}Sn . The 20th and 21st were used to measure ^{115}Cd , ^{115}In , and ^{115}Sn . ^{112}Sn and ^{115}Sn were included for systematic checks using measurements of the Q -values of $^{112}\text{Sn} \rightarrow ^{112}\text{Cd}$ and $^{115}\text{In} \rightarrow ^{115}\text{Sn}$. Ratios were wanted of $^{112}\text{Cd}^+ / ^{112}\text{Ag}^+$, $^{112}\text{Sn}^+ / ^{112}\text{Cd}^+$, $^{115}\text{In}^+ / ^{115}\text{Cd}^+$, and $^{115}\text{Sn}^+ / ^{115}\text{In}^+$.

For the second beam time, measurements were alternated following the pattern: ion one, ion two, ion three, ion two, ion one. For the $A=112$ measurements, ions one, two, and three corresponded to $^{112}\text{Cd}^+$, $^{112}\text{Ag}^+$, and $^{112}\text{Sn}^+$, respectively. For the $A=115$ measurements, ions one, two, and three corresponded to $^{115}\text{In}^+$, $^{115}\text{Cd}^+$, and $^{115}\text{Sn}^+$, respectively. This allowed for ratios to be taken of m_2/m_1 and m_3/m_2 . Approximately twenty measurements of each ion were taken at once with t_{acc} varied by about 100 microseconds every measurement, with an overall range of approximately one millisecond, passing over the range twice. The accumulation times were chosen to put all reference and measurement spots at the same location on the position sensitive MCP detector, to prevent systematic errors from possible detector misalignment and dead spots. Between the end of 2016 and the end of 2018, the unstable power supply discussed earlier had been replaced. The electric field was therefore constant enough to no longer require a reference before every measurement. Instead, approximately every five measurements, a reference spot was taken, with $t_{acc} \approx 0$. For the $A = 112$ ions, t_{acc} was varied around 710 milliseconds. For the $A = 115$ ions, two complete sets of data were taken, one varied around 457 milliseconds and the other varied around 440

milliseconds.

7.3.2 Data Analysis

The frequencies measured for various isotopes were analyzed and the measured ratios were used to calculate the Q -values for each decay. For each isotope, the measured frequency values were plotted against the accumulation time, t_{acc} , and the points were fit with a sine wave. The baseline of the sine wave was then taken to be the true cyclotron frequency of the isotope. An example of a data set from the November 2018 beam time and its sine wave fit can be seen in Fig. 7.9. As with the 2016 beam time, Q -values were calculated for the decays of $^{112}\text{Ag} \rightarrow ^{112}\text{Cd}$ and $^{115}\text{Cd} \rightarrow ^{115}\text{In}$, as described in the proposal, as well as for the decays of $^{112}\text{Sn} \rightarrow ^{112}\text{Cd}$ and $^{115}\text{In} \rightarrow ^{115}\text{Sn}$ to use as systematic checks.

In Table 7.7, the Q -values measured by the CPT facility can be seen, compared to the AME 2016. The bolded values are the weighted averages of the points. This comparison is also shown in Fig. 7.10, where the points are the various Q -value measurements performed by the CPT facility and the red bands are the AME 2016 uncertainty bands.

7.4 Combining the Data and Concluding

The final Q -values for the decays of $^{112}\text{Ag} \rightarrow ^{112}\text{Cd}$, $^{113}\text{Ag} \rightarrow ^{113}\text{Cd}$, and $^{115}\text{Cd} \rightarrow ^{115}\text{In}$ can be seen in Table 7.8 and Fig. 7.11. For the decay of ^{112}Ag , the uncertainty was improved by a factor of 3 over the AME 2016. For the decay of ^{113}Ag , the uncertainty was improved by a

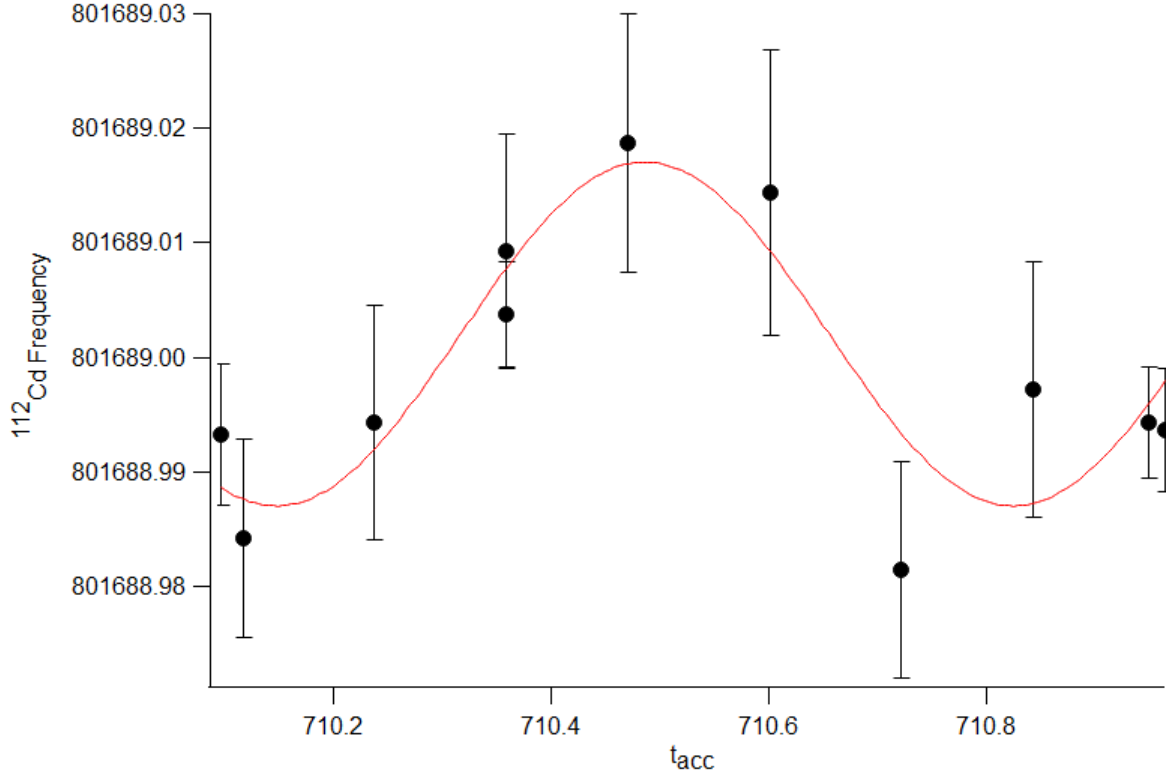


Figure 7.9: Measured frequencies, with a sinusoidal fit, taken of ^{112}Cd at the CPT facility in November of 2018. The accumulation time, t_{acc} , was varied by a hundred microseconds at a time over a range of one millisecond to allow for fitting and correction of the systematic error.

factor of 5.5 over the AME 2016. And for the decay of ^{115}Cd , the uncertainty was improved by a factor of 1.8 over the AME 2016. The Q -values of ^{112}Ag and ^{115}Cd agreed with the AME 2016 within one σ , while the Q -value of ^{113}Ag disagreed by more than four σ . ^{112}Ag was precisely measured at ISOLTRAP in 2010 [72] while ^{115}In was precisely measured at Florida State University in 2009 [52]. It is therefore understandable that the AME 2016 was accurate for these two, while the unmeasured ^{113}Ag showed a strong shift. In all three cases, an ultra-low Q -value decay is not energetically viable.

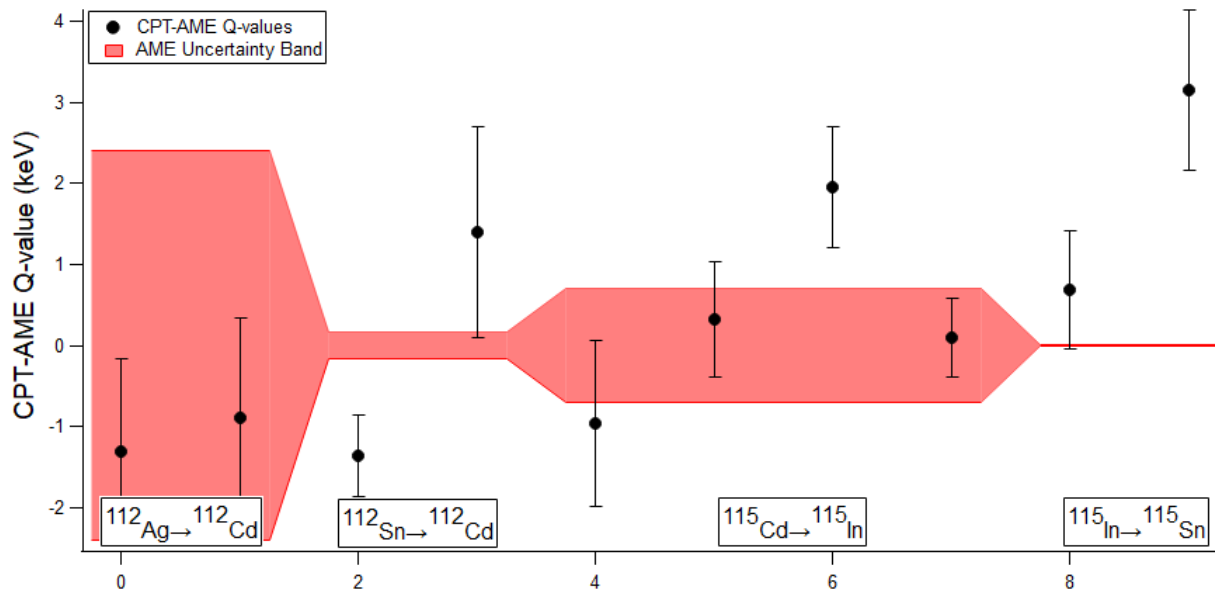


Figure 7.10: Data taken at the CPT facility in November of 2018. The points show the measured Q -values with the AME 2016 values subtracted out. The red bands show the uncertainty in the AME 2016.

Table 7.7: The Q -values measured at the CPT facility in November of 2018, shown in Fig. 7.10, with the AME 2016 values for comparison. The bolded values are weighted averages.

Decay	CPT Q -value	AME 2016 Q -value	ΔQ
$^{112}\text{Ag} \rightarrow ^{112}\text{Cd}$	3989.8 (1.1)	3991.1 (2.4)	-1.3
	3990.2 (1.2)		-0.9
	3989.98 (0.81)		-1.11
$^{112}\text{Sn} \rightarrow ^{112}\text{Cd}$	1918.5 (0.5)	1919.83 (0.30)	-1.4
	1921.3 (1.3)		1.4
	1918.86 (0.47)		-0.97
$^{115}\text{Cd} \rightarrow ^{115}\text{In}$	1450.9 (1.0)	1451.9 (0.7)	-1.0
	1452.2 (0.7)		0.3
	1453.9 (0.8)		2.0
	1452.0 (0.5)		0.1
	1452.27 (0.34)		0.36
$^{115}\text{In} \rightarrow ^{115}\text{Sn}$	498.18 (0.72)	497.489 (0.010)	0.691
	500.6 (1.0)		3.11
	499.01 (0.58)		1.52

Table 7.8: The Q -values measured at the CPT facility using combined data from the October 2016 experiment and the November 2018 experiment, shown in Fig. 7.11, with the AME 2016 values for comparison.

Decay	E^*	AME 2016		CPT	
		Q (keV)	Q_{UL} (keV)	Q (keV)	Q_{UL} (keV)
$^{112}\text{Ag} \rightarrow ^{112}\text{Cd}$	3997.75 (0.14)	3991.1 (2.4)	-6.7 (2.4)	3990.0 (0.8)	-7.8 (0.8)
$^{113}\text{Ag} \rightarrow ^{113}\text{Cd}$	2015.6 (2.5)	2016.5 (16.6)	0.9 (16.8)	2084.8 (3.0)	69.2 (3.9)
$^{115}\text{Cd} \rightarrow ^{115}\text{In}$	1451.9 (0.7)	1451.9 (0.7)	3.1 (0.7)	1452.3 (0.4)	3.5 (0.4)

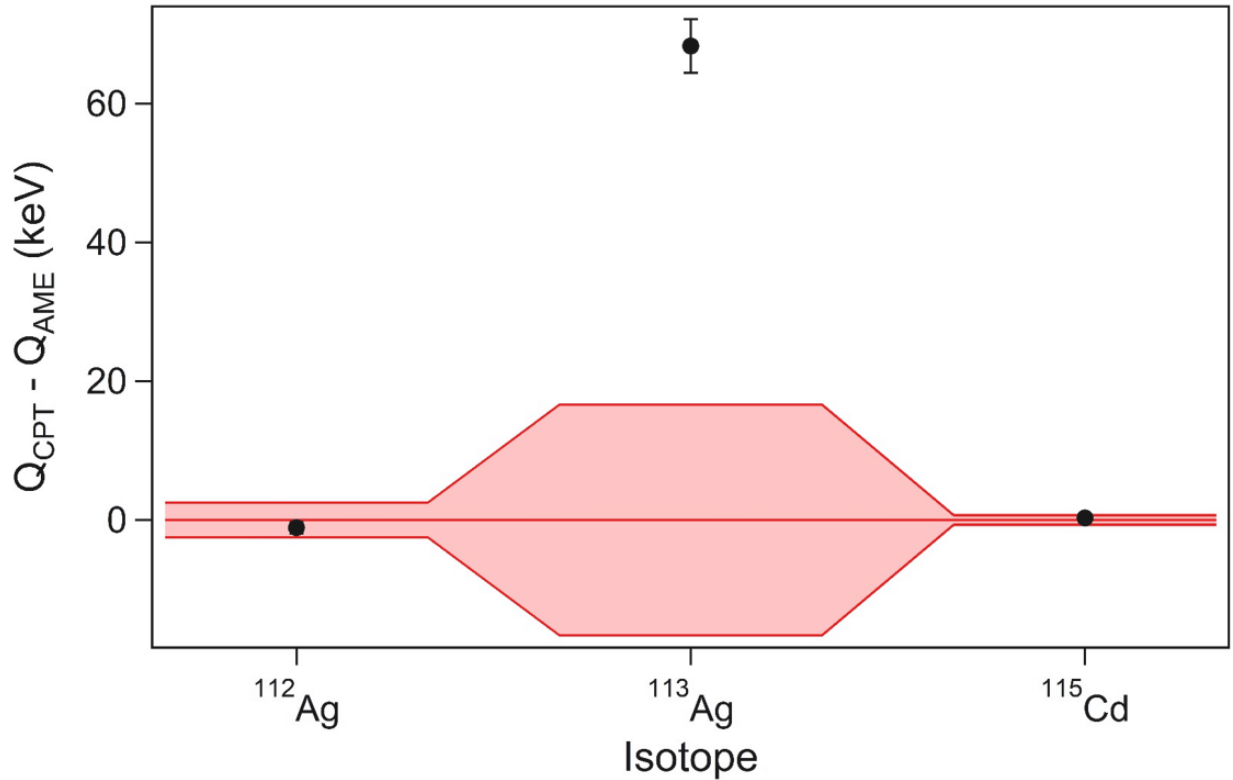


Figure 7.11: Q -values measured at CPT, using combined data from the October 2016 experiment and the November 2018 experiment. The points show the measured Q -values with the AME 2016 values subtracted out. The red bands show the uncertainty in the AME 2016.

Chapter 8

Measurement of ^{89}Y and ^{139}La Atomic Masses

This gets us impressively close to the exact answer. Uh, which slips my mind, but it's impressive.

-Scott Bogner

Measurements of ^{89}Y and ^{139}La atomic masses were performed at the LEBIT facility at the NSCL (see Chapter 3 for a full description of the facility). Both of these decays have potential ultra-low Q -value decay channels, as shown in Fig 8.1. For ^{89}Sr , the potential ultra-low Q -value decay channel is to the $3/2^-$ excited state at 1507.4(1) keV. For ^{139}Ba , there are two potential ultra-low Q -value decay channels, one to the $1/2^+$ state at 2310(19) keV and the other to the 2313(1) keV state of unknown spin and parity. These decay channels, along with the ultra-low Q -values they would produce, can be seen in Table 8.1.

Table 8.1: The list of potential ultra-low Q -value β -decay candidates studied using the LEBIT facility at the National Superconducting Cyclotron Laboratory, using information from the AME 2016 [1] and the NNDC [43]. The column E^* gives the excitation energy of the daughter nucleus. The column Q_{UL} is calculated as $Q_{GS} - E^*$.

Parent	Daughter	Decay	Q_{GS} (keV)	E^* (keV)	Q_{UL} (keV)
^{89}Sr	^{89}Y	β^-	1499.3 (1.6)	1507.4 (0.1)	-8.1 (1.6)
^{139}Ba	^{139}La	β^-	2312.5 (2.0)	2310 (19)	2.5 (19)
^{139}Ba	^{139}La	β^-	2312.5 (2.0)	2313 (1)	-0.5 (2)

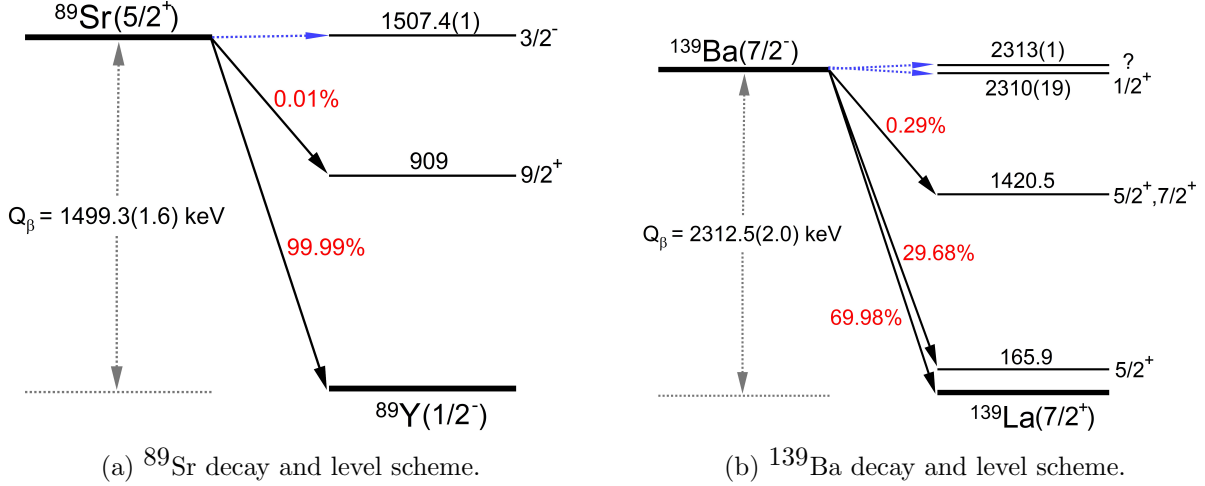


Figure 8.1: The decay and level schemes for ^{89}Sr , on the left, and ^{139}Ba , on the right. ^{89}Sr has one potential ultra-low Q -value decay channel while ^{139}Ba has two, all shown by the dotted blue arrows.

For both of the decays $^{89}\text{Sr} \rightarrow ^{89}\text{Y}$ and $^{139}\text{Ba} \rightarrow ^{139}\text{La}$, the masses of the unstable parents were already known to adequate precisions of $0.09 \text{ keV}/c^2$ and $0.3 \text{ keV}/c^2$, respectively [1]. ^{89}Sr is known through a precise $^{88}\text{Sr}(n,\gamma)^{89}\text{Sr}$ reaction, linking it to ^{88}Sr , which has been precisely measured with a Penning trap [73]. ^{139}Ba is known through a precise $^{138}\text{Ba}(n,\gamma)^{139}\text{Ba}$ reaction. The daughters were only known to precisions of $1.6 \text{ keV}/c^2$ and $2.0 \text{ keV}/c^2$ respectively and had never been directly measured. ^{89}Y was known primarily through a $^{88}\text{Sr}(p,\gamma)^{89}\text{Y}$ reaction measurement. ^{139}La was determined from a network of neutron capture, β -decay and α -decay measurements that link the lanthanides up to ^{163}Dy and ^{163}Ho . By lowering the uncertainty of the daughters to under $1 \text{ keV}/c^2$ with PTMS, it would be possible to say more definitively whether or not the potential ultra-low Q -value decay channels are energetically viable.

The results presented in this chapter were recently published in Physical Review C [74]. Portions of the text in this chapter and several of the figures presented here are reproduced from this reference. Additional details and discussion are included here, as well.

8.1 Measurements of ^{89}Y and ^{139}La Atomic Masses

For this experiment, isotopes of ^{89}Y and ^{139}La were created via the Laser Ablation Source (discussed in Section 3.1). The LAS was fitted with sheets of naturally abundant yttrium and lanthanum that were approximately $25\text{ mm} \times 25\text{ mm} \times 1\text{ mm}$ thick. Reference isotopes were created using the Test Ion Source (also discussed in Section 3.1). The TIS was used in surface ionization mode to produce $^{85}\text{Rb}^+$ and $^{87}\text{Rb}^+$ ions for use as reference ions in the measurement of ^{89}Y . It also was fitted with a canister of naturally abundant xenon gas to produce $^{136}\text{Xe}^+$ via plasma mode for use in measuring ^{139}La . All measurements were taken using the time of flight ion cyclotron resonance (TOF-ICR) technique, explained in detail in Section 3.4. An example resonance of $^{89}\text{Y}^+$ can be seen in Fig. 8.2.

For both measurements, the “indirect” method of measurement (described in Section 3.4.3) was used, as there was no rare isotope beam time to produce the parent isotopes. The LAS was initially fit with a target of lanthanum and the TIS fit with a canister of xenon gas. Each measurement of $^{139}\text{La}^+$ was bracketed by two reference measurements of $^{136}\text{Xe}^+$. The reference measurements were interpolated to find the cyclotron frequency of $^{136}\text{Xe}^+$ at the time of the measurements of $^{139}\text{La}^+$. The ions within the trap were driven with an RF pulse of 1 s and approximately seventy measurements of each isotope were taken, leading to seventy calculations of $R = f_{ion}/f_{ref}$. These were combined into a single average value of \bar{R} and were used via Eqn. 8.1 (given in Chapter 3 but restated here for convenience) to find the absolute mass of the isotopes of interest.

$$M_{int} = (M_{ref} - m_e) \frac{1}{\bar{R}} + m_e. \quad (8.1)$$

The overall process was repeated a second time, replacing the lanthanum target in the

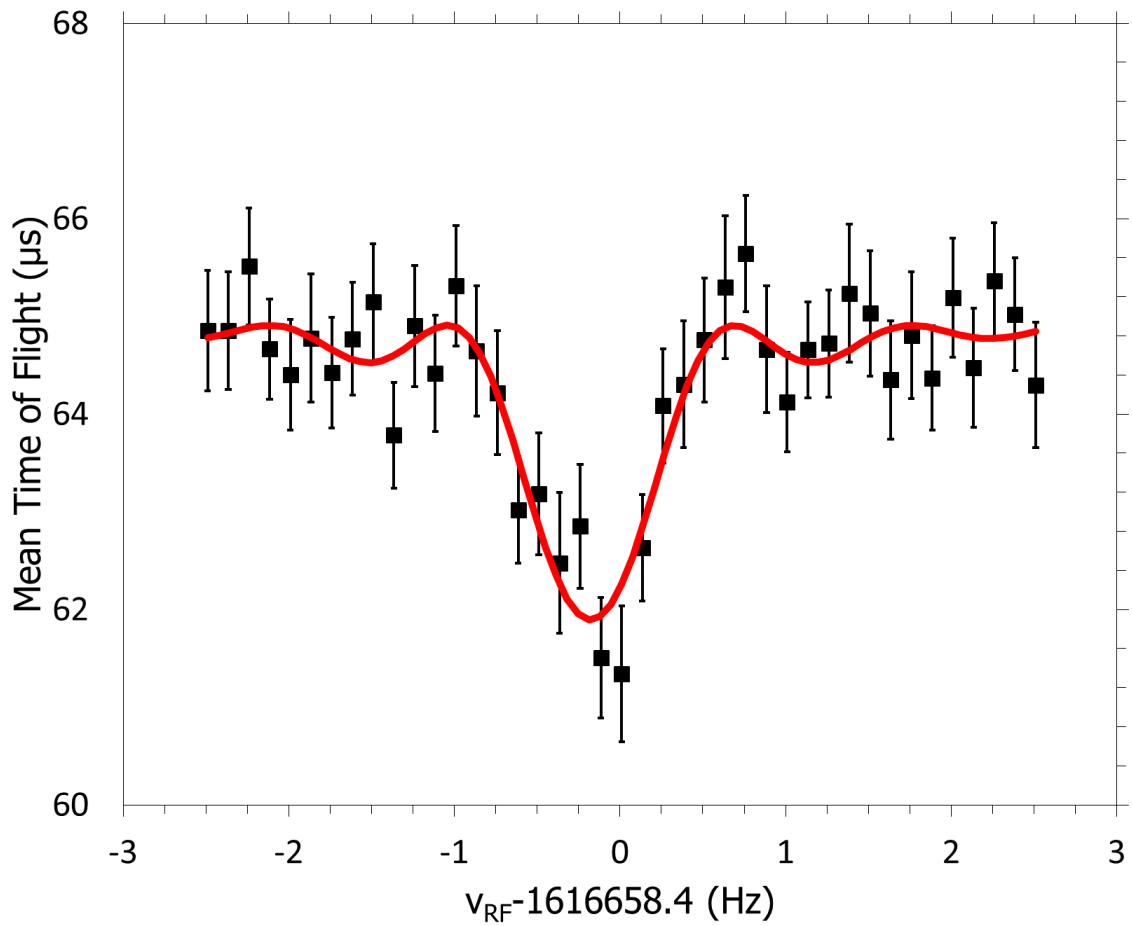


Figure 8.2: An example of a time of flight ion cyclotron resonance curve, shown here with ^{89}Y .

LAS with a target of yttrium and using the surface ionization technique to produce $^{85}\text{Rb}^+$ and $^{87}\text{Rb}^+$ in the TIS. A 500 ms excitation was used. Approximately fifty measurements of $^{89}\text{Y}^+$ were taken using $^{87}\text{Rb}^+$ as a reference, followed by an additional fifty measurements of $^{89}\text{Y}^+$ using $^{85}\text{Rb}^+$ as a reference. These were used to find two values of \bar{R} , which were then used to find the mass of ^{89}Y . The two values disagreed by about two sigma. To achieve more precise measurements and investigate the discrepancy, more data was taken using a 1 s excitation, with the pattern ^{85}Rb , ^{89}Y , ^{85}Rb , ^{87}Rb , ^{89}Y , ^{87}Rb , and used to find two separate values of \bar{R} and the mass of ^{89}Y . The data for the two different excitation times, as well as their weighted averages, can be seen in Fig. 8.3. As can be seen, the two sets of 1 s excitation data using ^{87}Rb and ^{85}Rb as references showed excellent agreement. The combined data for the two references (the pink bands in Fig. 8.3) disagreed by about 1.14 keV/c², or a little under 2 σ .

The absolute masses for ^{89}Y and ^{139}La , given as mass excesses, can be found in Table 8.2. These values are also plotted in Fig. 8.4 for clarity.

Table 8.2: Absolute mass measurements of ^{89}Y and ^{139}La , given as the mass excess. The column ΔME is the amount this measured mass excess deviates from the AME 2016.

Nuclide	Reference	ME (keV/c ²)		ΔME (keV/c ²)
		This Work	AME 2016	
^{89}Y	^{87}Rb	-87 710.67(0.49)		-2.3(1.7)
	^{85}Rb	-87 711.78(0.49)	-87 708.4(1.6)	-3.4(1.7)
	Ave.	-87 711.21(0.34)		-2.8(1.6)
^{139}La	^{136}Xe	-87 222.15(0.62)	-87 226.2(2.0)	4.0(2.1)

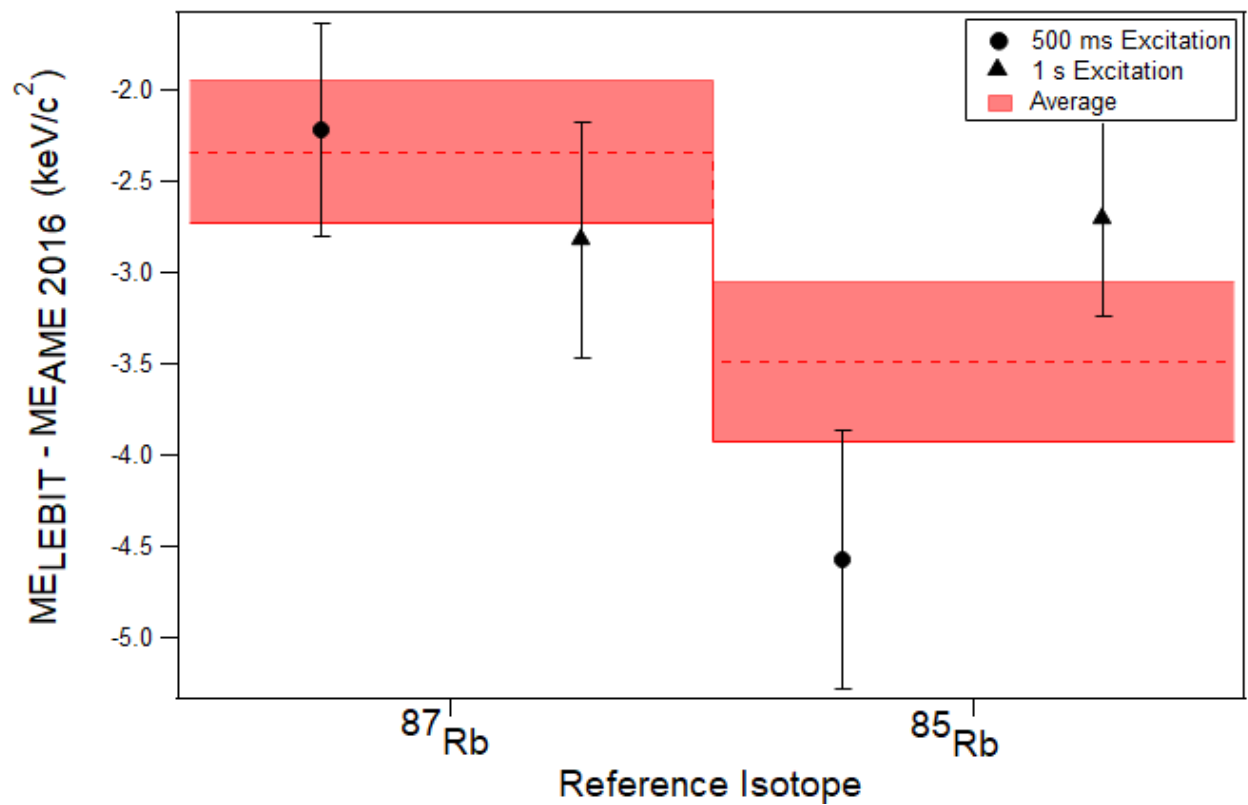


Figure 8.3: The mass excess (shown here as differences from the AME 2016) of ^{89}Y , calculated using two different references and two different excitation times. The red band is the weighted average for each reference.

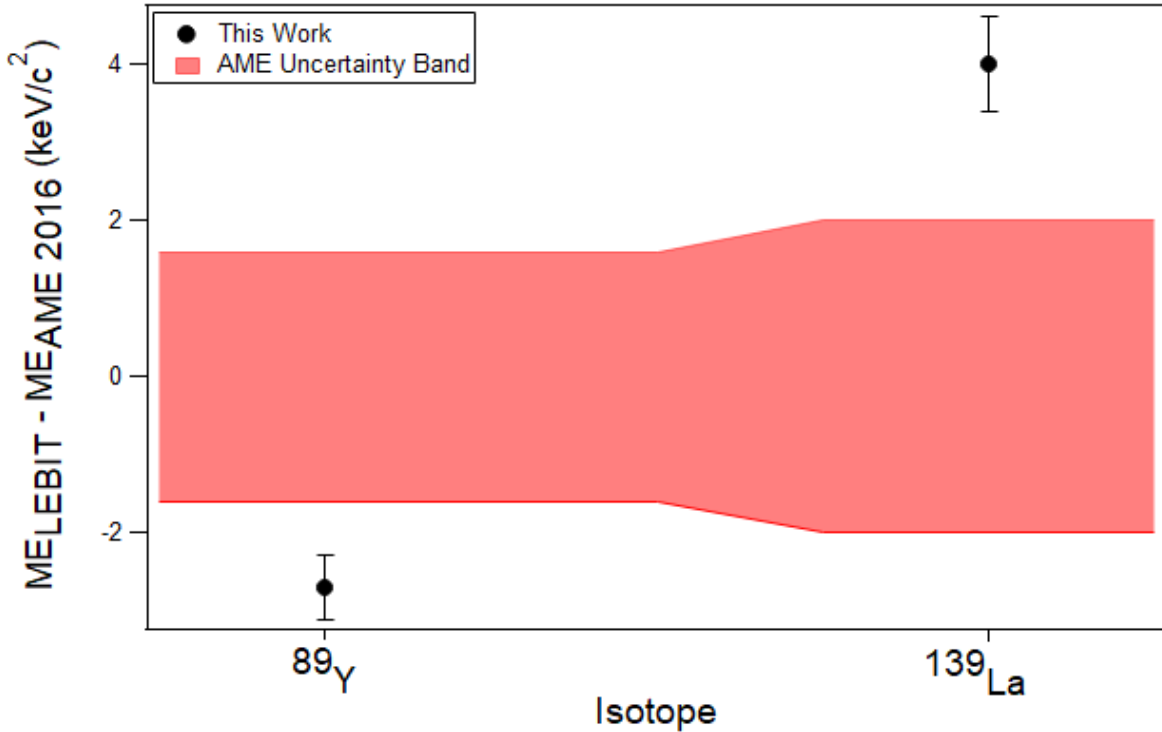


Figure 8.4: The weighted average Mass Excesses measured in this work compared to the AME 2016.

8.2 Analysis of ⁸⁹Sr and ¹³⁹Ba Decay

The absolute masses were then used with the absolute masses of the parent nuclides from the AME 2016 (see Table 8.3) to find the Q -values of the decays. For the case of ⁸⁹Y, the two mass measurements were used to find a weighted average, which was then used to find the Q -value. The two ground-state to ground-state Q -values can be found in Table 8.4. For both decays, the Q -values were measured to a precision better than 0.7 keV, surpassing the original goal of 1 keV.

Both isotopes deviated by about 1.5-2 σ in their mass excess from the AME 2016. As neither had previously been measured directly, this was not unexpected. With these updated mass excesses and Q -values, it is possible to be more definitive about their ultra-low Q -value candidacy. For the decay ⁸⁹Sr → ⁸⁹Y, the Q -value increased by about 2 keV. The new value

Table 8.3: Mass excesses for ^{89}Sr and ^{139}Ba , from the AME 2016.

Isotope	AME 2016 ME (keV/c ²)
^{89}Sr	-86209.02(0.09)
^{139}Ba	-84913.8(0.3)

Table 8.4: Q -values based on the absolute mass measurements in Table 4.3 and Eqn. 1.5. The column E^* gives the excitation energy of the daughter nucleus. The result for the ultra-low Q -value decay branch is calculated as $Q_{UL} = Q_{GS} - E^*$.

Parent	Daughter	Q_{GS} keV	E^* keV	Q_{UL} keV
^{89}Sr	^{89}Y	1502.19(0.41)	1507.4(0.1)	-5.21(32)
^{139}Ba	^{139}La	2308.37(0.68)	2310(19)	-1.6(19.0)
^{139}Ba	^{139}La	2308.37(0.68)	2313(1)	-4.6(1.2)

of 1502.19(0.41) keV is still less than the ^{89}Y $3/2^-$ excited state energy of 1507.4(0.1) keV. With the uncertainty of the Q -value decreased to under 1 keV, it can now be said definitively that the $3/2^-$ excited state is not an energetically viable candidate for ultra-low Q -value decay. For the decay $^{139}\text{Ba} \rightarrow ^{139}\text{La}$, the Q -value decreased by about 4 keV. The new value of 2308.37(0.68) is now substantially less than the excited state of unknown spin and parity at 2313(1) keV. With the uncertainty of the Q -value decreased to under 1 keV, it can now be said definitively that this unknown excited state is not an energetically viable candidate for ultra-low Q -value decay. The second excited state of ^{139}La , the $1/2^+$ state at 2310(19) keV has too large of an uncertainty for any definitive claims to be made. The value of this excited state will need to be measured to a higher precision to determine if it is still energetically viable for ultra-low Q -value decay.

Part III

Conclusion

Chapter 9

Summary and Outlook

I was hoping this could be a learning moment, but I'm not certain what you're supposed to learn.

-Ryan Ringle

The first Penning trap mass measurements of ^{138}La , ^{138}Ba , and ^{138}Ce were completed at LEBIT, along with direct Q -value measurements. The atomic mass uncertainties of ^{138}La and ^{138}Ce were reduced by nearly a factor of 6 and the mass of ^{138}Ba , previously determined from neutron capture measurements, was confirmed. The Q -value uncertainties of the decays $^{138}\text{La} \rightarrow ^{138}\text{Ce}$ and $^{138}\text{La} \rightarrow ^{138}\text{Ba}$ were reduced by an order of magnitude. The improved ^{138}La - ^{138}Ce β -decay Q -value measurement confirmed the end-point energy of the β spectrum measurements taken by Quarati, *et al.*, showing the LaBr_3 detectors used did not have any unaccounted systematic errors. The improved measurement also allowed for a closer look at the theoretical β spectrum calculation, improving the uncertainties of the experimental shape factor parameters by more than an order of magnitude. The ^{138}La - ^{138}Ba ϵ -decay Q -value measurement enabled the electron capture probability ratios for the K, L, and M shells to be recalculated and the uncertainties reduced by factors of 3. From here, it will be possible to use the improved theory to probe other highly-forbidden β -decay spectra, in turn improving understanding of the underlying nuclear structure.

From here, an additional forbidden β -decay Q -value measurement is that of ^{176}Lu . ^{176}Lu

decays via first-forbidden, non-unique β -decay to ^{176}Hf with a half-life of 3.8×10^{10} years. There is also the possibility of a potential fifth-forbidden, non-unique ϵ -decay to ^{176}Yb , with a Q -value of 109.1(1.2) keV. As with ^{138}La , found in scintillators of LaBr_3 , ^{176}Lu is found in scintillators of LYSO, or lutetium-yttrium oxyorthosilicate. This would allow for a clear, low-background β -decay spectrum of ^{176}Lu to be taken. A precise ground-state to ground-state Q -value measurement taken independently using a Penning trap would once again test the systematics of such scintillators and give additional experimental data to improve the theoretical fit.

The first on-line measurements taken with PI-ICR at the CPT facility were completed at ANL. These measurements found Q -values for $^{112}\text{Ag} \rightarrow ^{112}\text{Cd}$, $^{113}\text{Ag} \rightarrow ^{113}\text{Cd}$, and $^{115}\text{Cd} \rightarrow ^{115}\text{In}$ to test the energetic viability of potential ultra-low Q -value decays. The Q -value uncertainty for ^{112}Ag was improved by a factor of 3, the Q -value uncertainty for ^{113}Ag was improved by a factor of 5.5, and the Q -value uncertainty for ^{115}Cd was improved by a factor of 1.8. In the process, a systematic error at CPT caused by initial magnetron motion was discovered, modeled, and corrected. It was found that all three potential ultra-low Q -value decays, ^{112}Ag to the ^{112}Cd excited state at 3997.75 keV, ^{113}Ag to the ^{113}Cd excited state at 2016.5 keV, and ^{115}Cd to the ^{115}In excited state at 1451.9 keV, are not energetically viable.

The first Penning trap mass measurements of ^{89}Y and ^{139}La were also completed at LEBIT. The atomic mass uncertainties of ^{89}Y and ^{139}La were improved by factors of 3. With these measurements, the Q -value uncertainties of the decays $^{89}\text{Sr} \rightarrow ^{89}\text{Y}$ and $^{139}\text{Ba} \rightarrow ^{139}\text{La}$ were similarly improved by factors of 3. These new Q -value measurements allowed for definitive exclusion of two potential ultra-low Q -value decay candidates; neither the decay of ^{89}Sr to the ^{89}Y excited state at 1507.4 keV or the decay of ^{139}Ba to the ^{139}La excited state at 2313 keV are energetically viable. Improved measurements of the ^{139}La excited state at

2310 keV are necessary in order to determine if it is an ultra-low Q -value decay candidate.

From here, an additional offline measurement to evaluate potential ultra-low Q -value decay candidates could be made on ^{75}As . ^{75}As is the stable daughter for two potential ultra-low Q -value decays. ^{75}Se can decay via ϵ -decay to an excited state of ^{75}As and ^{75}Ge can decay via β -decay to an excited state of ^{75}As . As with the offline measurements of ^{89}Y and ^{139}La in this work, the unstable parents ^{75}Se and ^{75}Ge are known to adequate precisions of 0.07 and 0.09 keV/ c^2 , respectively. The stable daughter, ^{75}As , however, is only known to a precision of 0.88 keV/ c^2 . However, measuring arsenic would introduce additional safety concerns which must be taken into account.

Spinny
bit

Zappiness

Miracles

$$f_c = \frac{qB}{2\pi m}$$

Circlce

Heavy
boi

Bibliography

- [1] W. Huang, G. Audi, M. Wang, F. Kondev, S. Naimi, and X. Xu, *Chin. Phys. C* **41**, 3 (2017).
- [2] M. H. Holzscheiter, *Phys. Scr.* **69**, 69 (1995).
- [3] J. R. Pierce, *Theory and Design of Electron Beams* (D. Van Nostrand Co., Inc, 1949).
- [4] H. G. Dehmelt, in *Advances in Atomic and Molecular Physics*, Vol. 3, edited by D. R. Bates and I. Estermann (Elsevier, 1967) Chap. 2, “Radiofrequency Spectroscopy of Stored Ions I: Storage”.
- [5] “Nobel prize,” <https://www.nobelprize.org/prizes/physics/1989/summary/>, year=.
- [6] G. Bollen, H. Hartmann, H.-J. Kluge, M. König, T. Otto, G. Savard, and H. Stolzenberg, *Phys. Scr.* **46**, 581 (1992).
- [7] G. Bollen, R. B. Moore, G. Savard, and H. Stolzenberg, *Jour. Appl. Phys.* **68**, 9 (1990).
- [8] G. Bollen, S. Becker, H.-J. Kluge, M. König, R. B. Moore, T. Otto, H. Raimbault-Hartmass, G. Savard, and L. S. H. Stolzenberg, *Nuc. Instru. Meth. Phys. Res. A* **368**, 675 (1995).
- [9] H. Stolzenberg, S. Becker, G. Bollen, F. Kern, H.-J. Kluge, T. otto, G. Savard, L. Schweikhard, G. Audi, and R. B. Moore, *Phys. Rev. Lett* **65**, 3104 (1990).
- [10] P. Lofy, D. Morrissey, G. Bollen, D. Davies, R. Ringle, P. Schury, S. Schwarz, T. Sun, D. Vanwasshenova, L. Weissman, and D. Wiggins, (2002).
- [11] S. Schwarz, C. Bachelet, M. Block, G. Bollen, D. Davies, M. Facina, C. M. F. III, C. Guénaut, J. Huikari, E. Kwan, A. A. Kwiatkowski, D. J. Morrissey, G. Pang, A. Prinke, R. Ringle, J. Savory, P. Schury, C. Sumithrarachchi, and T. Sun, in *TCP 2006: Proceedings of the 4th International Conference on Trapped Charged Particles*, edited by J. Dilling, M. Comyn, J. Thomson, and G. Gwinner (Springer, 2007).
- [12] S. Eliseev, K. Blaum, M. Block, C. Droese, M. Goncharov, E. M. Ramirez, D. A. Nesterenko, Y. N. Novikov, and L. Schweikhard, *Phys. Rev. Lett.* **110**, 082501 (2013).
- [13] P. Tipler and R. Llewellyn, *Modern Physics*, 5th ed. (W. H. Freeman, 2008).

- [14] F. Joliot and I. Curie, *Nature* **133**, 201 (1934).
- [15] G. C. Wick, *Rendiconti dell'Accademia dei Lincei* **19**, 319 (1934).
- [16] R. Dunlap, *Particle Physics* (Morgan and Claypool Publishers, 2018).
- [17] H. F. Schopper, *Weak Interactions and Nuclear Beta Decay* (North-Holland Publishing Company, 1966).
- [18] K. Zuber, *Neutrino Physics* (Institute of Physics Publishing, 2004).
- [19] J. Kostensalo, M. Haaranen, and J. Suhonen, *Phys. Rev. C* **95**, 044313 (2017).
- [20] M. Haaranen, P. C. Srivastava, and J. Suhonen, *Phys. Rev. C* **93**, 034308 (2016).
- [21] F. G. A. Quarati, I. V. Khodyuk, C. W. E. van Eijk, P. Quarati, and P. Dorenbos, *Nat. Instru. Meth. Phys. Res. A* **683**, 46 (2012).
- [22] F. G. A. Quarati, P. Dorenbos, and X. Mougeot, *App. Rad. Iso.* **109**, 172 (2016).
- [23] R. H. Good, *Phys. Rev.* **94**, 931 (1954).
- [24] X. Mougeot and C. Bisch, *Phys. Rev. A* **90**, 012501 (2014).
- [25] K. Gulyuz, J. Ariche, G. Bollen, S. Bustabad, M. Eibach, C. Izzo, S. J. Novario, M. Redshaw, R. Ringle, R. Sandler, S. Schwarz, and A. A. Valverde, *Phys. Rev. C* **91**, 055501 (2015).
- [26] M. Eibach, G. Bollen, K. Gulyuz, C. Izzo, M. Redshaw, R. Ringle, R. Sandler, and A. A. Valverde, *Phys. Rev. C* **94**, 015502 (2016).
- [27] N. D. Gamage, G. Bollen, M. Eibach, K. Gulyuz, C. Izzo, R. M. E. B. Kandegedara, M. Redshaw, R. Ringle, R. Sandler, and A. A. Valverde, *Phys. Rev. C* **94**, 025505 (2016).
- [28] R. M. E. B. Kandegedara, G. Bollen, M. Eibach, N. D. Gamage, K. Gulyuz, C. Izzo, M. Redshaw, R. Ringle, R. Sandler, and A. A. Valverde, *Phys. Rev. C* **96**, 044321 (2017).
- [29] C. Izzo, G. Bollen, S. Bustabad, M. Eibach, K. Gulyuz, D. J. Morrissey, M. Redshaw, R. Ringle, R. Sandler, S. Schwarz, and A. A. Valverde, *Nuc. Instru. Meth. Phys. Res. B* **376**, 60 (2016).
- [30] C. Smorra, *Setup of a carbon-cluster laser ion source for high-precision mass spectrometry*, Ph.D. thesis, Johannes Gutenberg-Universität Mainz (2008).
- [31] A. M. Klose, *Production of singly-charged, transition-metal beams and subsequent collinear laser spectroscopy of neutral, stable Mn-55 and Fe-56*, Ph.D. thesis, Michigan State University (2013).

- [32] S. Schwarz, G. Bollen, D. Lawton, A. Neudert, R. Ringle, P. Schury, and T. Sun, *Nuc. Instru. Meth. Phys. Res. B* **204**, 474 (2003).
- [33] R. Ringle, *High-Precision Mass Measurement of ^{38}Ca and Development of the LEBIT 9.4-T Penning Trap System*, Ph.D. thesis, Michigan State University (2006).
- [34] R. Ringle, G. Bollen, A. Prinke, J. Savoy, P. Schury, S. Schwarz, and T. Sun, *Int. Jour. of Mass Spec.* **263**, 1 (2007).
- [35] S. Becker, G. Bollen, F. Kern, H.-J. Kluge, R. B. Moore, G. Savard, L. Schweikhard, H. Stolzenberg, and I. Collaboration, *Int. Jour. of Mass Spec.* **99**, 1 (1990).
- [36] M. Kretzschmar, *Eur. J. Phys.* **12**, 240 (1991).
- [37] L. S. Brown and G. Gabrielse, *Phys. Rev. A* **25**, 2423 (1982).
- [38] G. Gräff, H. Kalinowsky, and J. Traut, *Z. Phys. A Atom Nucl.* **297**, 35 (1980).
- [39] N. R. Daly, *Rev. Sci. Instru.* **31**, 264 (1960).
- [40] M. König, G. Bollen, H.-J. Kluge, T. Otto, and J. Szerypo, *Int. J. Mass. Spectrom. Ion Process* **142**, 95 (1995).
- [41] R. Ringle, T. Sun, G. Bollen, D. Davies, M. Facina, J. Huikari, E. Kwan, D. J. Morrissey, A. Prinke, J. Savory, P. Schury, S. Schwarz, and C. S. Sumithrarachchi, *Phys. Rev. C* **75**, 055503 (2007).
- [42] R. T. Birge, *Phys. Rev.* **40**, 207 (1932).
- [43] “Nuclear database 2,” <https://www.nndc.bnl.gov/nudat2/>, year=,.
- [44] R. Sandler, G. Bollen, J. Dissanayake, M. Eibach, K. Gulyuz, A. Hamaker, C. Izzo, X. Mougeot, D. Puentes, F. G. A. Qarati, M. Redshaw, R. Ringle, and I. Yandow, *Phys. Rev. C* **100**, 014308 (2019).
- [45] S. Eliseev, K. Blaum, M. Block, S. Chenmarev, H. Dorrer, C. E. Düllmann, C. Enss, P. E. Filianin, L. Gastaldo, M. Goncharov, U. Köster, F. Lautenschläger, Y. N. Novikov, A. Rischka, R. X. Schüssler, L. Schweikhard, and A. Türler, *Phys. Rev. Lett.* **115**, 062501 (2015).
- [46] M. Redshaw, E. Wingfield, J. McDaniel, and E. G. Myers, *Phys. Rev. Lett.* **98**, 053003 (2007).
- [47] M. Mougeot, *Appl. Radiat. Isot.* **134**, 225 (2018).
- [48] M. T. Mustonen and J. Suhonen, *J. Phys. G: Nucl. Part. Phys.* **37**, 064008 (2010).
- [49] C. M. Cattadori, M. D. Deo, M. Laubenstein, L. Pandola, and V. I. Tretyak, *Nucl. Phys. A* **748**, 333 (2005).
- [50] J. Kopp and A. Merle, *Phys. Rev. C* **81**, 045501 (2010).

- [51] J. S. E. Wieslander, J. Suhonen, T. Eronen, M. Hult, V.-V. Elomaa, A. Jokinen, G. Marissens, M. Misiaszek, M. T. Mustonen, S. Rahaman, C. Weber, and J. Äystö, *Phys. Rev. Lett.* **103**, 122501 (2009).
- [52] B. Mount, M. Redshaw, and E. G. Myers, *Phys. Rev. Lett.* **103**, 122502 (2009).
- [53] J. Bahcall, *Phys. Rev.* **129**, 6 (1962).
- [54] A. Saenz and P. Froelich, *Phys. Rev. C* **51**, 4 (1997).
- [55] M. T. Mustonen and J. Suhonen, *AIP Conf. Proc.* **1304**, 401 (2010).
- [56] N. D. Gamage, R. Bhandari, M. H. Gamage, R. Sandler, and M. Redshaw, *Hyp. Int.* **240**, 43 (2019).
- [57] M. Haaranen and J. Suhonen, *Eur. Phys. J. A* **49**, 93 (2013).
- [58] G. Savard, S. Baker, C. Davids, A. F. Levand, E. F. Moore, R. C. Pardo, R. Vondrasek, B. J. Zabransky, and G. Zinkmann, *Nuc. Instru. Meth. Phys. Res. B* **266**, 4086 (2008).
- [59] W. E. Nervi, *Phys. Rev.* **119**, 1685 (1960).
- [60] R. Orford, *Precision mass measurements of neutron-rich isotopes approaching the r-process path with the Canadian Penning Trap mass spectrometer*, Master's thesis, McGill University (2014).
- [61] J. C. D. Milton and J. S. Fraser, *Phys. Rev.* **111**, 3 (1958).
- [62] G. Savard, J. Clark, C. Boudreau, F. Buchinger, J. E. Crawford, H. Geissel, J. P. Greene, S. Gulick, A. Heinz, J. K. P. Lee, A. Levand, M. Maier, G. Münzenberg, C. Scheidenberger, D. Seweryniak, K. Sharma, G. Sprouse, J. Vaz, J. C. Wang, B. J. Zabransky, Z. Zhou, and the S258 Collaboration, *Nuc. Instru. Meth. Phys. Res. B* **204**, 582 (2003).
- [63] C. N. Davids and D. Peterson, *Nuc. Instru. Meth. Phys. Res. B* **266**, 4449 (2008).
- [64] T. Hirsh, N. Paul, M. Burkey, A. Aprahamian, F. Buchinger, S. Caldwell, J. Clark, A. Levand, L. Ying, S. Marley, G. Morgan, A. Nystrom, R. Orford, A. Galvan, J. Rohrer, G. Savard, K. Sharma, and K. Siegl, *Nuc. Instru. Meth. Phys. Res. B* **376**, 229 (2016).
- [65] H. Wollnik and M. Przewloka, *Int. Jour. of Mass Spec.* **96**, 3 (1990).
- [66] G. E. B. Morgan, *A Detector Upgrade for Phase-Imaging Ion Cyclotron Resonance Measurements at the CPT*, Master's thesis, University of Manitoba (2016).
- [67] B. Mount, M. Redshaw, and E. G. Myers, *Phys. Rev. A* **82**, 042513 (2009).
- [68] A. Lépine-Szily, *Hyp. Int.* **132**, 35 (2001).

- [69] G. Savard, R. C. Barber, C. Boudreau, F. Buchinger, J. Caggiano, J. Clark, J. E. Crawford, H. Fukutani, S. Gulick, J. C. Hardy, A. Heinz, J. K. P. Less, R. B. Moore, K. S. Sharma, J. Schwartz, D. Seweryniak, G. D. Sprouse, and J. Vaz, [Hyp. Int. **132**, 223 \(2001\)](#).
- [70] J. Clark, R. C. Barber, C. Boudreau, F. Buchinger, J. E. Crawford, S. Gulick, J. C. Hardy, A. Heinz, J. K. P. Lee, R. B. Moore, G. Savard, D. Seweryniak, K. S. Sharma, G. Sprouse, J. Vaz, J. C. Wang, and Z. Zhou, [Nuc. Instru. Meth. Phys. Res. B **204**, 487 \(2003\)](#).
- [71] R. Orford, J. A. Clark, A. Nystrom, G. Savard, A. Aprahamian, M. Brodeur, F. Buchinger, D. Burdette, M. Burkey, T. Y. Hirsh, J. Kelly, D. Lascar, L. Ling-Ying, G. E. Morgan, K. S. Sharma, and K. Siegl, in *Proceedings of the 14th International Symposium on Nuclei in the Cosmos*, edited by S. Kubono, T. Kajino, S. Nishimura, T. Isobe, S. Nagataki, T. Shima, and Y. Takeda (The Physical Society of Japan, 2017).
- [72] M. Breitenfeldt, C. Borgmann, G. Audi, S. Baruah, D. Deck, K. Blaum, C. Böhm, R. B. Cakirli, R. F. Casten, P. Delahaye, M. Dworschak, S. George, F. Herfurth, A. Herlert, A. Kellerbauer, M. Kowalska, D. Lunney, E. Minaya-Ramirez, S. Naimi, D. Neidherr, M. Rosenbusch, R. Savreux, S. Schwarz, L. Schweikhard, and C. Yazidjian, [Phys. Rev. C **81**, 034313 \(2010\)](#).
- [73] R. Rana, M. Höcker, and E. G. Myers, [Phys. Rev. A **86**, 050502 \(2012\)](#).
- [74] R. Sandler, G. Bollen, N. D. Gamage, A. Hamaker, C. Izzo, D. Puentes, M. Redshaw, R. Ringle, and I. Yandow, [Phys. Rev. C **100**, 024309 \(2019\)](#).